Advanced nano- and microdomain engineering of Rb-doped KTiOPO$_4$ for nonlinear optical applications

Charlotte Liljestrand

Doctoral Thesis in Physics

Laser Physics
Department of Applied Physics
School of Engineering Science
KTH

Stockholm, Sweden 2017

Advanced nano- and microdomain engineering of Rb-doped KTiOPO$_4$ for nonlinear optical applications

Akademisk avhandling som med tillstånd av Kungliga Tekniska Högskolan framlägges till offentlig granskning för avläggande av teknologie doktorsexamen i fysik, torsdagen 15 juni 2017 kl. 9.15 i sal FA32, Albanova, Roslagstullsbacken 21, KTH, Stockholm. Avhandlingen kommer att försvaras på engelska.

Cover picture: Optical micrograph of an ion-exchange grating with $\Lambda = 3$ µm in RKTP, as seen through the *y*-surface. The wavelengths in the microscope illumination become separated in space due to the refractive index distribution induced by the ion-exchange process.

Grant me the Serenity to accept
what I cannot change,

the Courage to change what I can,

and the Wisdom to know the difference

Charlotte Liljestrand
Advanced nano- and microdomain engineering in Rb-doped KTiOPO$_4$ for nonlinear optical applications
Department of Applied Physics, KTH – Royal Institute of Technology
106 91 Stockholm, Sweden

Abstract

Fine-pitch ferroelectric domain gratings are extensively used for generation of light in the visible and near-infrared spectral regions through quasi-phase matched (QPM) frequency conversion. Sub-μm QPM devices enables demonstration of nonlinear optics with counterpropagating waves, a field of nonlinear optics which remains sparsely explored due to the difficulty of fabricating high quality gratings.

In recent years, bulk Rb-doped KTiOPO$_4$ (RKTP) has emerged as a highly promising nonlinear materials for fabrication of fine-pitch QPM devices through periodic electric-field poling. RKTP possesses large optical nonlinearity and high resistance to optical damage, while demonstrating improved material homogeneity and lower ionic conductivity than its isomorphs which are important features for poling. Although fine-pitch QPM gratings, as well as large aperture QPM devices, have been demonstrated, fabrication of sub-μm high quality QPM devices remains a challenge.

The primary aim of this research was to develop a reliable method to fabricate high-quality sub-μm periodically poled RKTP crystals (PPRKTP) and exploit them in novel optical applications. For this purpose, a novel poling method was developed. It was based on periodic modulation of the coercive field through ion exchange, where K$^+$ ions are exchanged with Rb$^+$ in the crystal, to modulate the coercive field and the ionic conductivity. This enables periodic poling of higher quality and with shorter period than ever before.

High quality PPRKTP with a period of 755 nm were fabricated and used to demonstrate the first cascaded mirrorless optical parametric oscillator (MOPO), as well as the first MOPO pumped by a Q-switched laser. PPRKTP samples for blue light generation were fabricated, and second harmonic generation (SHG) was investigated with a high power 946 nm fiber laser. Up to 2 W of blue power was demonstrated for bulk samples, where the output power was limited by absorption of the SHG, leading to thermal dephasing of the devices. Laser-written waveguides were fabricated in PPRKTP for the first time, and a record high, SHG power of 76 mW was obtained.

Finally, the high-temperature stability of ferroelectric domain gratings was investigated. This is of utmost importance when a PPRKTP crystal is used as a seed for crystal growth. It was found that for charged domains walls, the domain-wall motion was highly anisotropic with rapid movement in *y*-direction while only small movements were observed in the *x*-direction of the crystal.

Sammanfattning

Ickelinjära ferroelektriska kristaller med artificiella domängitter med perioder av några mikrometer används idag för generering av ljus i de synliga och nära-infraröda våglängdsområdena, genom kvasifasmatchad (QPM) frekvenskonvertering. Med sub-µm QPM domängitter kan man åstadkomma ickelinjära optiska effekter med motpropagerande parametriska ljusvågor. Detta är ett område av den ickelinjära optiken som fortfarande är tämligen outforskat på grund av svårigheten med att tillverka högkvalitativa domängitter.

Under de senaste åren har Rb-dopat KTiOPO$_4$ (RKTP) blivit ett mycket lovande ickelinjärt material för tillverkning av QPM-gitter med mycket korta perioder genom periodisk elektrisk fält polning. RKTP kristallen har en hög optisk ickelinejäritet och den tål höga optiska intensiteter, samtidigt som materialet har bättre materialhomogenitet och lägre jonledningsförmåga än vad dess isomorfa kristaller har. De två senare egenskaperna har visat sig viktiga för att få en lyckad polning. Fastän QPM-gitter med kort periodicitet, liksom QPM-gitter med stor apertur, har demonstrerats, är tillverkningen av högkvalitativa QPM-kristaller med sub-µm perioder fortfarande en utmaning.

Det primära syftet med denna avhandling var att utveckla en pålitlig metod för att tillverka högkvalitativa sub-µm periodiskt polade RKTP kristaller (PPRKTP) och utnyttja dem i nya optiska tillämpningar. I detta syfte utvecklades en ny polningsmetod. Den baseras på periodiskt jonutbyte, där K$^+$ joner byts mot Rb$^+$ i kristallen, vilket resulterar i en samtidig modulation av materialets koerciva fält och jonledningsförmåga. Detta möjliggör i sin tur periodisk polning av högre kvalitet och med kortare perioder än någonsin tidigare har uppnåtts.

Högkvalitativa PPRKTP kristaller med en period på 755 nm tillverkades och användes för att demonstrera den första kaskaderade spegelfria optiska parametriska oscillatorn (MOPO), liksom den första MOPO processen pumpad av en Q-switchad laser. Vidare utvecklades PPRKTP-kristaller för generering av blått ljus via frekvensdubbling. Dessa utvärderades med hjälp av en högeffekts-fiberlaser vid 946 nm. Upp till 2 W av blått ljus erhölls för bulkkristallerna. Uteffekten begränsades av absorption av det blåa frekvensdubblade ljuset, vilket ledde till urfasning i QPM-gittret p.g.a. termiska effekter. Laserskrivna vågledare tillverkades sedan i PPRKTP för första gången, och en rekordhög effekt på 76 mW erhölls via frekvensdubbling.

Slutligen undersöktes stabiliteten hos de periodiskt polade domängitterna vid höga temperaturer. Det är viktigt att domängittrena är stabila när PPRKTP kristallerna används som ympämne för kristalltillväxt. Det visade sig att instabila domänväggar flyttade sig mycket anisotropt, med en snabb rörelse i kristallens *y*-riktning och en långsam rörelse i kristallens *x*-riktning.

List of Publications

This thesis is based on the following journal articles:

I.   **Charlotte Liljestrand**, Fredrik Laurell, and Carlota Canalias, "Periodic poling of Rb-doped $KTiOPO_4$ by coercive field engineering" Opt. Express 24, 14682-14689 (2016)

II.   Andrius Zukauskas, Anne-Lise Viotti, **Charlotte Liljestrand**, Valdas Pasiskevicius, and Carlota Canalias, "Cascaded counterpropagating nonlinear interactions in highly efficient sub-µm periodically poled crystals", submitted to Scientific Reports, March 2017

III.   **Charlotte Liljestrand**, Andrius Zukauskas, Valdas Pasiskevicius, and Carlota Canalias, "Highly efficient mirrorless optical parametric oscillator pumped by nanosecond pulses", Submitted to Optics Letters, April 2017

IV.   Gustav Lindgren, Alexandra Peña, Andrius Zukauskas, **Charlotte Liljestrand,** Bertrand Ménaert, Benoît Boulanger and Carlota Canalias, "Thermal Stability of ferroelectric domain gratings in Rb-doped KTP", Appl. Phys. Lett. 107, 082906 (2015)

V.   Sebastian Müller, Thomas Calmano, Philip W. Metz, Christian Kränkel, Carlota Canalias, **Charlotte Liljestrand,** Fredrik Laurell, and Günter Huber, "Highly efficient continuous wave blue second-harmonic generation in fs-laser written periodically poled $Rb:KTiOPO_4$ waveguides", Opt. Lett. 39, 1274-1277 (2014).

VI.   Loïc Deyra, **Charlotte Liljestrand**, Julien Didierjean, Carlota Canalias, Fredrik Laurell, François Balembois, and Patrick Georges, "High power single-crystal fiber CW 946 nm laser and blue generation based on Rubidium-doped PPKTP", 2013 Conference on Lasers and Electro-Optics - International Quantum Electronics Conference, (Optical Society of America, 2013)

Description of Author Contribution

My contributions to the original papers were the following:

Paper I

I fabricated the samples, did the periodic poling and the optical evaluation. I participated in the discussions and writing of the article.

Paper II

I developed the lithography system, participated in the periodic poling, optical evaluation of the samples, discussions and writing of the article.

Paper III

I developed the lithography system, participated in the periodic poling, optical evaluation of the samples, discussions and writing of the article.

Paper IV

I fabricated and periodically poled some of the samples, participated in discussions and writing of the article.

Paper V

I performed the periodic poling and participated in the optical experiments. I participated in the discussions and writing of the article.

Paper VI

I performed the periodic poling and participated in the optical experiments. I participated in the discussions and writing of the article.

Publications not Included in this Thesis

A. C. Yang , C. Lin , C. Liljestrand , W. Su , C. Canalias, C. Chuu, " Parametric down-conversion with nonideal and random quasi-phase-matching", Scientific Reports 6, 26079 (2016)

B. C. Liljestrand, F. Laurell, and C. Canalias "Coercive Field Engineering in Bulk Rb-doped $KTiOPO_4$ " Joint IEEE International Symposium on the Applications of Ferroelectrics, European Conference on Applications of Polar Dielectrics & Workshop on Piezoresponse Force Microscopy (ISAF/ECAPD/PFM 2016), Darmstadt, Germany August 21-25 (2016)

C. A. Zukauskas, C. Liljestrand, V. Pasiskevicius, F. Laurell and C. Canalias, "Progress in Fabrication of sub-µm QPM Devices in Bulk Rb-doped KTP", Europhoton 2012, Stockholm, Sweden, August 26-31 (2012)

D. F. Laurell, C. Canalias, A. Zukauskas, C. Liljestrand and V. Pasiskevicius, "Nanodomain Engineered Ferroelectrics for Nonlinear Optical Applications". Progress in Electromagnetics Research Symposium (PIERS 2013), Stockholm, Sweden, 12-15 August, (2013)

E. C. Canalias, A. Zukauskas, C. Liljestrand, V. Pasiskevicius and F. Laurell, "Sub-wavelength domain engineering in KTP isomorphs : QPM devices with counter-propagating photons", Conference on Lasers and Electro-Optics Pacific Rim (CLEO-PR 2013), Kyoto, Japan, June 30-July 4 (2013)

F. C Canalias, A. Zukauskas, C. Liljestrand, V. Pasiskevicius and F. Laurell, "Advances in QPM Devices Based on KTP Isomorphs" International Workshop on New Science and Technologies Using Entangled Photons (NSTEP2013), Osaka, Japan, July 8-9 (2013).

G. C. Liljestrand, F. Laurell and C. Canalias, "Chemical Patterning of Rubidium doped $KTiOPO_4$ for electric field periodic poling" Optics and Photonics Sweden 2014 , Gothenburg, November 11-12, (2014)

H. F. Laurell, S. Müller, T. Calmano, P. Metz, C. Kränkel, C. Canalias, C. Liljestrand, G. Huber, "A fs-laser written waveguide in periodically poled $Rb:KTiOPO_4$ for efficient second harmonic generation" 17th European Conference on Integrated Optics (ECIO-MOC 2014), Nice, France, June 24-27, (2014)

I. G. Lindgren, A. Peña, A. Zakauskas, C. Liljestrand, B. Ménaert, B. Boulanger and C. Canalias, "Thermal stability of ferroelectric domain gratings in Rb-doped $KTiOPO_4$" Advanced Solid State Lasers, (ASSL 2015), Berlin, Germany, October 4-9 (2015)

J. A. Zukauskas, C. Liljestrand, V. Pasiskevicius, and C. Canalias, "Fabrication of sub-µm ferroelectric domain gratings for counter-propagating nonlinear interactions". 5th French-German Workshop on Oxide, Dielectric, and Laser Crystals, Berlin, Germany, September 15-16 (2016)

K. C. Liljestrand, F. Laurell and C. Canalias, "Ion-Exchange Induced Coercive Field Gratings for QPM Devices in Rb-doped KTP" Conference on Lasers and Electro-Optics, (CLEO 2016), San Jose, USA, June 5-10 (2016)

L. A. Zukauskas, C. Liljestrand, A.Viotti, V. Pasiskevicius, C. Canalias, "Highly-Efficient Cascaded Mirrorless OPO in Sub-µm Periodically Poled RKTP Crystals " Conference on Lasers and Electro-Optics, (CLEO 2017), San Jose, USA, May 14-19 (2017)

M. C. Liljestrand, A. Zukauskas, V. Pasiskevicius, C. Canalias, "Mirrorless Optical Parametric Oscillator Pumped By Nanosecond Pulses" Conference on Lasers and Electro-Optics Europe, (CLEO Europe 2017), Munich, Germany, June 25-29 (2017)

Preface

The research presented in this thesis has been performed in the Laser physics group, at the department of Applied Physics at KTH (Royal Institute of Technology) in Stockholm between 2011 and 2017.

The investigation of SHG at high power was done in collaboration with the Prof. Patrick Georges group at Laboratoire Charles Fabry, Institut d'Optique, in Palaiseau, France.

The laser-written waveguides were fabricated in collaboration with Prof. Dr. Günter Huber's group at Institut für Laser-Physik, Universität Hamburg in Hamburg, Germany.

Acknowledgements

There is an African proverb saying: "*It takes a village to raise a child*". In a similar manner, supervisors, colleagues, friends and family are needed to train a PhD student to become a competent researcher, and I would like to thank my 'village' for all of their support.

First of all, I would like to express my deepest gratitude to my main supervisor Dr. Carlota Canalias for accepting me as a PhD student and guiding me on my path throughout these years. I truly appreciate the knowledge she has shared, both through interesting discussions and throughout the many hours spent in the lab. It was not a straight path, but I am truly grateful for the years we have worked together and will remember the knowledge and inspiration she has provided.

Second, I would like to thank Professor Fredrik Laurell and Professor Valdas Pasiskevicius for welcoming me as a PhD student in the Laserphysics group and for the endless support and knowledge they have provided over the years. They never seize to inspire me and keep my interest alive for nonlinear optics, and physics in general.

Apart from Carlota, Valdas and Fredrik, I would like to thank all the present and former colleagues in the Laserphysics group for their excellent company and their never-ending willingness to share knowledge and insights or just a nice cup of coffee. I would especially like to thank the following people:

- Hoda Kianirad, for being a great office mate, for the many conversations we have had about science, life and everything in-between.
- Andrius Zukauskas, for always being available to help in the lab, for always showing interest in projects and for always keeping your door open and offering to help in at all times.
- Gustav Lindgren, for all discussions about our parallel projects, KTP and so much more.
- Staffan Tjörnhammar, for the great support, friendship and shared wisdom throughout the years.
- Jens Tellefsen, for proof-reading this thesis and providing valuable knowledge of the English language.
- Hoon Jang, for being a confidant from the time we were master students, for always being a friend, and always willing to share your deep knowledge no matter day or night. And for all the sushi!

Without my dear friends, well known and anonymous, I would not be the person I am proud to be today, and for that I am eternally grateful for everyone who has appeared in my life. I would like to say a special 'thank you' to my girls Sandra, Sandra, Annika and Annette. You are always there, whenever I need a friend, and for that I cannot thank you enough.

Finally, I would like to thank my family for their support. Especially I would like to thank my mother Marianne, who endlessly supports me in all the ways possible and gives me an incredible strength in life. Without her support, nothing I have achieved would have been possible.

Contents

1 Introduction

Second order nonlinear optics is the most powerful technology for generation of coherent electromagnetic radiation at optical frequencies which are needed for a wide range of applications such as research, medicine, biology, material processing, quantum information, remote sensing, aerospace and defense applications, and optical signal processing. Second order nonlinear optical processes were first experimentally demonstrated in 1961, by second harmonic generation (SHG) in a crystalline quartz plate [1]. Since then, numerous nonlinear optical processes have been demonstrated in several materials, for generation of light from the UV to the far-IR spectral region.

In order to ensure efficient energy transfer from the pump wave to the generated waves in any optical nonlinear process, the interacting optical waves should propagate in phase throughout the nonlinear material; a condition called phase matching. However, due to the material dispersion, this condition is seldom automatically fulfilled. The most common method to obtain phase matching is to use the natural birefringence of the nonlinear material, so-called birefringent phase matching (BPM). Although widely used, BPM suffers from drawbacks such as Poynting vector walk-off and polarization dependent nonlinearity, effectively limiting the interaction length, the obtainable spectral range and the efficiency of the nonlinear process. An alternative method to obtain phase matching is the so-called quasi-phase matching (QPM). The idea behind QPM is to periodically reset the phase mismatch between the interacting waves. This method enables phase matching within the full spectral range of the material, and the possibility to utilize the largest nonlinear coefficient of the material, overcoming the drawbacks of BPM. QPM can be implemented in a variety of materials using a range of different techniques [2–4]. However, today the most extensively used and reliable method is by periodically reversing the spontaneous polarization by application of an external electric field in a ferroelectric material, so-called periodic electric field poling, or periodic poling. Typically, a periodic metal grating is fabricated through photolithography on one of the polar crystal surfaces to select the regions where domain reversal is desired as the external electric field is applied to the crystal. The poled ferroelectric domain structure is dependent on a vast amount of variables such as crystal structure, material homogeneity, pulse shape and magnitude of the applied electric field, to mention a few.

The electric field poling was first demonstrated in $LiNbO_3$ in 1993 [5]. Since then, electric field poling has been thoroughly investigated in both $LiNbO_3$ and $LiTaO_3$, two optically nonlinear materials which are inexpensive and commercially available. Problems such as large coercive fields (~21 kV/mm) and sensitivity to photorefractive damage have been alleviated by improved stoichiometry and MgO-doping of the material [6–10]. Nevertheless, $LiNbO_3$ and $LiTaO_3$ have a trigonal crystal structure which favors formation of trigonal and hexagonal domains, making it extremely challenging to fabricate domain structures with periods shorter than 6 μm for apertures larger than 500 μm which is required in most laser applications.

On the other hand, KTiOPO$_4$ (KTP) has high optical nonlinearity, excellent mechanical and thermal properties, high resistance to optical damage and does not suffer from photorefractive damage. Therefore, it is considered a superior material for frequency conversion within its optical transparency range pumped by light with wavelength of ~1 μm. The coercive field of KTP is an order of magnitude lower than that of LiNbO$_3$ [11], which, combined with the chiral crystal structure of KTP, enables fabrication of fine-pitch, large aspect-ratio QPM devices through periodic poling. Indeed, large aperture and fine-pitch QPM gratings have previously been demonstrated through electric field periodic poling in KTiOPO$_4$ (KTP) [12,13]. However, despite its excellent qualities, KTP suffers from large ionic conductivity as well as poor material homogeneity which greatly affect the quality of the periodically poled QPM structure. Moreover, the ionic conductivity of KTP has been linked to the photochromatic damage which occurs at high powers in the green and blue spectral region and is detrimental for the performance of the fabricated QPM crystals [14].

In recent years, bulk Rb-doped KTP (RKTP) with 0.3 % Rb-doping in the as-grown crystals has become commercially available and it is considered an attractive alternative for fabrication of fine-pitch QPM structures [15]. The light Rb-doping of the material results in a two order of magnitude lower ionic conductivity than for ordinary KTP, while maintaining excellent linear and nonlinear properties. The improved homogeneity of the material and the lower ionic conductivity greatly facilitates the fabrication of fine-pitch QPM gratings. Nevertheless, fabrication of sub-μm periodic domain gratings in this material remains largely unexplored. Large aperture QPM devices [16] and quasi-periodic sub-μm domain structures [17] have been demonstrated in RKTP, but fabrication of high quality sub-μm QPM structures still remains difficult [18]. The accurate control of the domain formation needed to fabricate sub-μm structures is partly obstructed by the domain broadening associated with the ionic conductivity in RKTP in combination with the fringing fields from the periodic metal electrodes used for electric field poling [19]. An attractive alternative method would be fabrication of a coercive field grating in the bulk of the RKTP crystal, which potentially would allow electric field poling using planar electrodes, thereby alleviating the domain broadening.

Sub-μm QPM devices enables nonlinear optical processes not achievable by BPM, such as nonlinear optics with counterpropagating waves. These processes, such as Mirrorless Optical Parametric Oscillation (MOPO) [13,20], backwards parametric amplification and backward second harmonic generation [17,21], are sparsely explored due to the difficulty to obtain QPM devices with the required periodicity. However, counterpropagating nonlinear processes are potentially of great interest due to their unique spectral, tuning and coherence properties [22–24] with applications such as slow-light devices [25], ultrabright biphoton sources [26], frequency translators allowing transfer of photon quantum states from one wavelength to another [27], counter-propagating optical amplifiers with the expected self-compression of the counter-propagating pulses [28], etc.

The primary aim of this thesis was to develop a reliable method for fabrication of sub-μm ferroelectric domain gratings in RKTP, and to assess the optical performance of the fabricated

QPM devices. A novel poling technique based on the fabrication of a coercive field grating, through ion exchange, in the bulk of RKTP was developed to enable fabrication of high quality sub-µm devices [paper I]. The impact of the ion exchange process on the optical performance of the QPM devices was studied for SHG, and the possibility to engineer the linear and nonlinear refractive indices was explored simultaneously. The high quality of the sub-µm PPRKTP crystals enabled not only experimental demonstration of MOPO in RKTP, but also the first experimental demonstration of cascaded MOPO [paper II] and MOPO pumped by a Q-switched laser [paper III]. In addition, QPM devices were fabricated using conventional electric field poling for studies of the domain-wall stability [paper IV] and the optical performance of PPRKTP in the blue spectral region, both in bulk crystals [paper VI] and in waveguides fabricated using laser-writing technology [paper V].

The outline of the thesis

This thesis is structured as follows: In Chapter 2, the basic concepts of nonlinear optics and QPM are presented, which provide the main incentive for fabrication of ferroelectric domain gratings. Chapter 3 discusses the principles of ferroelectricity and polarization switching in ferroelectric materials. In Chapter 4, the reader is introduced to the material RKTP and its most important properties. Chapter 5 describes the ion exchange technology in KTP isomorphs, which is a key technology for the fabrication of coercive field gratings in this work. In Chapter 6, periodic poling of RKTP is presented. Conventional electric field poling of RKTP is discussed, as well as electric field poling of RKTP crystals with an engineered coercive field grating. Finally, fabrication of sub-µm ferroelectric domain gratings in RKTP is demonstrated. Chapter 7 presents the optical performance of the fabricated PPRKTP crystals. Conventional PPRKTP crystals are evaluated for high power SHG in the blue spectral region. Laser-written waveguides are demonstrated in PPRKTP for SHG with record high power. Finally MOPO is demonstrated for the first time in PPRKTP, both in the picosecond and nanosecond regime.

2 Nonlinear optics

This chapter briefly describes and explains the nonlinear processes relevant to this research. Starting from the fundamental concepts of nonlinear optics, quasi-phase matching, second harmonic generation and parametric interactions are discussed.

2.1 Basic concepts of nonlinear optics

Light can be described as an electromagnetic wave with spatially and temporally varying field strengths. The electric, $E(t)$, and magnetic, $B(t)$, components of such a wave are orthogonal to each other as well as to the propagation direction of the light wave. As the light wave propagates in a dielectric medium, it interacts with the charged particles that constitute the material. However, in most dielectric materials, the interaction between the material and the magnetic field is so small it can be neglected compared to the impact of the electric field. From now on, only the electric field will be considered and it can be descried by the following expression:

$$E = A exp(i(\boldsymbol{kr} - \omega t)) + c.c. \, , \tag{2.1}$$

where c.c. denotes the complex conjugate, ω is the angular frequency of the light and $\boldsymbol{k}$ denotes the wavevector of the light with the magnitude given by the relations

$$|\boldsymbol{k}| = k = \frac{n\omega}{c} = \frac{2\pi n}{\lambda} \, , \tag{2.2}$$

with λ being the wavelength of light and n is the corresponding refractive index at the given wavelength.

As the light wave propagates in the dielectric material, the charged particles in the material are accelerated along with the electric field. The induced movement of the electrons is significantly larger relative to the movement of the nuclei of the atoms, as the nuclei are significantly heavier than the electrons. The separation of the charges induces a dipole moment, where the average value per unit volume is called the induced electric polarization ($\boldsymbol{P}$). The polarization is dependent both on the electric field strength as well as on the susceptibility of the material to polarization. The polarization for a quasi-monochromatic wave, not too close to an absorption resonance can be described by a power series given by

$$\boldsymbol{P} = \sum_{N=1}^{\infty} \boldsymbol{P}^{(N)} = \varepsilon_0 \sum_{N=1}^{\infty} \chi^{(N)} \boldsymbol{E}^N. \tag{2.3}$$

Here, $\boldsymbol{P}^{(N)}$ is the n-th order polarization, ε_0 the vacuum permittivity, and $\chi^{(N)}$ the n-th order optical susceptibility, a tensor of rank n +1.

At low electric field strengths, the response of the material is linear, which is the first term of the power series, $\boldsymbol{P}^{(1)}$. This term describes the linear interactions such as refractive index, n, and the linear absorption, α.

4

As the strength of the electric field is increased, as in a focused laser beam, the material will respond in a non-linear fashion, which is described by the higher order terms in the power sum. All terms with N ≥ 4 can normally be disregarded due to their relative weaknesses. The first nonlinear term, N = 2, is only nonzero for non-centrosymmetric materials. This term is extensively used in a wide range of applications for frequency converters, which will be discussed further in this thesis. Furthermore, N = 3 is the first non-zero term for centrosymmetric materials.

2.2 Second order nonlinearities

The second order nonlinearity is extensively used for a wide range of frequency conversion applications. The second order polarization, $\boldsymbol{P}^{(2)}$, allows for three electromagnetic waves to interact using the quadratic response of the induced polarization to the electric field of the light. This second order process, so-called three-wave mixing, can be described by the expression

$$\boldsymbol{P}^{(2)} = \varepsilon_0 \boldsymbol{\chi}^{(2)} \boldsymbol{E}^2. \tag{2.4}$$

When an optical field consisting of two different wavelengths is considered, and their corresponding angular frequencies, ω_1 and ω_2, respectively, the second order polarization can be rewritten as follows

$$\boldsymbol{P}^{(2)} = \varepsilon_0 \boldsymbol{\chi}^{(2)} \big(\boldsymbol{E}(\omega_1) + \boldsymbol{E}(\omega_2) \big)^2 =$$

$$
\begin{aligned}
= \varepsilon_0 \boldsymbol{\chi}^{(2)} \big[& A_1^2 e^{2i(k_1 r - \omega_1 t)} + c.c. + && \text{(SHG)} \\
& + A_2^2 e^{2i(k_2 r - \omega_2 t)} + c.c. + && \text{(SHG)} \\
& + 2 A_1 A_2 e^{i((k_1 + k_2) r - (\omega_1 + \omega_2) t)} && \text{(SFG)} \\
& + c.c. + \\
& + 2 A_1 A_2^* e^{i((k_1 - k_2) r - (\omega_1 - \omega_2) t)} && \text{(DFG)} \\
& + c.c. + \\
& + 2 (A_1 A_1^* + A_2 A_2^*). && \text{(OR)}
\end{aligned}
\tag{2.5}
$$

Each term is labelled with the process it describes: Second Harmonic Generation (SHG), Sum Frequency Generation (SFG), Difference Frequency Generation (DFG) and Optical Rectification (OR), respectively. These processes are illustrated in Fig. 2.1 along with the energy diagrams of the up-conversion processes, e.g. SHG and SFG, and the down-conversion processes, e.g. DFG.
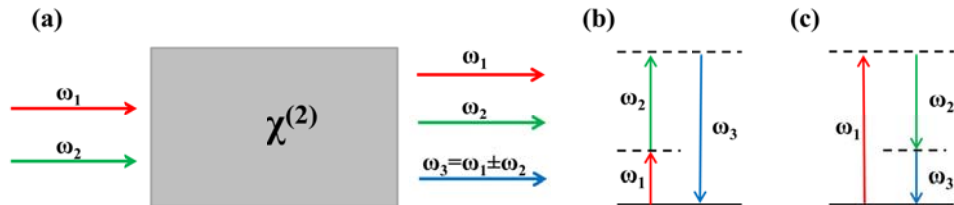

Fig. 2.1: Illustration of (a) three wave mixing and energy level diagram of (b) up conversion and (c) down conversion. The solid line represents the ground state while the dashed lines are virtual energy levels.

For each Cartesian component, the induced second order polarization, P_i $i = 1,2,3 = x,y,z$, can be rewritten as follows:

$$\boldsymbol{P}_i^{(2)}(\omega_a) = \varepsilon_0 D^{(2)} \sum_{jk} \sum_{acb} X_{ijk}(-\omega_a; \omega_b, \omega_c) E_j(\omega_b) E_k(\omega_c).$$

(2.6)

Here, the summation is performed over the electric fields with frequencies ω_b and ω_c both being positive and negative so that the sum over all involved frequencies are $-\omega_a + \omega_b + \omega_c = 0$. Thereafter, the summation is performed over all Cartesian components to obtain the polarization component P_i. $D^{(2)}$ is a degeneracy factor given by $D = 2$ if the fields E_k and E_j are distinguishable, and $D = 1$ otherwise. The tensor character of the susceptibility allows for the polarization in Cartesian coordinates to be excited by electric fields of other polarizations.

The susceptibility tensor, X_{ijk}, is a third rank tensor containing 27 different elements. However, symmetries occur that reduce the number of nonzero elements. Furthermore, if the frequencies of the optical waves in the nonlinear processes are far enough from the absorption lines, i.e., the components of X_{ijk} are frequency independent, the Kleinmann symmetry [29] is applicable and X_{ijk} can be reduced to a second order tensor, d, with the components of d given by:

$$d_{il} = \frac{1}{2} X_{ijk}^{(2)},$$

(2.7)

so that

$$d = \begin{bmatrix} d_{11} & d_{12} & d_{13} & d_{14} & d_{15} & d_{16} \\ d_{21} & d_{22} & d_{23} & d_{24} & d_{25} & d_{26} \\ d_{31} & d_{32} & d_{33} & d_{34} & d_{35} & d_{36} \end{bmatrix}.$$

(2.8)

Applying Kleinmann symmetries further reduces the number of elements to

$$d = \begin{bmatrix} d_{11} & d_{12} & d_{13} & d_{14} & d_{15} & d_{16} \\ d_{16} & d_{22} & d_{23} & d_{24} & d_{14} & d_{12} \\ d_{15} & d_{24} & d_{33} & d_{23} & d_{13} & d_{14} \end{bmatrix}.$$

(2.9)

For SFG, the nonlinear polarization for each Cartesian coordinate of the generated wave can now be described by the following:

$$\begin{bmatrix} P_x(\omega_3) \\ P_y(\omega_3) \\ P_z(\omega_3) \end{bmatrix} = 4\varepsilon_0 d \times \begin{bmatrix} E_x(\omega_1)E_x(\omega_2) \\ E_y(\omega_1)E_y(\omega_2) \\ E_z(\omega_1)E_z(\omega_2) \\ E_y(\omega_1)E_z(\omega_2) + E_z(\omega_1)E_y(\omega_2) \\ E_x(\omega_1)E_z(\omega_2) + E_z(\omega_1)E_x(\omega_2) \\ E_x(\omega_1)E_y(\omega_2) + E_y(\omega_1)E_x(\omega_2) \end{bmatrix}.$$

(2.10)

2.3 Coupled wave equations

The energy transfer between the interacting frequencies in a nonlinear process can be calculated using Maxwell's equations combined with a wave equation combining the electric field, E, and the polarization, P. For plane waves propagating in a nonmagnetic nonlinear medium with no free charges and zero currents, the wave equation can be written as:

$$\nabla^2 \mathbf{E}(\omega) + \frac{n^2}{c^2}\frac{\partial^2 \mathbf{E}(\omega)}{\partial t^2} = -\frac{1}{\varepsilon_0 c^2}\frac{\partial^2 \mathbf{P}^{NL}(\omega)}{\partial t^2} . \tag{2.11}$$

Here, the nonlinearity of the material acts as a source term for the wave equation. To illustrate how the optical waves interact with each other, SFG is considered. The light propagating in the nonlinear medium is now assumed to be three planar, monochromatic waves with angular frequencies, ω_1, ω_2 and ω_3, respectively. The two waves with angular frequency ω_1 and ω_2 are interacting with the nonlinear medium, and thereby generating a wave with frequency ω_3. For simplicity, assume that the light waves propagate in the x-direction and are polarized in the z-direction. The applied optical fields and the nonlinear source term are then given by:

$$\begin{aligned}
E_1(x,t) &= A_1 exp\big(i(k_1 x - \omega_1 t)\big) + c.c. \\
E_2(x,t) &= A_2 exp\big(i(k_2 r - \omega_2 t)\big) + c.c. \\
P_3(x,t) &= P_3 exp(-i\omega_3 t) + c.c.,
\end{aligned} \tag{2.12}$$

where $P_3 = 4\varepsilon_0 d_{eff} A_1 A_2 e^{i(k_1+k_2)x}$, with d_{eff} being the effective nonlinear coefficient correlated with the polarization of the three interacting waves. As the amplitudes of the interacting waves are assumed to change slowly compared to the wavelength of the interacting waves, the slowly-varying-envelope approximation (SVEA) can be applied, meaning that the second order derivatives can be neglected:

$$\left|\frac{d^2 A_i}{dx^2}\right| \ll \left|k_i \frac{dA_i}{dx}\right|. \tag{2.13}$$

Using Eq. (2.12), the wave equation can now be written for each of the interacting waves in the following way:

$$\frac{dA_1}{dx} = \frac{2id_{eff}\omega_1}{cn_1} A_3 A_2^* e^{i\Delta kx},$$

$$\frac{dA_2}{dx} = \frac{2id_{eff}\omega_2}{cn_2} A_3 A_1^* e^{i\Delta kx}, \tag{2.14}$$

$$\frac{dA_3}{dx} = \frac{2id_{eff}\omega_3}{cn_3} A_1 A_2 e^{-i\Delta kx},$$

where $\Delta k = k_3 - k_2 - k_1$ is the phase mismatch between the interacting waves. Eqs. (2.14) are commonly known as the *coupled amplitude equations* and they describe how the energy flows

between the interacting waves. The expressions above are specific to SFG but similar expressions are possible to derive for other second order nonlinear processes.

2.4 Phase matching

The amplitude of each wave, A_i, is obtained by solving the Eqs. (2.14) above. Thereafter, the intensity of each wave is given by the relationship:

$$I_i = \frac{\varepsilon_0 c n}{2} A_i A_i^* . \tag{2.15}$$

For planar waves, if the input amplitudes, A_1 and A_2, are approximately constant, the intensity of the generated wave is given by the expression:

$$I_3 = \frac{8 d_{eff}^2 \omega_3^2 I_1 I_2}{n_1 n_2 n_3 \varepsilon_0 c^2} L^2 sinc^2 \left(\frac{\Delta k L}{2}\right), \tag{2.16}$$

where L is the propagation distance within the nonlinear material. It can be seen that the intensity grows quadratically with the length of the propagation distance. However, the intensity of the generated beam is also highly dependent on the product of the phase mismatch and the propagation distance, $\Delta k L$. Fig. 2.2 shows the intensity as a function of $\Delta k L/2$.

The intensity has a maximum when $\Delta k L/2 = 0$, i.e. when the phase mismatch of the interacting waves is zero. As $|\Delta k L/2|$ deviates from zero the intensity decreases and reaches zero as $|\Delta k L/2| = \pm \pi$. The propagation distance where $|\Delta k L/2| = \pm \pi$ is defined as the coherence length, L_c, of the nonlinear process:

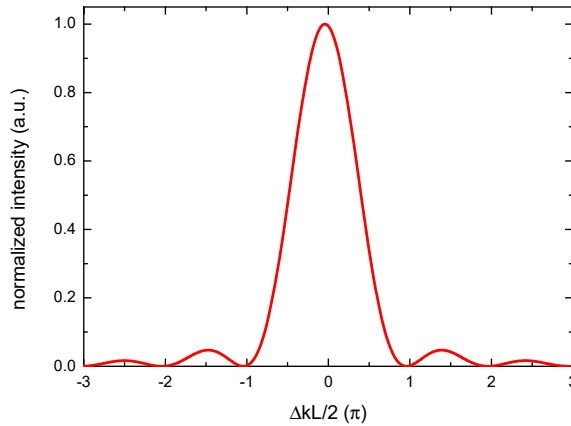$$L_c = \frac{\pi}{|\Delta k|} . \tag{2.17}$$

Fig. 2.2: Intensity of the generated wave as a function of phase mismatch.

While the propagated distance is shorter than the coherence length, energy will be flowing into the generated wave from the pumping wave(s). However, as the coherence length is reached, energy will start being transferred back to the pumping wave(s) from the generated wave. Each

8

energy transfer cycle is two coherence lengths long and the cycle will repeat itself throughout the entire length of the nonlinear material.

This fact shows that proper phase matching ($\Delta k = 0$) is essential in order to obtain an efficient nonlinear process. However, due to the dispersion of the material, this condition is normally not fulfilled. In order to obtain phase matching for a certain process, either birefringent phase matching or quasi-phase matching can be employed.

2.4.1 Birefringent phase matching

The technique of birefringent phase matching (BPM) utilizes the natural birefringence of most nonlinear optical materials, i.e., optical waves of different polarizations experience different refractive index, n, while propagating in the nonlinear material.

A wave polarized perpendicular to a plane containing the optical axis and the propagation direction experiences the *ordinary* refractive index, n_o, and is, hence, named the ordinary wave. The ordinary refractive index remains the same independent of the propagation direction in the crystal. Meanwhile, a wave polarized parallel to the plane containing the optical axis and the propagation direction experiences the *extraordinary* refractive index, n_e, and is named the extraordinary wave. The extraordinary refractive index varies with the angle, θ, between the optical axis of the crystal and the propagation direction. For a negative uniaxial crystal the extraordinary refractive index is given by [30]:

$$n_e(\theta) = \frac{n_o \bar{n}_e}{\sqrt{n_o^2 - (n_o^2 - \bar{n}_e^2)\cos^2(\theta)}}. \tag{2.18}$$

Here, $\bar{n}_e$ is the principal value of the refractive index so that $n_e(\theta) = \bar{n}_e$ for $\theta = 90°$ and $n_e(\theta) = n_o$ for $\theta = 0°$.

BPM processes are divided in two groups of phase matching, Type I and Type II. Type I phase matching occurs when the two waves with the lowest frequencies are polarized in the same direction. Type II phase matching occurs when the two lowest frequency waves are polarized orthogonally to each other [31].

Although BPM is a straightforward and a considerably simple technique, it suffers from several drawbacks. While using the correct angle to obtain phase matching for a desired nonlinear process, if this angle $\theta \neq 0,90°$, there will be a spatial walk-off between the interacting waves. The walk-off is due to the Poynting vector not being parallel to the propagation vector. This leads to a decreased spatial overlap of the interacting waves and, hence, a decreased conversion efficiency. However, if the birefringence of the material is temperature dependent, the spatial walk-off between the interacting waves can be avoided by setting the crystal angle to $\theta = 90°$ and adjust the temperature of the crystal to obtain the collinear phase matching. This technique is called noncritical phase matching. Moreover, while employing BPM it is not always possible to use all the elements of the nonlinearity tensor d. The components d_{11}, d_{22} and d_{33} are not accessible when employing BPM because of the different polarizations of the optical waves involved in the process. Finally, not all spectral regions have large enough birefringence to be phase matched making several of the nonlinear processes unachievable.

2.4.2 Quasi-phase matching

Another method to achieve phase matching is quasi-phase matching (QPM). The QPM technique is based on resetting the phase mismatch between the interacting light waves in the nonlinear process every coherence length. This is done by periodically rotating the $\chi^{(2)}$ tensor 180˚ with respect to the propagation direction, effectively inverting the sign of the nonlinear coefficient, d_{eff}, as schematically shown in Fig. 2.3. The idea of QPM was proposed by Armstrong *et al.* in 1962 [32] and demonstrated for the first time in 1966 [33], a few years after BPM was demonstrated [34,35].
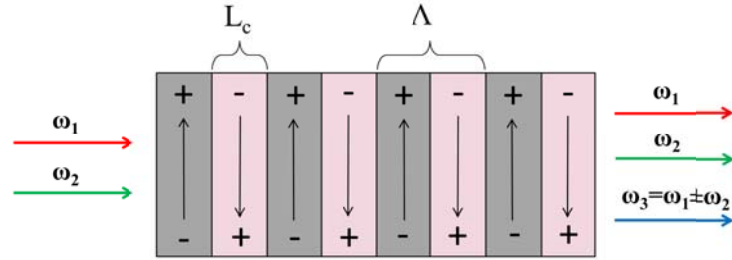

Fig. 2.3: Illustration of the periodically poled crystal used for three wave mixing.

QPM in ferroelectric crystalline materials is realized by periodically inverting the spontaneous polarization of the material, thereby inverting the nonlinear coefficient, d_{eff}. This can be done in the growth process of the crystal [36–38], or more commonly through so-called periodic poling. During the periodic poling, an electric field is applied over a periodic electrode to selectively invert the spontaneous polarization. This makes it possible to engineer any nonlinear optical interaction within the full transparency range of the material, which is the main advantage of QPM.

With the effective nonlinearity, d_{eff}, now being spatially dependent on the *x*-coordinate, the coupled-wave equation Eqs. (2.14), must be adjusted to the following expression:

$$\frac{dA_3}{dx} = \frac{i\omega_3}{n_{3c}} d_{eff}(x) A_1 A_2 e^{-i\Delta kz}. \tag{2.19}$$

The spatially varying d_{eff} can now be expressed as a Fourier series in the following way:

$$d_{eff}(x) = d_{il} \sum_{m=-\infty}^{\infty} G_m e^{iK_m x}, \tag{2.20}$$

where d_{il} are given by the matrix elements in Eq. (2.9) and the m-th grating vector, K_m, is given by:

$$K_m = \frac{2\pi m}{\Lambda}, \tag{2.21}$$

and the Fourier coefficients G_m are defined as:

$$G_m = \frac{2}{m\pi} \sin(m\pi D),$$ (2.22)

where Λ is the period of the d_{eff} grating, D being the duty-cycle of the grating, $D = l/\Lambda$, with l being the length of the inverted spontaneous polarization. The impact of the duty-cycle on the effective nonlinearity, d_{eff}, is shown in Fig. 2.4 for $m = 1,2,3$. As can be seen, the largest nonlinearity, and therefore, the most efficient nonlinear process, is obtained for first order phase matching with $m = 1$ and with $D = 0.5$.

With $D = 0.5$ the Fourier coefficients G_m are now given by the following:

$$G_m = \begin{cases} 0, & \textit{for even } m \\ \dfrac{2}{m\pi}, & \textit{for odd } m \end{cases}$$ (2.23)

and the effective nonlinearity:

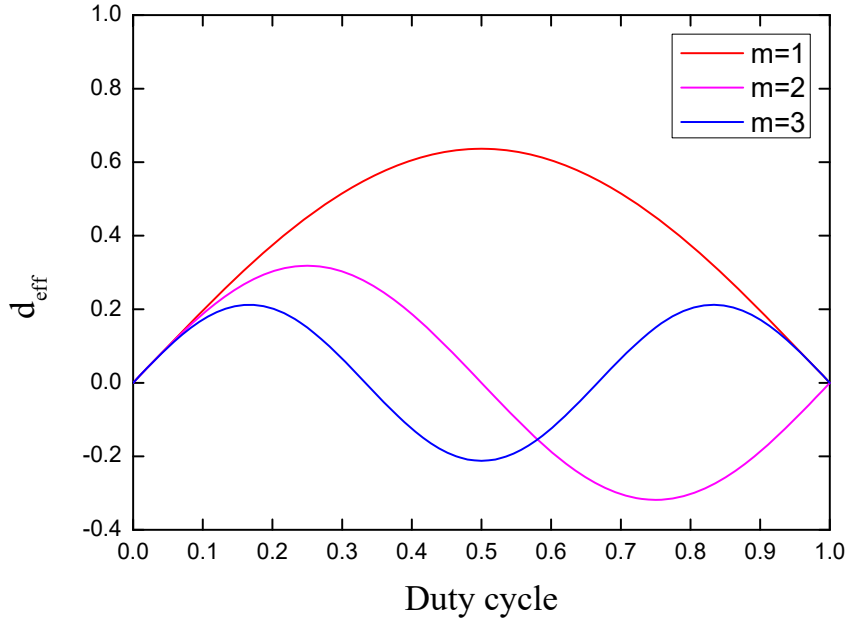$$d_{eff} = d_{il} \frac{2}{m\pi}.$$ (2.24)

Fig. 2.4: The normalized effective nonlinearity as function of duty-cycle.

Although the nonlinear coefficient is now scaled with a factor of $2/\pi$, QPM can yield significantly effective nonlinearity than BPM, as shown in Fig. 2.5. QPM normally operates in what is called Type 0 phase matching, where all the interacting waves have the same polarization. Therefore, the diagonal nonlinear coefficients, d_{11}, d_{22} and d_{33}, are all accessible using this technique. These diagonal coefficients are normally the largest ones in the nonlinear tensor, d.

11

Perfect phase matching, $\Delta k_{QPM} = 0$, for a given process, can only be achieved for one value of m. However, the non-phase-matched higher order Fourier components causes the intensity of the generated wave to grow oscillatory, as can be seen in Fig. 2.5.

The phase mismatch of the nonlinear process can now be expressed as:

$$\Delta k_{QPM} = k_3 - k_2 - k_1 - K_m. \tag{2.25}$$

From Eq. (2.25), and the requirement for perfect phase matching for a nonlinear process to be efficient, the grating period can now be expressed as follows:

$$\Lambda = 2L_c = \frac{m}{\dfrac{n_3}{\lambda_3} - \dfrac{n_2}{\lambda_2} - \dfrac{n_1}{\lambda_1}}, \tag{2.26}$$

where the refractive indices, n_i, can be obtained from the Sellmeier equations for the given material.
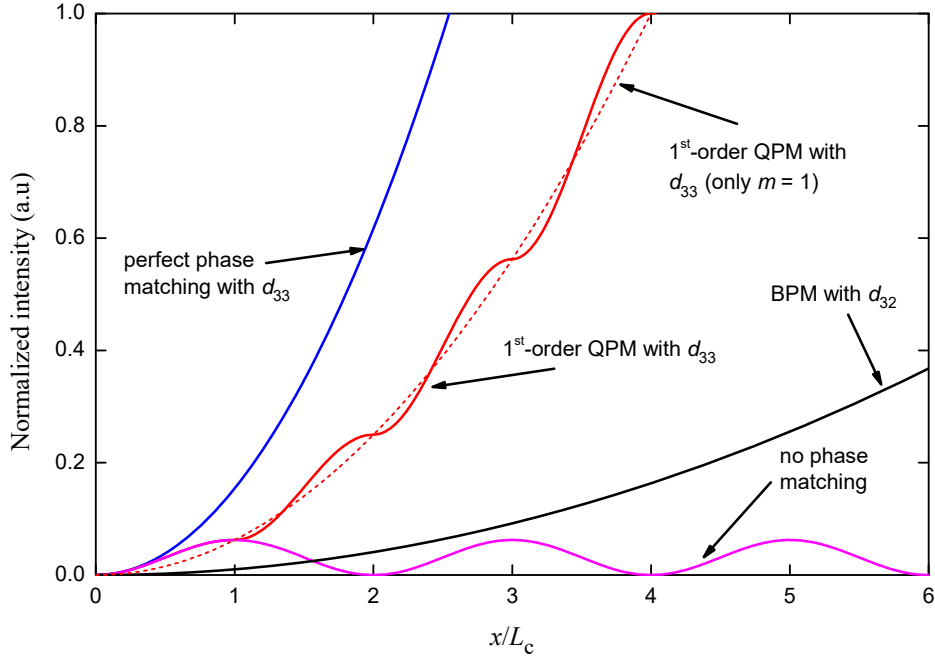

Fig. 2.5: Comparison of different phase matching conditions in a KTiOPO$_4$ crystal for a nonlinear frequency conversion process.

2.5 QPM Second Harmonic Generation

Second Harmonic Generation (SHG) is the $\chi^{(2)}$ nonlinear process where two pump photons are converted into one photon with the double energy, $\omega_{SH} = 2\omega_F$ ($\omega_1 = \omega_2 = \omega_F$, $\omega_3 = \omega_{SH}$), and at one half of the pump wavelength, $\lambda_{SH} = \lambda_F/2$. This process is extensively used for frequency conversion of light in the near infrared range into light in the visible range. The phase mismatch in this process is given by the expression:

$$\Delta k_{QPM} = k_{SH} - 2k_F - K_m \,. \tag{2.27}$$

When the process is phase matched ($\Delta k = 0$), the grating period can be deduced as:

$$\Lambda_{SHG} = 2L_c = \frac{m\lambda_F}{2(n_{SH} - n_F)} \,. \tag{2.28}$$

2.5.1 Tuning and tolerances

Although QPM is a robust technology, with several advantages over BPM, it is sensitive to various parameters such as wavelength, temperature and angle [39]. From Eq. (2.16) the full-width-half-maximum of the output power can be calculated as the following expression:

$$\frac{\Delta k L}{2} = 0.4429\pi. \tag{2.29}$$

This expression can now be expanded as a function of wavelength, angle or temperature, from which the wavelength acceptance bandwidth, angular acceptance bandwidth and temperature acceptance bandwidth also can be found.

The angular acceptance bandwidth for a QPM device can be deduced from Eq. (2.29) as [39]:

$$\Delta\theta = 2\sqrt{1.772 \frac{n_2}{n_1} \frac{L_c}{L} cos\theta} \,. \tag{2.30}$$

Altering the temperature of the QPM device can be employed for tuning of the phase matching condition. Temperature changes will alter the refractive index as well as change the QPM period due to thermal expansion. The temperature tuning bandwidth is given by [39]:

$$\Delta T = \frac{0.4429\lambda_F}{L} \left| \frac{\partial n_{SH}}{\partial T} \right|_{T_0} - \frac{\partial n_F}{\partial T} \bigg|_{T_0} + \alpha(n_{SH} - n_F) \bigg|^{-1} . \tag{2.31}$$

Changing the temperature can also be used to evaluate the uniformity of the QPM structure. From Eq. (2.29), the wavelength acceptance bandwidth can be derived as [39]:

$$\Delta\lambda_{FWHM} = \frac{0.4429\lambda}{L} \left| \frac{n_{SH} - n_F}{\lambda} + \frac{\partial n_F}{\partial\lambda} - \frac{1}{2}\frac{\partial n_{SH}}{\partial\lambda} \right|^{-1} . \tag{2.32}$$

The wavelength acceptance bandwidth provides information on the bandwidth limitations of the fundamental laser source that can be used in the nonlinear process.

2.5.2 SHG with Gaussian beams

Lasers generally have a Gaussian intensity distribution. When such a beam is being focused into, e.g., a nonlinear crystal, the depth of the focus is limited by diffraction of the beam. The amount of diffraction spread increases as the beam waist in the focus is decreased. With this trade-off in mind, between interaction length and beam size, Boyd and Kleinmann [40] derived the following expression of the second harmonic conversion efficiency as follows:

$$\eta = \frac{2d_{eff}^2 \omega_F^2 k_F P_F}{\pi \varepsilon_0 n_F^2 n_{SH} c^3} L h(B, \xi).$$

<div align="right">(2.33)</div>

Here, $h(B,\xi)$ is the Boyd-Kleinmann focusing factor, $\xi = L/b$ where $b = 2\pi n_F w_0^2/\lambda$ is the confocal parameter for a beam waist of w_0.

For noncritical phase matching, i.e., with no spatial walk-off $B = 0$, there is a maximum in the efficiency, η, for the parameters $\xi = 2.84$ and $h(B,\xi) = 1.068$. However, the second harmonic conversion efficiency remains within 10 % of this maximum value for the range $1.52 < \xi < 5.3$.

Normalizing the conversion efficiency, η, with respect to the device length, L, and the input power, P, makes it possible to compare the performance of different QPM devices:

$$\eta_{norm} = \frac{2d_{eff}^2 \omega_F^2 k_F}{\pi \varepsilon_0 n_F^2 n_{SH} c^3} h(B, \xi) \, .$$

<div align="right">(2.34)</div>

Another measure of the quality of the QPM device is the effective nonlinear coefficient, d_{eff}, which is given by the expression:

$$d_{eff} = \sqrt{\frac{\pi \varepsilon^3 n_F^2 n_{SH} P_{SH} m^2}{2\omega_1^2 k_1 P_F^2 L h(B, \xi)}} \, .$$

<div align="right">(2.35)</div>

2.5.3 SHG in waveguides

In an optical waveguide, the light is propagating being confined in a region of the material with an increased refractive index [41]. Such a refractive index increase can be obtained by, e.g., alteration of the material composition or be stress-induced [41–43]. The transverse intensity distribution of the light propagating in the waveguide is given by the so-called *modes*, i.e., the eigenstates of the light in the waveguide, which are determined by the waveguide shape, its dimensions and the wavelength of the propagating light. The confinement of the light propagating in the waveguide enables propagation over long distances without suffering from diffraction. A typical example of such a waveguide, which is extensively used in modern photonics, is the optical fiber, where the light in the fiber typically is propagating in a high refractive index core [44].

Waveguides made from a nonlinear material can be employed for efficient frequency conversion of pump sources of low or moderate powers, as the necessary high intensities can be obtained in the waveguide. The efficiency of a SHG process in a waveguide is given by the expression:

$$\eta = \frac{8\pi^2 d_{eff}^2 P_F}{c \varepsilon_0 n_{SHG} n_F^2 A_0} L^2,$$

<div align="right">(2.36)</div>

where A_0 is the so-called *overlap area* of the fundamental beam and the second harmonic defined by [45]:

$$A_0 = 1 \Bigg/ \left(\frac{\iint_{-\infty}^{\infty} F_{SHG}(y,z) F_F^2(y,z) dy dz}{[\iint_{-\infty}^{\infty} F_{SHG}^2(y,z) dy dz]^{\frac{1}{2}} \iint_{-\infty}^{\infty} F_F^2(y,z) dy dz} \right)^2 . \tag{2.37}$$

Here, F_{SHG} and F_F are the transverse intensity distributions of the second harmonic and fundamental beam, respectively.

It can be observed that the conversion efficiency is inversely proportional to the overlap area. The conversion efficiency is therefore maximized by minimizing A_0, i.e., by optimizing the spatial overlap of the interacting waves, and minimizing their respective mode areas.

2.6 Optical Parametric Oscillation

Optical parametric oscillation (OPO) is a nonlinear process converting one input wave, most often named the pump, into two lower energy waves, named the signal and the idler. The frequencies of these waves are correlated by the expressions $\omega_p = \omega_s + \omega_i$ and $\omega_p > \omega_s > \omega_i$. This process is commonly used to generate light in the mid- and far-infrared spectral ranges.
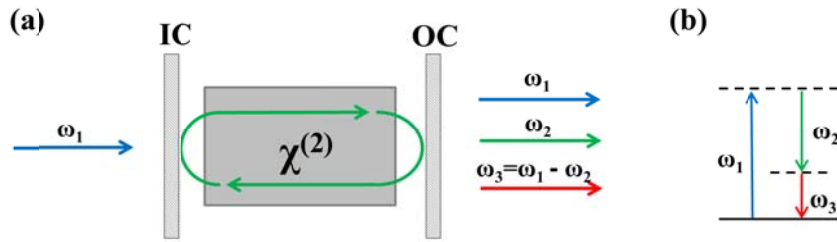

Fig. 2.6: Illustration of Optical Parametric Oscillator (a) and the energy diagram of the nonlinear interaction (b). Note that the energy diagram for OPO/OPG is the same as for DFG.

In its simplest form, the OPO consists of a nonlinear material and two mirrors, the resonator, in a linear configuration, as illustrated in Fig. 2.6. The two mirrors are commonly called the input coupler (IC) and the output coupler (OC), respectively. The input coupler is highly reflective while the output coupler is partially reflective to provide feedback for the signal and/or idler. The feedback lowers the interaction threshold, increases the conversion efficiency and decreases the bandwidth of the generated waves compared to Optical parametric generation (OPG), also called DFG, in which case no resonator is used. If the resonator is reflective for one of the parametric waves, the process is called a singly resonant OPO (SRO). This is the most widely used configuration due to its superior stability. There are configurations where both of the parametric waves are resonated in the resonator, then called a doubly resonant OPO (DRO). It is also possible to resonate both the pump wave and the two generated waves in the resonator in a so-called triply resonant OPO (TRO). The DRO and TRO systems require active stabilization of the resonator to maintain resonance and are sensitive to small fluctuations of the pump frequency and the ambient temperature.

The frequencies of the parametric waves can be tuned to any pair of $\omega_p = \omega_s + \omega_i$ as long as the phase-matching condition, $\Delta k = 0$, is fulfilled. This can be done by altering the temperature

of the nonlinear material, rotation of the crystal, tuning of the pump wavelength or by rotation of the resonator.

From the coupled amplitude equations, Eqs. (2.14), the Manley-Rowe relations can be derived [46]. It describes the energy flow between the three interacting fields through the relationship:

$$-\frac{1}{\omega_p}\frac{dI_p}{dz} = \frac{1}{\omega_s}\frac{dI_s}{dz} = \frac{1}{\omega_i}\frac{dI_i}{dz}. \tag{2.38}$$

By integrating the coupled amplitude equations in the non-depleted pump approximation, the single-pass amplification for a parametric device of length L can be written as follows:

$$\frac{I_{(L)}}{I_{(0)}} = 1 + \Gamma^2 \frac{\sinh^2\left(L\sqrt{\Gamma^2 - \left(\frac{\Delta k}{2}\right)^2}\right)}{\Gamma^2 - \left(\frac{\Delta k}{2}\right)^2}, \tag{2.39}$$

when assuming that the incident signal wave is weak and that the depletion of the pump is low. Here, the parameter Γ^2 is defined as:

$$\Gamma^2 = \kappa I_p,$$

$$\kappa = \frac{8\pi^2 d_{eff}^2}{\epsilon_0 c n_p n_s n_i \lambda_s \lambda_i}. \tag{2.40}$$

The pump energy threshold for an SRO, operating with nanosecond pulses, is given by the expression [47]:

$$\mathcal{E}_{th} = \frac{0.6(w_p^2 + w_s^2)}{\kappa L^2}\left[\frac{25l}{\tau c} + \frac{1}{2}\ln\frac{2}{R(1-A)}\right]^2, \tag{2.41}$$

where R is the reflectivity of the output coupler, A accounts for the losses in the cavity, τ is the FWHM of the pulse length, L is the crystal length, l the optical cavity length, w_p and w_s are the mode radius of the pump and the signal, respectively. When the threshold is reached and the OPO is operating, the signal and the idler will deplete the pump source so that the gain and the losses in the process are equal.

As a measure of how well the OPO is working, both the pump depletion and the efficiency of the OPO can be measured. The efficiency of the OPO is given by the expression:

$$n_{eff} = \frac{\mathcal{E}_s^{out} + \mathcal{E}_i^{out}}{\mathcal{E}_p^{out}}. \tag{2.42}$$

Here, $\mathcal{E}$ is the measured energy of each of the interacting waves. If the energy of the signal or the idler is not measured, it can be calculated from the expression $\mathcal{E}_i = \mathcal{E}_s \lambda_s / \lambda_i$ ($\mathcal{E}_s = \mathcal{E}_i \lambda_i / \lambda_s$) from the Manley-Rowe relation, Eq. (2.38).

The nonlinear loss of the pump in the OPO process is named the *pump depletion*. It is measured by comparing the total loss of the pump energy in the process to the linear loss of the pump energy below the oscillation threshold. By letting $\mathcal{E}^*$ denote the measured energy below threshold, the pump depletion can be written:

$$\eta_{depl} = 1 - \frac{\mathcal{E}_p^{out}}{\mathcal{E}_p^{in}} \frac{\mathcal{E}_p^{*in}}{\mathcal{E}_p^{*out}}.$$

<div align="right">(2.43)</div>

In an ideal OPO, every depleted pump photon is transferred by the nonlinear process into one signal-and-idler pair of photons. Ideally, the pump depletion should equal the efficiency of the OPO. In reality, there are often losses due to scattering and diffraction in the resonator, so that the pump depletion is usually higher than the efficiency of the OPO.

The maximum conversion efficiency of the OPO is limited by back-conversion of the signal and the idler waves to the pump beam [48]. The back-conversion stems from the high signal intensity resonating in the OPO cavity at high pump powers, exceeding the pump intensity due to the depletion of the pump beam, and resulting in an energy flow from the parametric waves back to the pump beam. Analytically, it has been shown that the maximum conversion efficiency of the OPO is obtained at approximately 2.5 times above the oscillation threshold given by Eq. (2.41), which agrees well with the experimental observations [49,50].

2.7 Mirrorless Optical Parametric Oscillation

Mirrorless optical parametric oscillation (MOPO) is a unique nonlinear process where naturally counterpropagating signal and idler waves are generated by down-conversion. In contrast to a conventional co-propagating OPO, the MOPO has no external cavity providing feedback to the process, but, instead, the feedback is established internally in the nonlinear material by the parametric wave counterpropagating with respect to the pump wave, as illustrated in Fig. 2.7 (a). This is similar to distributed-feedback (DFB) lasers, where the feedback is provided by Bragg reflection from the periodic modulation of the propagation constant [51,52]. However, in contrast to the DFB lasers, the MOPO is truly mirrorless, as the feedback is a result of the phase matching rather than a reflection of either of the involved waves.

However, to realize the MOPO process, a large phase mismatch between the interacting waves needs to be compensated for, as illustrated in Fig. 2.7 (b). This large phase mismatch is typically not available by birefringence in most materials, for the generation of wavelengths in the visible, near-IR and mid-IR part of the spectrum. Therefore, QPM is the most viable method to practically realize the MOPO process. However, the periodicity required of the QPM device to obtain phase matching is of the order of one half of the wavelength of the counterpropagating wave. Due to the challenge of fabricating QPM devices with sub-µm periods, the experimental demonstration of the MOPO waited 41 years [13] from when it was first suggested in 1966 [20].
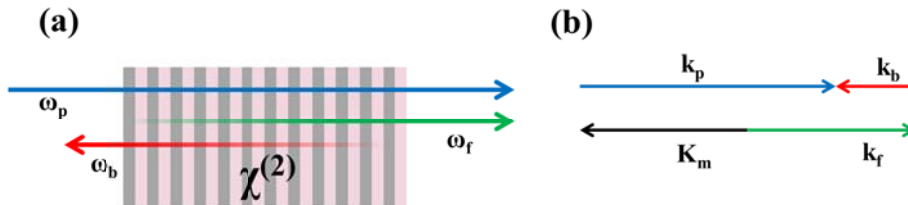

Fig. 2.7: (a) Schematic illustration of the MOPO and (b) diagram of the phase matching condition.

In the MOPO process, the energy flow between the pump and the two parametric waves can be described by the coupled wave equations. Assuming that the MOPO operates with planar and monochromatic waves, the coupled wave equations for the MOPO process are given by the expressions:

$$\frac{dA_f}{dx} = \frac{2id_{eff}\omega_f}{cn_f} A_p A_b^* \,,$$

$$\frac{dA_b}{dx} = -\frac{2id_{eff}\omega_b}{cn_b} A_p A_f^* \,,$$

(2.44)

$$\frac{dA_p}{dx} = \frac{2id_{eff}\omega_p}{cn_p} A_f A_b \,.$$

The MOPO oscillation is established once the counterpropagating parametric wave has reached sufficient intensity while propagating in the material. The pump intensity at threshold for the MOPO process can be derived by solving Eqs. (2.44) in the non-depleted pump regime, with the boundary conditions $A_f(0) = 0$ and $A_b(L) = 0$, as [53]:

$$I_{p,th} = \frac{\varepsilon_0 c n_p n_f n_b \lambda_f \lambda_b}{2L^2 d_{eff}^2} \,.$$

(2.45)

Once above the threshold, the pump wave is converted into the signal and the idler waves while the pump and counterpropagating waves are spatially overlapping in the QPM device. However, it should be noted that the generated co- and counterpropagating waves do not overlap spatially in the device, thereby preventing up-conversion back to the pump wavelength. Furthermore, the assumption of monochromatic and planar waves is indeed a simplification, and more accurate calculations require numerical modelling, as performed by Strömqvist *et al.* [23].

For the MOPO process, the QPM condition, illustrated in Fig. 2.7 (b), is given by the expression:

$$k_p = K_m + k_f - k_b \,.$$

(2.46)

Here, the indices $i = p,f,b$ correspond to the pump, the forward/co-propagating wave and the backward/counterpropagating waves, respectively.

From the QPM condition and the energy conservation requirement, the wavelength of the generated counterpropagating wave can be expressed as:

$$\frac{1}{\lambda_b} = \frac{1}{n_f - n_b}\left(\frac{1}{\Lambda} - \frac{n_p - n_f}{\lambda_p}\right) \,.$$

(2.47)

It is worth observing that the generated wavelengths of the MOPO are dependent on the pump wavelength and the dispersion of the material, as well as on the period of the QPM grating. For KTP, the contribution of the QPM grating is typically much larger than the contribution of the pump wavelength and the dispersion, resulting in a strong dependence on the QPM grating

period. In contrast, due to the energy conservation requirement, the dependence of the co-propagating wave is the opposite, being mainly dependent on the pump wavelength and the dispersion of the material.

The spectral properties of the generated parametric waves can be considered by studying the impact of the pump spectrum on the generated forward and backward propagating parametric waves, which can be derived by differentiating the QPM condition with respect to the pump wavelength, resulting in the relations:

$$\frac{\partial \omega_f}{\partial \omega_p} = \frac{v_{gf}(v_{gb} + v_{gp})}{v_{gp}(v_{gb} + v_{gf})} \equiv 1 + \varepsilon_1 \,,$$

$$\frac{\partial \omega_b}{\partial \omega_p} = \frac{v_{gf}(v_{gb} - v_{gp})}{v_{gp}(v_{gb} + v_{gf})} \equiv -\varepsilon_1 \,.$$

(2.48)

Here, ε_1 is introduced as a dimensionless parameter measuring the group velocity difference between the pump wave and the co-propagating parametric wave. For any given values of the group velocities, the values of the derivatives are significantly different, as indicated by the minus sign. Moreover, if the dispersion of the material is low, as e.g., in KTP, then $|\varepsilon_1| \ll 1$, indicating that the frequency of the co-propagating wave changes along with the frequency of the pump wave while the frequency of the counterpropagating wave remains essentially constant. Therefore, the relations between the temporal phases of the counterpropagating, the co-propagating, and the pump waves in the MOPO can be expressed as:

$$\partial_t \phi_b \simeq 0 \,,$$
$$\partial_t \phi_f \simeq \partial_t \phi_p \,.$$

(2.49)

The temporal phase of the counterpropagating wave is slowly varying compared to that of the co-propagating and the pump waves. Also, the phase of the pump wave will be coherently transferred to the generated co-propagating parametric wave in the MOPO process. When strict equality applies in Eq. (2.49), the phase of the counterpropagating wave is constant. Therefore, the bandwidth of the counterpropagating wave is then determined by the pulse length, as it is transform limited. Moreover, from Eq. (2.48) it can be seen that the counterpropagating wave contains approximately $|\partial \omega_b / \partial \omega_p| / |\partial \omega_f / \partial \omega_p| \simeq |\varepsilon_1|$ times the frequency content of the co-propagating wave, thereby further proving a very narrow bandwidth of the counterpropagating wave. These unique spectral properties are a result of the counterpropagating geometry of the MOPO, and have been experimentally verified by Strömqvist *et al.* [22,23].

With the wavelength of the counterpropagating wave being mainly dependent on the QPM grating (Eq. (2.47)) and the spectral content being mainly transferred to the co-propagating wave (Eq. (2.49)) in the MOPO process, the tuning with respect to temperature and angle of the counterpropagating wave in the MOPO is limited [13,22,23]. Meanwhile, the co-propagating wave will be tuned according to the pump wave to maintain the energy conservation condition and the phase matching condition.

3 Ferroelectricity

In this chapter, the basic concepts of ferroelectricity and polarization switching that are relevant to this research will be introduced.

3.1 Ferroelectric materials

A crystalline material can be described as a material with all its constituents arranged in a highly ordered manner, forming a crystal lattice which extends in all directions of the crystal. The *unit cell* is the smallest recognizable pattern in the crystal lattice. The composition of the unit cell governs the electrical as well as the optical properties of a crystalline material.

Crystalline materials can be divided into point groups depending on their response to symmetry operations, such as translations, rotations and reflections, which map the crystal back on itself. Out of the total 32 point groups, 11 are centrosymmetric, i.e., the center of the positive and the negative charges coincide [54]. Of the non-centrosymmetric 21, groups 20 are *piezoelectric*. Piezoelectric materials exhibit an electric polarization along a certain direction when a mechanical stress is applied to the material. The induced polarization is proportional to the magnitude of the applied mechanical stress. Moreover, when an electric field is applied to the crystal, a stress is induced in the material causing it to contract or expand.

Of the 20 piezoelectric groups, 10 are so-called *pyroelectrics*. Pyroelectric materials exhibit a polarization of the material for a certain range of temperatures when an applied electric field is not present, so-called *spontaneous polarization*, P_s, Due to P_s originating from the dipole moment, caused by the separation of the charges in the crystal unit cell, this groups of materials are called *polar materials*. Moreover, pyroelectric materials develop a surface charge as the material is heated or cooled due to the change of polarization with the temperature, and the conduction in the crystal can most often not compensate for this change. The *ferroelectric materials* are a subgroup of the pyroelectric materials, as illustrated in Fig. 3.1. In a ferroelectric material, P_s can be reversed or reoriented by an applied electric field [55]. The possible directions of the P_s are called *orientation states*. All orientation states of the ferroelectric material have the same crystalline structure, but differ in the direction of P_s in the absence of an applied electric field.

As mentioned above, P_s is temperature dependent and above a certain temperature ferroelectric materials undergo a phase transition into a paraelectric phase where $P_s = 0$. The temperature at which this phase transition occurs is called the Curie temperature, T_c. This phase transition can be classified in two groups. When P_s disappears abruptly at T_c, the phase transition is defined as a first order phase transition, e.g. in $BaTiO_3$ [56]. The phase transition is classified as a second order transition if P_s decreases continuously to the point where it disappears, e.g. in $KTiOPO_4$ [57].
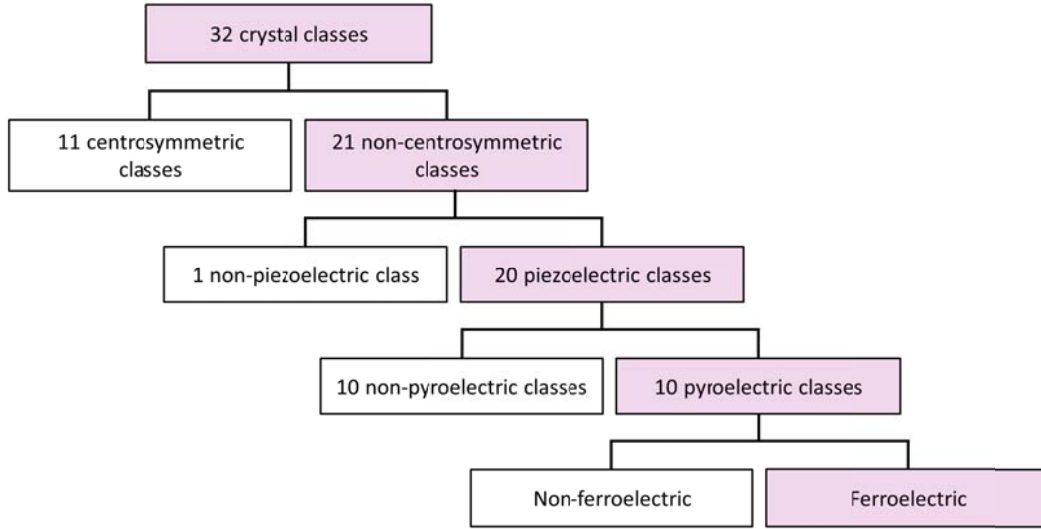
Fig. 3.1: Classification of ferroelectric materials.

The temperature dependence of P_s allows for a thermodynamic description of the system. This thermodynamic approach makes it possible to study several properties of the ferroelectric materials, without considering the microscopic mechanisms. The above mentioned phase transition can, no matter the order, be described as the one that minimizes the free Gibbs energy of the system. Assuming that all stresses are zero, that the polarization and the electric field are only along one crystallographic axis, and the non-polar phase is centrosymmetric, the elastic Gibbs function can be expressed in a polynomial form:

$$G = G_0 + \frac{\alpha}{2}P^2 + \frac{\beta}{4}P^4 + \frac{\gamma}{6}P^6, \tag{3.1}$$

where P is the polarization and α,β and γ are temperature dependent coefficients. The Gibbs free energy is qualitatively sketched for $T < T_c$, $T = T_c$ and $T > T_c$ in Fig. 3.2. The stable phases are obtained when the Gibbs free energy is minimized with respect to the polarization. As seen in Fig. 3.2, below the critical T_c Eq. (3.1) has two minima where $P_s \neq 0$, corresponding to the equilibrium values of the ferroelectric phase. As the temperature equals or exceeds T_c only one minimum can be found, corresponding to the paraelectric phase. The minimum(s) of Eq. (3.1) are found by differentiating with respect to P:

$$\frac{\partial G}{\partial P} = E = \alpha P + \beta P^3 + \gamma P^5, \tag{3.2}$$

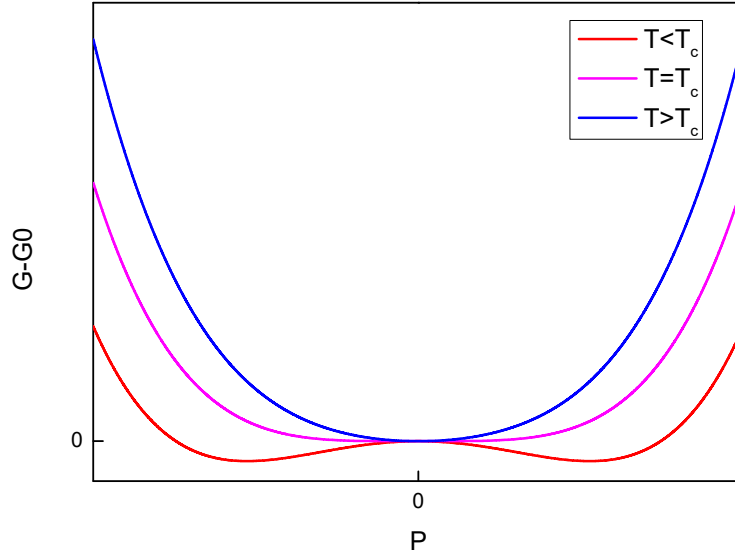and solving for $E = 0$, where E is the electric field.

Fig. 3.2: Gibbs free energy as function of the polarization below, at and above Tc.

The electric displacement in a material as an effect of the applied electric field and the polarization given by the expression:

$$D = \varepsilon E + P \, .$$

(3.3)

Given Gauss law, the free charge density ρ in a material is given by:

$$\nabla \cdot D = \rho \, .$$

(3.4)

Using Eq. (3.3) and Eq. (3.4) for a ferroelectric crystal resulting in:

$$\nabla \cdot E = \frac{1}{\varepsilon \varepsilon_0} \rho - \nabla \cdot P_s \, .$$

(3.5)

Assuming the crystal is perfect and of infinite dimensions, $\nabla \cdot P_s = 0$. In reality crystals are not infinitely large and often contain defects. At any discontinuities, e.g., at the crystal surface or due to a defect in the crystal, $\nabla \cdot P_s \neq 0$, and a charge will be present at the position of the discontinuity. This charge is called a *bound charge*, and gives rise to an electric field, the so-called *depolarization field*, oriented antiparallel to the spontaneous polarization [56]. The depolarization field can be compensated for by internal or external charges, or by creation of regions with antiparallel direction of P_s.

A region in a ferroelectric material with the same orientation spontaneous polarization is called a *ferroelectric domain* [55]. The boundary between two adjacent antiparallel ferroelectric domains is called a *domain wall*. As the crystal transitions from the non-polarized paraelectric state to the ferroelectric state, the crystal forms domains to minimize the energy from the depolarization field and the strong elastic fields within the crystal.

3.2 Polarization reversal

One important feature which distinguishes ferroelectrics from other pyroelectrics is the possibility to reverse and reorient the spontaneous polarization with an applied electric field. The response of the polarization to an electric field in a ferroelectric, Eq. (3.2), at a constant temperature, below T_c, can be described by the hysteresis loop, i.e. a *P-E* curve. A standard hysteresis for a ferroelectric material is shown in Fig. 3.3. The polarization of the material is saturated at large electric fields, with all the dipoles in the material aligned along the direction of the electric field, as for a standard dielectric material. The magnitude of the P_s is given at large electric fields, as indicated in Fig. 3.3. The polarization attains a non-zero value called the remnant polarization, P_r, as the magnitude of the electric field is decreased to $E = 0$. When the electric field is absent, some dipoles return to their original reversed state due to internal stresses in the material. Therefore, P_r is normally smaller than P_s. To change the polarization from P_r to zero the value of the applied electric needed is called the coercive field, E_c. E_c depends of a number of parameters such as temperature, electrodes, waveform and frequency of the electric field, pressure, etc. By application of an electric field with magnitude larger than E_c it is possible to change the direction of P_s, so-called *poling*. The energy required to twice change the direction of P_s is given by the area under the loop in Fig. 3.3.
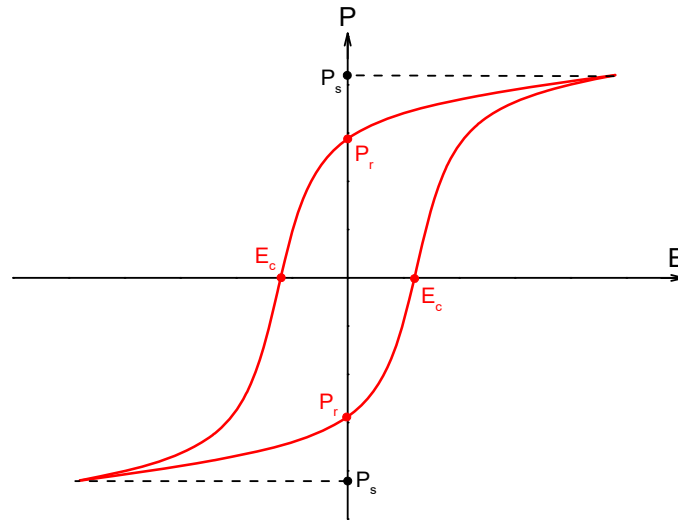

Fig. 3.3: A typical hysteresis loop for a ferroelectric material.

The process of polarization reversal can be described by the following four steps: nucleation of an antiparallel domain, expansion along the polar axis, lateral growth and finally merging of domains. Nucleation of new antiparallel domains is normally considered a statistical effect, with the probability to nucleate a new domain exponentially proportional to the applied electric field [58]. According to the theory developed by Merz [59] and Landauer [60], nucleation of a new domain yields a total energy change given by

$$\Delta W = W_w + W_E - \boldsymbol{D} \cdot \boldsymbol{E}V, \qquad (3.6)$$

where W_W and W_E are the domain wall and depolarization energy , respectively of the nucleus. **D·E**V is the electrostatic energy of the nucleus of volume V in the applied electric field E. With the assumption that within the nucleus both the polarization and the electric field are uniform, the rate of nucleation is proportional to *exp(-ΔW/kT)*. The probability to nucleate domains due to thermal fluctuations in the bulk of the crystal is small due to the large energy required. The energy required to nucleate new domains is significantly smaller at the surfaces, by defect sites or by walls of already existing domains. The Landauer theory does assume an ideal insulating ferroelectric crystal containing no defects or free carriers. In order to account for defect assisted nucleation several theories have been developed to extend the Landauer theory [61,62]. Today, the most accepted model of domain nucleation is the one by Gerra *et al.* [63]. This model includes the ferroelectric-electrode coupling and defects in its interface, and the nucleated domains have the shape of prolate semispheroids. Eq (3.6) can now be adjusted to:

$$\Delta W = W_w + W_E - \boldsymbol{D} \cdot \boldsymbol{E}V - \pi \xi P_s r^2, \qquad \textbf{(3.7)}$$

with r being the base radius of the domain, and ξ being the local surface field.

Following nucleation of an antiparallel domain, the domain will grow along the polar and the lateral directions. Along the polar axis the growth velocity normally follows an inverse exponential dependence on the electric field [64]. The domains normally grow easily along the polar axis due to the kinks and ledges available in this direction. Furthermore, the growth velocity along the polar axis is normally significantly faster than the growth velocity along the lateral directions. For instance, in KTP the domain growth velocity is orders of magnitude larger along the polar axis than along the lateral directions [65].

In the lateral directions, there are two possible ways for the domain walls to move, either by direct movement of the domain wall, or by nucleation of new domains adjacent to an existing domain wall. The energy needed for a domain wall to move one lattice spacing sideways is on the same order of magnitude as the energy of the domain wall itself. Also, the energy gained by such movement of the domain wall is not very large. Therefore, this kind of wall sideways wall motion is highly unlikely [56]. It is more likely that domain walls move by nucleation at the crystal surface, adjacent to an already existing domain wall, causing the domain wall to move in a step-wise manner, as illustrated in Fig. 3.4 [66]. For this stepwise motion of the domain walls, the most energetically favorable shape of the nucleated domain is triangular, as seen in Fig. 3.4.

The dynamics of the polarization reversal is dependent on the magnitude of the electric field. The nucleation and the switching dynamics can be characterized by applying an electric field to the material and measuring the switching current due to polarization reversal in the material as a function of time [59]. Both the switching time and the domain velocity are important parameters to understand the polarization-switching characteristics of a material.
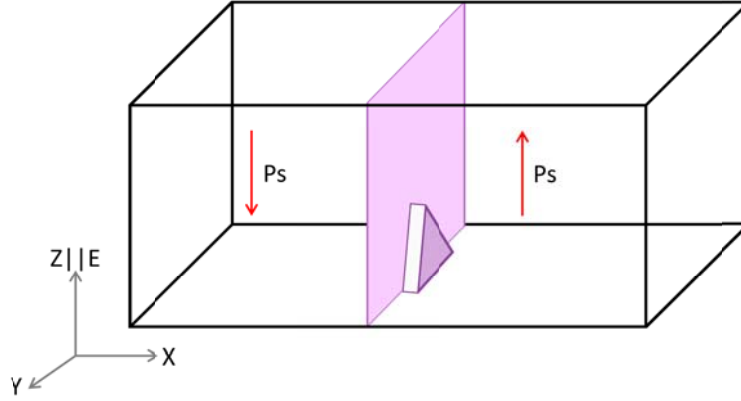
Fig. 3.4: Schematic drawing of a triangular domain nucleated adjacent to a domain wall.

The time needed to completely reverse the polarization under an applied electric field is the so-called *switching time*, t_s, which is commonly defined as the time from the beginning of the electric field pulse until the switching current has dropped to 5 % of its maximum value. For BaTiO$_3$, which is the most well-studied ferroelectric material, the switching time shows an exponential dependence if the magnitude of applied electric field is smaller than E_c,

$$t_s \sim e^{\frac{a}{E}}, \tag{3.8}$$

where a is the activation field [67]. As the magnitude of the electric field is increased above E_c, the switching time dependence on the electric field changes from an exponential to a power law [68],

$$t_s \sim E^{-n}. \tag{3.9}$$

Here, n is a material-dependent parameter.

The velocity of the domain-wall lateral motion, i.e., in the nonpolar directions, can also be correlated to the magnitude of the electric field. Miller and Savage [67] showed that the lateral domain wall velocity for BaTiO$_3$ depends inversely exponentially on the electric field when its magnitude is below E_c as:

$$v = v_{\infty} e^{-\frac{\delta}{E}}, \tag{3.10}$$

with v_{∞} and δ being parameters independent of the applied electric field. However, as the magnitude of the electric field increases above E_c, the dependence of v changes to:

$$v \sim E^n, \tag{3.11}$$

which is in agreement with Eq. (3.9). With the nucleation rate of the new domains being inversely proportional to the magnitude of the electric field, the polarization switching behavior below E_c can be understood as limited by the nucleation of new domains. However, at larger magnitudes of the applied electric field, above E_c, the polarization switching behavior is no longer limited by the nucleation rate but rather by material properties, given by the motion of the domain walls. In agreement to what has been found for BaTiO$_3$, Canalias *et al.* [65], Rosenmann

et al. [69] and Urenski *et al*. [70] reported similar polarization switching behaviors for KTP in two different regimes. At low fields, the polarization switching behavior is dominated by the nucleation rate of the new domains, while at high fields the polarization switching is governed by the domain-wall motion.

3.3 Role of defects

Defects in a crystalline lattice cause deformations of the crystal lattice and modify its local electric fields. The impact of the defect on the polarization switching characteristics of the material is governed by the type of the defect, the location of the defect in the lattice and the defect-host interaction. An acentric defect creates a dipole moment given by:

$$\overline{\Delta\mu} = \Delta\mu_d + \sum_i q_i \Delta x_i \,. \tag{3.12}$$

Here, $\Delta\mu_d$ is the change in dipole moment, Δx_i displacement of charge q_i in surrounding lattice due to the defect. Assuming the defect concentration, N, is small enough, the interaction between the different defects can be neglected. The change in macroscopic polarization is then given by:

$$\Delta P = N\overline{\Delta\mu} \,. \tag{3.13}$$

The contribution ΔP to the polarization of the material may or may not reverse when an electric field is applied to the material for polarization switching. If ΔP is reversed during polarization switching, the hysteresis loop will be altered due to the presence of the defects. In general, the presence of defects in a material tends to increase the magnitude of E_c. If all dipoles are ordered in the same direction, the hysteresis loop will appear biased. However, if the dipoles are completely random, the loop will show an increased E_c. If ΔP does not reverse under an applied electric field, the defects might act as initial nucleation sites, or be the cause of backswitching, i.e., domains returning to their previous state when the applied electric field is removed.

The defects might also cause domain wall pinning, i.e., that the domain wall motion is hindered by the coupling between the domain wall and the defects [64]. To overcome this, larger magnitude or longer pulse length of the applied electric field might be needed. When accurate control of the domain wall motion is needed, e.g. during fabrication of QPM devices, materials of high quality with low defect concentrations are desired.

4 Properties of KTP and RKTP

The nonlinear crystal used throughout this work is flux-grown bulk Rb-doped KTP (RKTP), which is an isomorph of KTP. In this chapter the material properties of KTP and RPKTP are presented.

KTP and its isomorphs do not exist in nature, but needs to be synthesized. The first synthesis of KTP was reported in 1890 [71], however it was not until the 1970s [72] the material attracted a considerable interest as a nonlinear media for frequency conversion due to its excellent properties, such as large optical nonlinearity, high damage threshold, excellent mechanical and thermal properties and high resistance to optical damage [73]. Today KTP and its isomorphs are well-established materials used in nonlinear optics, both for BPM, and for QPM using periodically poled crystals.

The crystalline structure of KTP was determined by Tordjman *et al.* [74] in 1974. The ferroelectric properties, enabling periodic poling, were first reported in 1980 [57]. Several techniques have been developed to obtain periodic poling of KTP, such as electric field poling at room temperature [75], poling by electron beam writing [76] , poling at low temperature [77] and electric field using chemical patterning [78].

4.1 Crystal structure

The KTP isomorphs are characterized by the unit formula $MTiOXO_4$, where M is K, Rb, Cs or Tl and X is P or As. KTP and its isomorphs are optically biaxial crystals. Their crystal structure is orthorhombic and belongs to the 2mm point group and the $Pna2_1$ space group [73]. The lattice constants of KTP are $a = 12.819$ Å, $b = 6.299$ Å, and $c = 10.583$ Å [79]. The crystallographic axes a,b,c correspond to the x,y,z optical axes, and the crystal exhibits spontaneous polarization along the z-axis. KTP undergoes a ferroelectric phase transition at 934 ˚C to the paraelectric state, where the crystal structure becomes centrosymmetric [57].

Each KTP unit cell contains four asymmetric units with two formula units per cell. The crystal structure is made up by TiO_6 octahedra forming helical chains along the [001] direction, linked together by PO_4 tetrahedra. There are eight oxygen atoms binding to both the Ti and P atoms, while two oxygen atoms bind only to the Ti atoms. Since the Ti atoms are slightly displaced in the TiO_6 octahedra, the length of the Ti-O bonds alternates between long and short in the helical chain. The TiO_6 octahedra and PO_4 tetrahedra form a crystal framework with cavities where the K^+ ions are accommodated, as illustrated in Fig. 4.1. The K^+ ions can occupy two non-equivalent sites in the crystal structure, the eight-fold coordinated K(1) site or the nine-fold coordinated K(2) site. As seen in Fig. 4.2 the cavities in which the K^+ ions are situated are slightly stretched along the polar direction and form open channels in this direction. The K^+ ions are loosely bound in the cavities, and can move via a hopping mechanism within the channels, being the cause of the ionic conductivity in the KTP isomorphs.
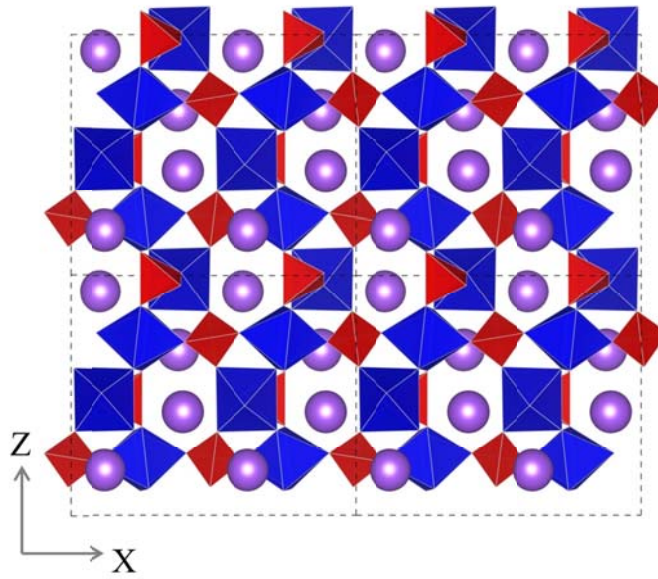
Fig. 4.1: The crystal structure of KTP viewed in the *y*-direction. The TiO$_6$-octahedra are shown in blue, the PO$_4$ tetrahedra in red and the K$^+$ ions in purple (adapted from [80]).

The origin of the optical nonlinearity in KTP is yet not fully established. Some studies suggest that the optical nonlinearity originates from the alternating short and long Ti-O bonds along the *z*-axis, which result in a net polarization in the *z*-direction [72,73]. In particular, the short Ti-O bond might be a major contributor due to its large polarizability [72]. In contrast, a more recent study by Xue *et al.* suggests that the nonlinearity originates from the KO$_x$ (x = 8,9) and the P(2)O$_4$ groups, whereas the TiO$_6$ and the P(1)O$_4$ groups are mainly responsible for the linear optical properties [81]. Therefore, to fully understand the origin of the optical nonlinearity in KTP, further studies are needed.
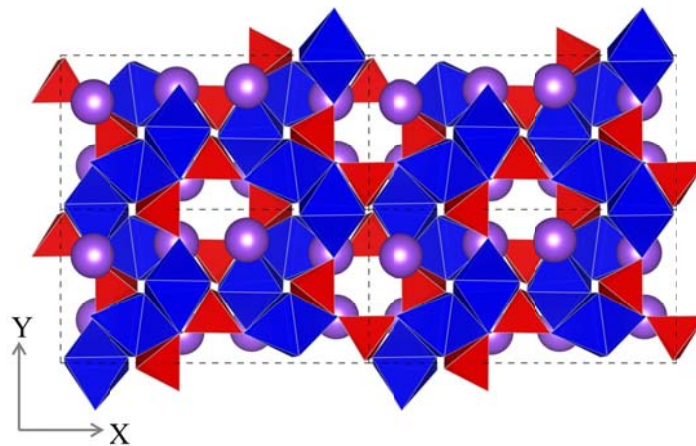

Fig. 4.2: The KTP crystal structure viewed in the *z*-direction. Here, the ionic transport channels can be observed (adapted from [80]).
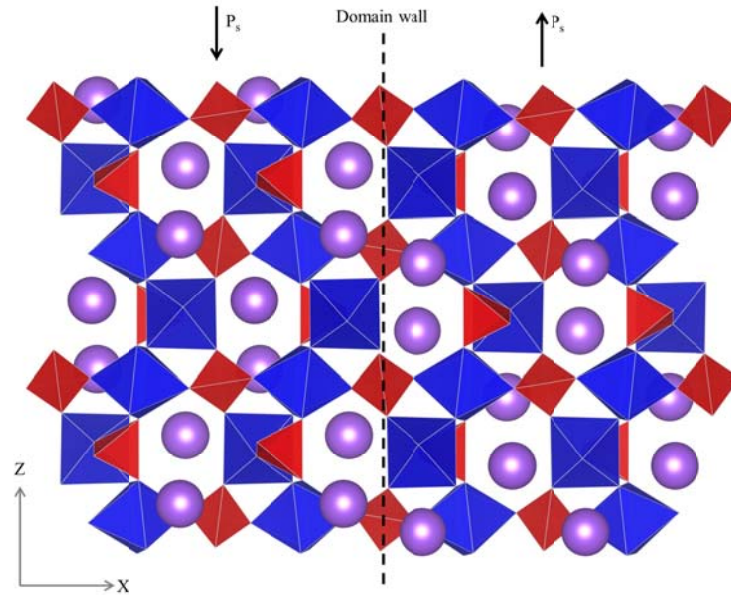
Fig. 4.3: Schematic view of two domains with opposite direction of the polarization, linked together by the P(1) atoms (adapted from [82]).

Stolzenberger *et al.* suggested that the polarization reversal occurs by shifting the K^+ ion to the alternative sites in the $-z$ direction [83]. This slightly relaxes the oxygen sublattice, and the eight-coordinated K^+ ion becomes nine-coordinated, and vice versa. Simultaneously, the TiO_6 and PO_4 framework adjusts to accommodate the shift of the alkali ion, and the short Ti-O bonds become long, and the long Ti-O bonds become short. Furthermore, it has been suggested that the P(1) atom is the pivotal point at the domain wall, linking the inverted domains together, as illustrated in Fig. 4.3 [82].

4.2 Crystal growth

The two main methods to grow KTP are by hydrothermal growth [84] and flux growth [85]. Hydrothermal growth is performed in an autoclave at high temperatures and at high pressure. The autoclave experiences a thermal gradient where the nutrient is dissolved in the heated part of the autoclave. By thermal-convection currents the nutrient is then transported to the cooler part of the autoclave, where the nutrient is crystallized into the desired crystal. For KTP, hydrothermal growth is normally done using a 2M K_2HPO_4 mineralizer at 400 ˚C at 1 kbar [84]. The main advantage with hydrothermal growth is the possibility to grow high quality crystals with low concentrations of vacancies and defects. However, the autoclave in which the growth occurs, need to be able to withstand high temperature, high pressure and corrosive solvents. Therefore, the need of complex equipment makes this an expensive alternative.

Flux growth, on the other hand, is performed at atmospheric pressure and at high temperature, although temperatures lower than the crystal melting point. The solvent containing the crystal nutrients is kept in a container with accurate temperature control. Crystal growth starts from a supersaturated flux in the coolest part of the container, either by spontaneous

nucleation, for small crystals, or by using a seed crystal, for growth of larger crystals. The growth then continues while the temperature is slowly decreased. If the growth is performed below T_c, it will result in a single-domain crystal, whereas growth performed above T_c will result in a multi-domain crystal [86]. In order to ensure crystals of high quality, good temperature stability is needed (better than 0.05 ˚C), as well as small temperature gradients to avoid thermal strain. In order to ensure sufficient flow of the flux to the growing crystal, the crystal is rotated in the flux. Any inhomogeneity of the nutrient flow is avoided by changing the direction of the rotation. Typically, flux growth of KTP crystals is carried out at 840- 928 ˚C from a flux containing various phosphates or tungstates, e.g. $K_6P_4O_{13}$ [85].

The typical growth morphology for KTP is shown in Fig. 4.4 [73]. KTP tends to grow on the (100), (201), (011) and (110) planes, where the (201) and (011) plane form sharp caps along the z-direction. The growth rate for the different planes depends of the flux components, flux saturation and the growth temperature. Other growth morphologies are, however, possible if the growth parameters are adjusted, which was exploited to grow periodically poled KTP crystals [38].
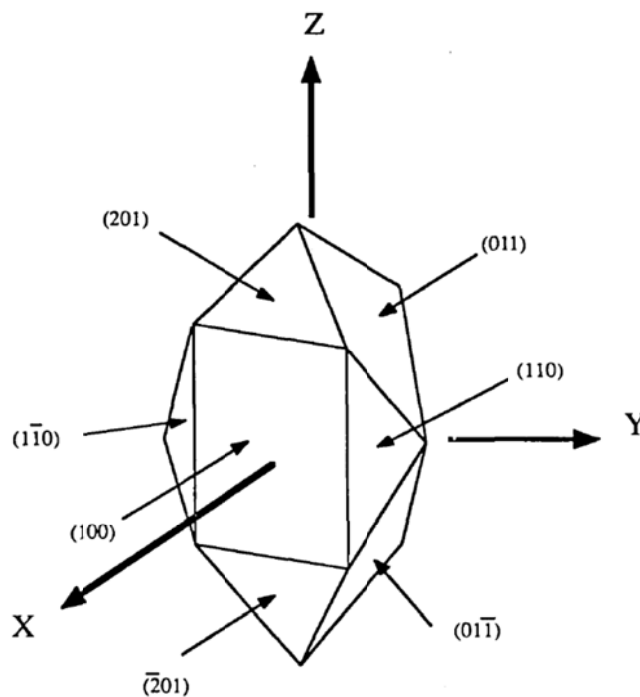

Fig. 4.4: The natural morphology of KTP isomorphs [73].

It should be noted that flux growth is simpler and much less expensive than hydrothermal growth. The disadvantages are however slow crystal growth, the different growth rates of the different planes and the larger concentration of vacancies and defects in the produced crystal.

4.3 RKTP

The RKTP used in this work is grown with 1.4 mol% Rb in the flux, resulting in a 0.3 % doping of the final crystal. During the growth process, the Rb^+ ions will occupy some of the K^+ sites in

the crystal structure. At low doping concentrations, the Rb^+ ions prefer to occupy the larger K(2) position in the crystal lattice [87].

The very light Rb-doping of RKTP grants very similar linear and nonlinear optical properties as KTP. Nevertheless, RKTP has proven to have decreased susceptibility to grey-tracking [88–90]. Moreover, the Rb-doping in RKTP significantly decreases the ionic conductivity compared to undoped KTP, which greatly affects the domain-wall movement during the periodic poling [19], which, in turn, enhances the quality of the fabricated QPM structures.

Polarization switching in RKTP was first demonstrated by Jiang *et al.* [91]. However, Wang *et al.* demonstrated the first periodically poled RKTP crystals [92]. In recent years, the material has attracted more and more interest for fabrication of fine pitch QPM gratings, particularly demonstrated in this work. The material shows improved homogeneity compared to undoped flux-grown KTP, making it possible to obtain homogenous periodically poled structures over larger areas [16].

4.4 Ionic conductivity

As mentioned above, the ionic conductivity in KTP is caused by a vacancy hopping mechanism of the K^+ ions in the crystalline lattice. The K^+ ions can move through the open channels formed by the oxygen atoms in the framework, as illustrated in Fig. 4.1 and Fig. 4.2. Potassium vacancies have been found to be the main contributor to the ionic conductivity in KTP isomorphs. The potassium vacancies originate from the growth process of the crystal. At the elevated temperatures where crystal growth occurs, oxygen atoms tend to escape out of the crystal lattice leaving a charge unbalance. This charge unbalance is compensated for by removal of K^+ ions leaving a crystal with oxygen and potassium vacancies.

The magnitude of the ionic conductivity therefore depends of the growth process, as well as on the isomorph composition [93]. Flux grown KTP typically has a conductivity of 10^{-5} S/m [15] while hydrothermal KTP has an ionic conductivity of 10^{-7} S/m [94], owing to the lower concentration of vacancies in the hydrothermally grown material.

The RKTP crystals used in this work has significantly lower conductivity than flux grown KTP, due to the Rb-doping of the material [15]. The Rb^+ ion is larger than the K^+ ion which tends to block the hopping channels along the polar axis. This corresponds to higher activation energy for the Rb^+ ion, which effectively reduces the conductivity.

The ionic conductivity of the as-purchased RKTP wafers is measured prior to poling. It is done by application of an electric field with a magnitude well-below the coercive field while the current is monitored. To avoid any risk for poling, the electric field is applied parallel to the non-switching direction. A typical wafer map is shown in Fig. 4.5 [15].
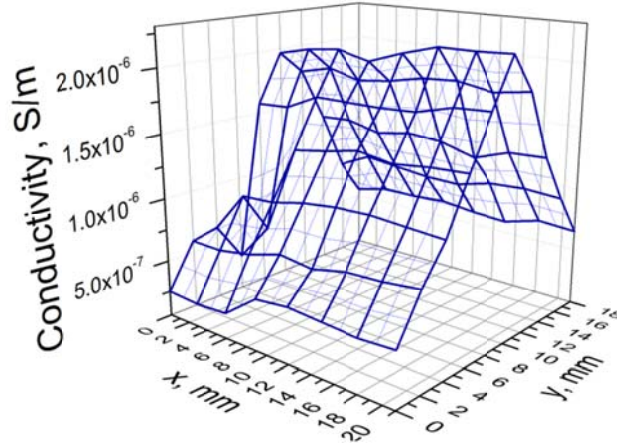
Fig. 4.5: Wafer map of the ionic conductivity in RKTP [15].

As evident in Fig. 4.5, the ionic conductivity varies significantly over the wafer. In a typical RKTP wafer the variation of the ionic conductivity is considerably smaller along the x-direction of the wafer than in the y-direction. Along the y-direction the conductivity presents a parabolic behavior and might vary with as much as one order of magnitude. This variation has been connected to temperature gradients over the crystal during the growth process, leading to varying stoichiometry over the wafer. Furthermore, each wafer may vary in conductivity.

4.5 Optical properties

The low Rb doping of the RKTP used in this work grants practically the same optical properties as those of undoped flux-grown KTP. Therefore, unless otherwise stated, the properties of KTP are referred to, which have been studied in detail, and are essentially the same as those of RKTP.

KTP is transparent for optical radiation of wavelengths approximately between 365 nm and 4.3 µm as can be seen in Fig. 4.6 [95]. There is a strong absorption at 2.8 µm due to OH⁻ impurities in the crystal, which are incorporated in the crystal during the growth process.

The nonlinear coefficients for KTP at 1064 nm given in pm/V are [96]:

$$d = \begin{pmatrix} 0 & 0 & 0 & 0 & 2.02 & 0 \\ 0 & 0 & 0 & 3.75 & 0 & 0 \\ 2.02 & 3.75 & 15.4 & 0 & 0 & 0 \end{pmatrix}. \tag{4.1}$$

In QPM devices, usually the large d_{33} coefficient is exploited.
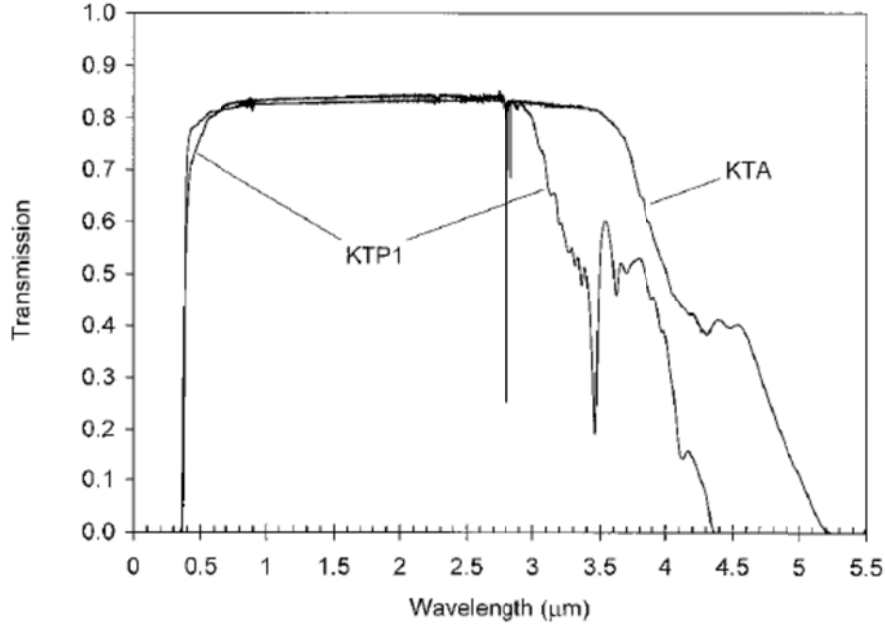
Fig. 4.6: The transmission spectrum of KTP and the isomorph KTA for z-polarized light [95].

In order to design a QPM device for a specific application, knowledge of the refractive index for all of the interacting waves is needed. The refractive index at a given wavelength can be derived from the Sellmeier equations. For KTP, the Sellmeier equation has the following form:

$$n_z^2 = A + \frac{B}{1 - C\lambda^{-2}} + \frac{D}{1 - E\lambda^{-2}} - F\lambda^2,$$ (4.2)

where A,B,C,D,E,F are material dependent coefficient and λ is the wavelength [97,98]. For wavelengths below 1 μm, the Sellmeier coefficients reported by Fan *et al.* [97] work best, while Fradkin *et al.* [98] have reported accurate coefficients for wavelengths above 1 μm, all shown in Table 4.1.

Wavelength range	Coefficient					
	A	B	C	D	E	F
λ < 1 μm [97]	2.25411	1.06543	0.05486	0	0	0.02140
λ > 1 μm [98]	2.12725	1.18431	0.0514852	0.6603	100.00507	0.00968956

Table 4.1: Sellmeier coefficients for KTP for wavelengths below and above 1 μm.

Moreover, the refractive index has a temperature dependence which needs to be accounted for. For wavelengths shorter than 1 μm, the temperature corrections to the Sellmeier equation was derived by Weichmann *et al.* [99] on the form:

$$\frac{dn_z}{dT} = \frac{a_3}{\lambda^3} + \frac{a_2}{\lambda^2} + \frac{a_1}{\lambda} + a_0,$$ (4.3)

with a_m, $m = 0,1,2,3$, being material coefficients. For wavelengths above 1 μm, the temperature corrections have been derived by Emanuelli and Arie [100] on the form:

$$\Delta n_z = n_1(T - 25°C) - n_2(T - 25°C)^2,$$ (4.4)

with

$$n_{1,2} = \sum_{m=0}^{3} \frac{a_m}{\lambda^m}.$$ (4.5)

The coefficients a_m are given in Table 4.2.

Wavelength range		Coefficient			
		a_0	a_1	a_2	a_3
$\lambda < 1$ μm [99]	10-5/°C	1.2415	-4.4414	5.9129	1.2102
$\lambda > 1$ μm [100]	n_1, 10^{-6}	9.9587	9.9228	-8.9603	0.6603
	n_2, 10^{-8}	-1.1882	10.459	-9.8136	3.1481

Table 4.2: Temperature correction coefficients for KTP for wavelengths below and above 1 μm.

The resistance to high optical intensities is important as it ultimately limits the nonlinear process. There are several forms of damage, and the most sever is catastrophic damage where the material breaks down irreversibly. The threshold for this type of optical damage in the crystal is determined by several factors such as wavelength, transient behavior of the pump laser (pulsed or continuous wave regime), pulse length, polarization of interacting waves as well as the individual crystal quality, etc. Most damage threshold studies are performed in the nanosecond regime. A recent study showed that the damage threshold for KTP and RKTP is approximately 10 GW/cm^2 for 1 μm and 2 μm radiation using 11 ns pulses at 100 Hz polarized along the z-axis [101]. This study further showed that the damage occurred mainly at the crystal surfaces, suggesting the surface quality was the main limiting factor, rather than the wavelength. Other studies showed slightly different results depending of measurement parameters [73,102–104]. Compared to other nonlinear crystals, e.g. LiNbO3 [105], the resistance to optical damage is significantly larger.

As the wavelength decrease towards the lower limit of the KTP transmission range, the KTP isomorphs become more and more absorbing, as seen in Fig. 4.7. The absorption at these wavelengths leads to thermal dephasing of the QPM device and, hence, to decreased conversion efficiency, long term stability and lower resistance to optical damage [90,106]. Moreover, at visible wavelengths KTP isomorphs suffer from so-called *grey-tracking*. Grey-tracking is formation of color centers in the crystal due to absorption of light in the blue and the green spectral range, leading to an increased absorption of infrared light. Recent studies have shown RKTP is significantly less prone to grey-tracking, which is attributed to the lower ionic conductivity compared to KTP [88,89]. This can be understood by considering the dynamics associated with the color center formation. It has been indicated by electron-paramagnetic-resonance (EPR) studies that the formation of the color centers can be associated with the emergence of Ti^{4+}/Ti^{3+} electron traps and O^{2-}/O^{-} hole traps on the oxygen ion adjacent to the Ti

ions [107,108]. These electron and hole traps are inherently unstable, and can be stabilized by the oxygen and the potassium vacancies in the crystal lattice originating from the growth process, as well as by polaron formation [89]. The potassium vacancies are, just like the K^+ ions, loosely bound in the conduction channels of the crystal lattice and can easily move to stabilize the electron traps. In RKTP, the conduction channels are blocked by the Rb^+ ions, resulting in a decreased mobility of the potassium vacancies. Therefore, less electron traps will be stabilized by the potassium vacancies, effectively resulting in a larger resistance towards grey-tracking. Furthermore, it has been shown that the grey-tracking can be further mitigated by an increase of the temperature at which the QPM device is operated [89,109,110].
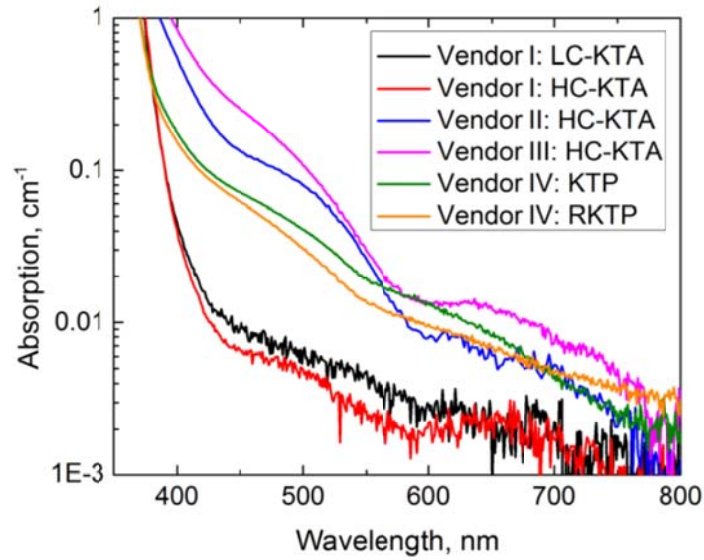

Fig. 4.7: Absorption as a function of wavelength in various KTP isomorphs for *z*-polarized light [15].

4.6 Polarization switching dynamics of RKTP

To successfully fabricate domain-inverted structures in RKTP with high pattern-fidelity and high reproducibility, good knowledge is needed of the parameters that play an important role in polarization switching, such as the ionic conductivity, the coercive field, the switching time, the domain nucleation and the domain wall velocities. For the KTP isomorphs, these properties were extensively studied by Zukauskas [15] and Canalias [11] and will be summarized here.

As mentioned in Chapter 3, the coercive field is defined as the electric field needed to reverse the spontaneous polarization. The coercive field can be measured by monitoring the current through the material during the application of a linearly ramped electric field antiparallel to the spontaneous polarization. In RKTP, and other KTP isomorphs, the measured current in a crystal under an applied electric field is the combination of the switching current and the ionic current. The total current density in a KTP crystal is described by [65]:

$$J = \frac{9}{8}\varepsilon\varepsilon_0\mu\frac{V^2}{L^3} + 2P_s\frac{1}{A}\frac{\partial A_i}{\partial t}. \tag{4.6}$$

35

Here, ε is the relative permittivity of the material, μ the ion mobility, V the applied voltage, L the crystal thickness, P_s the spontaneous polarization and A is the area over which the voltage is applied. The ionic current depends quadratically on a linearly ramped applied electric field, while the switching current should appear as a sharp peak at the coercive field [111], provided that the ramp rate of the external electric field is properly chosen, so that the switching current is not masked by the dominating ionic contribution. Fig. 4.8 shows a typical coercive field measurement of a RKTP crystal.
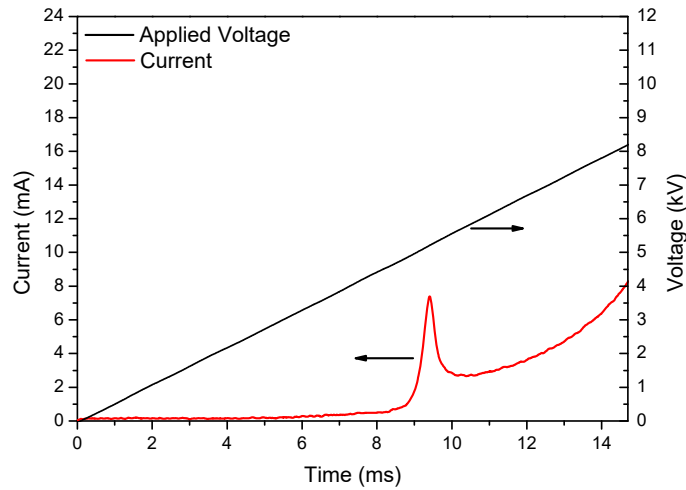

Fig. 4.8: The measured current under an applied linearly ramped electric field for a 1 mm thick RKTP sample.

As can be seen, the RKTP crystal measured in Fig. 4.8 has a coercive field of 5.02 kV/mm. Here, the ramp rate of the applied electric field was 550 V/ms. It is worth mentioning that the magnitude of the coercive field is strongly dependent on the ramp rate of the external electric field. For a linearly ramped pulse, the ramp rate is determined by the peak magnitude of the electric field and the pulse length. When the peak magnitude of the applied electric field pulse is kept constant, the coercive field varies with the pulse length as [112]:

$$E_c = \frac{\alpha}{\ln(\tau) - \ln(\gamma)},$$

(4.7)

where α is the activation field, τ is the pulse length and γ is a parameter independent on the applied electric field. In RKTP, Zukauskas reported a variation of the coercive field of 3.8-6.5 kV/mm for ramp rates ranging from 2.56 kV/ms to 284 V/ms [15].

Moreover, to accurately fabricate domain inverted structures, it is crucial to understand the dynamics of the domain formation. For this purpose, it is meaningful to study the switching time, the domain wall velocities and the domain-nucleation rate of RKTP. The polarization switching time gives an estimate of the time scale at which new domains form. The switching time is dependent on the magnitude of applied electric field, as discussed in chapter 3.

The domain wall velocities can be measured using the so-called Miller-Savage method [67]. Electric field pulses are applied to the sample and the resulting domain structure is observed by

selective etching in between each pulse. The domain velocity in each direction is defined as the average domain width divided by the length of the electric field pulse. For KTP, the domain wall velocity is at least two orders of magnitude faster in the polar direction compared to the nonpolar directions. In the nonpolar x- and y-directions, the domain wall velocity is approximately 30 times faster along the y-direction than along the x-direction [65], resulting in a large anisotropy in the domain-wall velocity.

For KTP, it has been reported that the domain-nucleation rate is significantly larger on the z^- surface compared to that of the z^+ surface [65]. A plausible explanation is that the preferred nucleation on the z^- surface is caused by the movement of the K^+ ions in the crystal structure. When an external electric field is applied to the crystal, the K^+ ions will move towards the z^- surface, where an accumulation of K^+ ions is created. The accumulation of K^+ ions might increase the nucleation probability at this surface. Moreover, the rate at which new domains nucleate is highly influenced by the interface between the material and the electrode. It has been experimentally observed that it is possible to further enhance the domain nucleation rate by deposition of an aluminum film on the z^--surface [11,15].
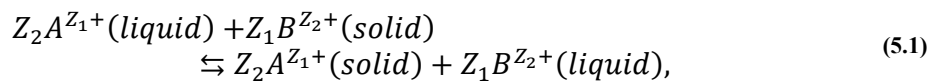
5 Ion exchange

The ion exchange technology in KTP was developed in 1980's by Bierlein *et al*. [113] to enable the fabrication of waveguides. The K$^+$ ions in the KTP structure are exchanged for Rb$^+$, Cs$^+$, or Tl$^+$ ions, resulting in an increase of the refractive index, which can be used for waveguiding of light in the high refractive-index region. Moreover, ion exchange processes were also used for controlled domain reversal before the electric field poling technique was developed to fabricate QPM devices [2]. Furthermore, the ion exchange technology can be used to engineer the coercive field and the ionic conductivity of the KTP crystals [78,113]. Risk *et al*. utilized the coercive field difference between ion-exchanged and non-exchanged regions to fabricate periodically poled, segmented waveguides for QPM applications [78]. However, this approach was never tested for fabrication of bulk ferroelectric domain gratings.

In this work, the ion exchange process in RKTP has been exploited for engineering of bulk devices: both in terms of coercive field engineering for subsequent periodic poling and bulk refractive index engineering in the crystal. In this chapter, the ion exchange process in KTP is reviewed and the impact of the various ion exchange parameters is studied. The resulting optical properties of the fabricated devices will be discussed in Chapter 7.

5.1 Introduction to ion exchange

The process of ion exchange in a solid material, where ions in the material are exchanged for dopant ions, can be used to alter the chemical composition of the material and its properties. In practice, the process of ion exchange is seemingly simple, but good knowledge and understanding of diffusion in solid materials, and the interplay between diffusion, ionic conductivity, ionic species and temperature is needed to fully comprehend the process and engineer the material properties. Typically, the ion exchange is performed by submersion of a solid material (e.g. a crystal) into a liquid containing the dopant ion at elevated temperatures, thereby allowing host ions to be replaced by dopant ions from the liquid through a diffusion process. The ion exchange is driven by the chemical potential of the system, i.e., the concentration gradient of the host and dopant ions, and the gradient of the electric potential in the material [114]. The gradient of the electric potential is built up by the ion exchange process itself, even if no external applied electric field is present. The electric potential is a result from formation of vacancies as host ions diffuse out of the material, leaving a charge unbalance. The charge unbalance, in turn, attracts ions from the liquid to diffuse in to the material, to neutralize it. Meanwhile, the system will aim to reach a chemical equilibrium state, where the concentration of host and dopant ions on the surface of the solid material is in chemical equilibrium with the concentrations of the ionic species in the liquid. The process of ion exchange can therefore be described by the chemical reaction [115]:

$$Z_2 A^{Z_1+}(liquid) + Z_1 B^{Z_2+}(solid)$$
$$\leftrightarrows Z_2 A^{Z_1+}(solid) + Z_1 B^{Z_2+}(liquid),$$

<div align="right">(5.1)</div>

where Z_1 and Z_2 are the charge of the dopant ion A and host ion B, respectively. To maintain charge equality in the process, the total charge of the in-diffused dopant ions must equal the total charge of the out-diffused host ions.

Diffusion of ions in a solid material is motivated by thermal vibrations of the ions, causing random jumping of ions to the nearest empty space in the matrix, e.g., a vacancy in a crystal lattice. The process of random jumping to adjacent sites makes diffusion a highly statistical process, although temperature dependent. When the temperature of the system is increased, the amplitude of the thermal vibrations increases, thereby making the random jumps between adjacent sites more probable. From a macroscopic point of view, diffusion of an ionic or atomic species at any given interface in the material can be described by *Fick's first law*:

$$J_i = -D_{ij} \frac{dc}{dX_j}, \qquad (5.2)$$

where J_i is the atomic flux, X_j the gradient direction, c the concentration of the diffusing species and D_{ij} the diffusion coefficient for the given atom in the diffusion direction. J and X are both vectors while D is a second order tensor given by the structure of the material. The minus sign in Eq. (5.2) indicates a fundamental property of diffusion. Ions will diffuse so that the chemical potential, i.e. the concentration difference, of the system is minimized by moving from highly concentrated regions to regions with lower concentration [114].

The diffusion coefficient, D, can be described by the Arrhenius relationship:

$$D = D_0 \exp\left(-\frac{Q}{RT}\right), \qquad (5.3)$$

where Q is the activation energy, R the universal gas constant, D_0 a temperature independent factor and T the absolute temperature. Eq (5.3) emphasizes the relation between diffusion and temperature, while Q can be correlated to the energy required to initiate diffusion of a given ionic species, which is dependent on the structure of the material as well as the charge, weight and radius of the ion of interest.

The temporal behavior of diffusion can, in turn, be described by *Fick's second law*:

$$\frac{\partial c}{\partial t} = D_{ij} \frac{\partial^2 c}{\partial X_j^2}. \qquad (5.4)$$

From *Fick's second law*, it can be understood that the rate of the diffusion is correlated to the concentration difference in the gradient direction. The diffusion process slows down as the concentration difference, i.e. chemical potential of the system, decreases. Once the system is in chemical equilibrium, the diffusion will seize.

Moreover, the diffusion of a given ion is closely related to the ionic conductivity, σ, of a material through the Nernst-Einstein equation:

$$\sigma = \frac{Dnq^2}{kT}, \qquad (5.5)$$

with q being the charge per ion, k the Boltzmann's constant, T the absolute temperature, n the number of charge carriers per unit volume and D the diffusion coefficient. Although the ionic conductivity is commonly used to describe the response to an applied electric field, it is, indeed, a diffusive process where ions in the material move to minimize the electric potential of the system. Moreover, the ionic conductivity of a material can be easily measured by application of an external electric field, and thereby makes it possible obtain an estimate of the diffusion dynamics of the material.

In an ion exchange process, not only one ionic species should be considered, but both the host and the dopant ionic species. In a binary system, the diffusion of the two species through a given plane can be described by the Nernst-Planck equation:

$$
\begin{aligned}
J_i^A &= -\widehat{D}_A \left(\frac{dc_A}{dX_j} - \frac{c_A F Z_1}{RT} \frac{dV}{dX_j} \right), \\
J_i^b &= -\widehat{D}_B \left(\frac{dc_B}{dX_j} - \frac{c_B F Z_2}{RT} \frac{dV}{dX_j} \right).
\end{aligned}
\tag{5.6}
$$

Here, dV/dX_j is the potential gradient, F the Faraday constant, and $\widehat{D}_i$ diffusion coefficient of the binary process that is connected to the self-diffusion coefficient D_i through:

$$
\begin{aligned}
\widehat{D}_A &= D_A \left(1 - \frac{c_A}{c_B} \left(\frac{d \ln \gamma_A}{d \ln c_B} \right) \right), \\
\widehat{D}_B &= D_b \left(1 - \frac{c_B}{c_A} \left(\frac{d \ln \gamma_B}{d \ln c_A} \right) \right),
\end{aligned}
\tag{5.7}
$$

where γ_i is the activity coefficient of the ions A and B , respectively. From here, it is obvious that the diffusion of the dopant ions into the solid and the out-diffusion of host ions are interconnected.

5.2 Ion exchange in KTP and RKTP

In the KTP isomorphs, ion exchange has traditionally been performed by submerging the crystal into a nitrate melt, typically heated to 330-450 °C, containing dopant ions Rb^+, Cs^+ or Tl^+ ions, thereby substituting the K^+ ions in the crystal structure [113]. The crystal is heated up alongside the melt to avoid breaking from thermal stress [116], and then submerged in the nitrate melt for the ion exchange. The ion exchange process is stopped by removing the crystal from the melt and subsequent cooling to room temperature. The range of temperatures at which ion exchange is performed is limited by the melting point of the nitrate melt, for cooler temperatures, and etching of the sample, at higher temperature [113]. Although ion exchange has been performed with a variety of monovalent and divalent dopant ions [113,116–118] in KTP, most of the thorough studies have been done on exchanges involving Rb^+ ions. In waveguides, a refractive index increase sufficient to guide one or two modes is desired. The larger polarizability and radius of the Cs^+ and Tl^+ ion result in large increases of the refractive index, and thereby multimode

waveguides, even for shallow ion-exchange depths [113]. Additionally, Cs^+ and Tl^+ are radioactive and very poisonous ions, thereby making handling of the nitrate salts highly hazardous.

The ion exchange in this work is mainly performed with Rb^+ ions, thereby creating a mixed $Rb_aK_{a-1}TiOPO_4$ structure, where a is the dopant concentration ranging from 0 to 1. Therefore, from here on, the dopant cation can be assumed to be Rb^+ unless otherwise mentioned. Ba^{2+} and K^+ ions were also added to the nitrate melt to enable engineering of the process, as will be discussed later on in this chapter. The work was performed in RKTP, with ca 0.3 at% Rb^+ present in the material from the growth process. However, the low doping of RKTP, compared to KTP, makes it reasonable to assume that the ion exchange dynamics are very similar.

5.2.1 Ion exchange using a monovalent RbNO$_3$ melt

As discussed in Chapter 4, the K^+ ions are loosely bound in the KTP crystal structure, and can move by a vacancy hoping mechanism in the channel network, hence being the cause of the ionic conductivity. At elevated temperatures, the amplitude of the thermal vibrations of the K^+ ions increases, causing an increased diffusion of the ions. When submerged in a nitrate melt with dopants, the K^+ ions close to the surface diffuse out of the crystal into the melt and leave behind a negatively charged potassium vacancy. These negatively charged vacancies, in turn, electrostatically attract the dopant ions in the melt, whereby they diffuse into the crystal to compensate the charge unbalance. Moreover, already preexisting vacancies, obtained during the crystal growth, can also attract dopant ions from the melt [119]. In general, the ion exchange process in KTP can be described by [119]:

$$M_L^{n+} + nK_S^+ \leftrightarrows M_S^{n+} + (n-1)V_K + nK_L^+. \tag{5.8}$$
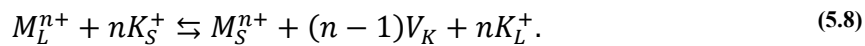
Here, M is the dopant ion with charge n, V_K a potassium vacancy and S and L are the solid and liquid phase, respectively. When ion exchange is performed using a monovalent ion, the concentration of dopant ions diffusing into the KTP crystal is equivalent to the out-diffusion of K^+ ions. However, if the dopant ion is divalent, formation of additional vacancies is required to maintain charge neutrality.

As the Rb^+ ions diffuses in to the crystal and replaces K^+ ions, the preferred occupancy of the Rb^+ ion is in the larger nine-fold coordinated K(2) site [120]. Therefore, the majority of the Rb^+ ions diffusing into the crystal will first be situated in the K(2) site and only occupy the K(1) site at large Rb^+ concentrations in the sample. It has also been suggested by Thomas *et al.* that the Rb^+ ions in ion exchanged KTP also partially occupy the nine-fold coordinated hole site, h(1), as a residual charge density could be found in close proximity to this hole site [87].

The Rb^+ ion (and other monovalent dopant ions) has a larger ionic radius than the K^+ ion. In order to accommodate the larger Rb^+ ion in the exchange, the lattice needs to adjust. It has been found that during ion exchange, the crystal lattice expands along the *x*- and *y*-direction taking intermediate values between those of KTP and RTP, listed in Table 5.1 [79,120], depending on the dopant ion concentration. In contrast, the lattice contracts in the *z*-direction during ion exchange, creating a distorted unit cell [119].

	$a(x)$ (Å)	$b(y)$ (Å)	$c(z)$ (Å)
KTP [79]	12.819	6.339	10.584
RTP [120]	12.974	6.494	10.564

Table 5.1: Lattice constants of the isomorphs KTP and RTP.

The ion exchange process is initially rapid, and then slows down the further the process proceeds, as K^+ ions are released into the nitrate melt and dopant ions incorporated in the crystal, as indicated by Fick's second law (Eq. (5.4)). Moreover, the rate of exchange is orders of magnitude faster in the KTP isomorphs along the polar z-direction, compared to the non-polar x- and y-directions. This is an effect of the ionic mobility being order of magnitudes larger along the polar direction than in the non-polar directions, which is connected to the KTP crystals structure (see Section 4.4). Furthermore, the ion exchange rate in KTP, in a monovalent melt, is larger in the z^- direction than the z^+ direction. The polar nature of KTP results in a preferential movement of the K^+ ion towards the high temperature, paraelectric, position [116]. Therefore, the rate of exchange is higher in the z^- direction, and the resulting ion exchanged layer is slightly deeper as compared to exchange structures on the z^+ surface.

In the purely monovalent melt, the diffusion rate of the dopant ion in the KTP crystal, along the channels in the crystal structure, is strongly dependent on the sample conductivity, as it is largely dependent on the preexisting K^+ vacancy concentration [113,121]. The Rb^+ ion has a larger ionic radius and higher activation energy than the K^+ ion, and it will therefore be much less mobile in the crystal structure. The in-diffused Rb^+ ions ends up blocking the conduction channels in the crystalline structure close to the crystal surface and only diffuse a few μm into the crystal, preventing K^+ ions situated deeper in the crystal to diffuse out. The concentration of Rb^+ ions is at maximum at the surface, at the interface with the nitrate melt, and then decreases with depth in the bulk of the crystal. Typically, the thickness of the ion-exchanged layer varies between 1-10 μm.

If not interrupted, the ion exchange process continues until a chemical equilibrium state has been established between the crystal and the melt. The concentration of Rb^+ ions incorporated into the ion exchanged crystal is directly correlated to the ratio between the concentration of Rb^+ ions and K^+ ions in the melt [119]. In a pure $RbNO_3$ melt the largest possible dopant concentration in the crystal at equilibrium is 65 % [119]. If the concentration of $RbNO_3$ in the melt in decreased and KNO_3 added to the melt the surface concentration of the dopant ion will be decreased, as demonstrated by Roelofs *et al.* [119]. In order to obtain concentrations of Rb^+ ions larger than 65 % the KTP crystal needs to be ion exchanged in several subsequent $RbNO_3$ melts [119].

The concentration of the various atoms and ions in the crystal structure can be measured using a variety of techniques, such as energy dispersive X-ray spectroscopy, in a scanning electrode microscope (SEM-EDX) or by the electron microprobe technique (EMP). Bierlein *et al.* reported that the distribution of the in-diffused Rb^+ ions follows a complementary error function when scanned from the surface into the bulk of the crystal along the polar direction in the sample [113]

$$C(z) = C_s \cdot erfc\left(\frac{z}{d}\right),$$

(5.9)

where C is the Rb^+ concentration, C_s the Rb^+ surface concentration, and d the depth of the ion exchanged region.

The refractive index increase normally scales with polarizability of the dopant ion, i.e., with the charge difference between the K^+ ion and the dopant cation. The refractive index profile along the polar axis of such devices is normally derived by measurement of the guided modes in the structure, followed by calculations using the *inverse WKB* method [122]. In agreement with the dopant ion concentration, the refractive index profile induced by the ion exchange follows a complementary error function written on the form [113,116]:

$$n(z) = n_s \cdot erfc\left(\frac{z}{d}\right) + n_{KTP}.$$

(5.10)

Here, n_s is the magnitude of the surface refractive index and d the depth of the ion exchanged structure. It can be observed that the refractive index increase is proportional to the concentration of dopant ions given by Eq. (5.9).

In similarity to what is reported for ion exchange in KTP, the isomorph RKTP also presents a refractive index profile of a complementary effort function when subject to a shallow ion exchange process, as shown in Fig. 5.1. For the waveguide structures, the refractive index profile can be correlated, one to one, to the distribution of the Rb^+ ions in the sample [113].
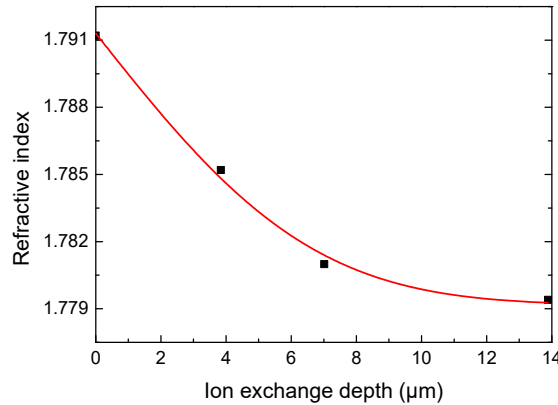

Fig. 5.1: Refractive index profile of a planar waveguide in a RKTP crystal, exchanged in a pure RbNO$_3$ melt at 345 ˚C for 90 min.

5.2.2 Addition of Ba^{2+} to the $RbNO_3$ melt

To obtain ion exchange depths larger than tens of micrometers and to gain more accurate control of the diffusion rate, as well as thickness of the ion exchanged structure, a divalent ion can be added to the nitrate melt. Most commonly, addition of Ba^{2+} ions are used for this purpose. The Ba^{2+} ion is slightly smaller than the K^+ ion and can therefore move more easily within the crystal lattice. The divalent Ba^{2+} ions and potassium vacancies have an electrostatic attraction which creates a bond between the cation and the vacancy. This bond does, however, occupy two

43

potassium sites, resulting in nearby K^+ ions being repelled from the Ba^{2+} ion [123]. Addition of Ba^{2+} creates additional potassium vacancies to maintain the charge neutrality of the system, as seen in Eq.(5.8). These additional potassium vacancies are available for the monovalent dopant ions at the crystal surface. Therefore, the monovalent ion exchange rate is significantly increased and the impact of the sample conductivity is greatly reduced, resulting in an increased reproducibility of the process. Moreover, addition of divalent ions to the nitrate melt prevents the surface to saturate with monovalent dopant ions and keeps the conduction channels open, thereby allowing for the dopant ions to diffuse deeper into the crystal structure.

However, it has been observed that addition of Ba^{2+} into the nitrate melt sometimes causes reversal of the spontaneous polarization during the ion exchange process [2]. The domain reversal from the ion exchange process has only been observed close to the z^--surface, even if the ion-exchanged structure is considerably deeper, as shown in Fig. 5.2. This suggests the domain reversal occurs where the Rb^+ ion concentration is the largest, and therefore creates the largest strain in the crystal lattice. The combined large Rb^+ concentration and the relief of strain induced by the Ba^{2+} ion could, indeed, be a plausible explanation for this phenomenon. It has been suggested that the domain reversal is correlated to the charge difference between the Ba^{2+} ion and the K^+ ions since the Ba^{2+} ion is more electronegative than the K^+ ion and will pull the oxygen framework around itself as it exchanges for a K^+ ion in the crystal framework [119,123]. This, in turn, causes local expansions of the framework in the surrounding regions, which helps in accommodating the larger Rb^+ ion. At the same time, these local contractions are also considered to be mechanism for relieving strain in the ion-exchanged region. It is believed that this release of strain in the crystal structure is related to the domain reversal. Moreover, as previously mentioned, the Rb^+ ions prefer the nine-fold K(2) site in the crystal lattice. Only at high concentrations, the Rb^+ ions start occupying the K(1) site. It is also possible for the Rb^+ ions to fill the hole sites, h(1) and h(2), which both are larger than corresponding K-sites. These sites are readily available for the Rb^+ ions, especially when ion exchange is performed from the z^- surface. When the Rb^+ ions are situated in the hole sites, the crystal structure resembles that of the inverted P_s. Nevertheless, the complete dynamics of the domain reversal during ion exchange remains to be fully understood and requires further research. It is also unclear whether domain reversal occurs during the ion exchange process, or when the crystal is removed from the melt and cooled down.
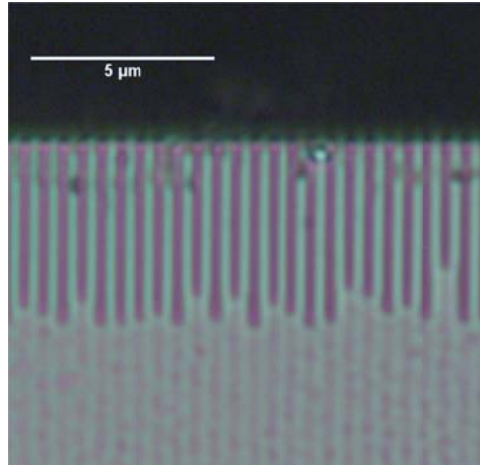
Fig. 5.2: Optical micrograph of a periodic ion exchanged structure, Λ = 700 nm, viewed at 45˚ angle from the z^- surface, exchanged in a 73 mol% RbNO$_3$ / 7 mol% Ba(NO$_3$)$_2$ / 20 mol% KNO$_3$ melt at 350 ˚C for 4 h. The enhanced contrast pattern showed the domain inverted regions from the ion exchange with average thickness of 4 μm. The ion exchanged structure is in total 22 μm thick.

5.3 Engineering of material properties by ion exchange

The ion exchange process can be used to engineer the refractive index, the ionic conductivity and the coercive field in KTP and its isomorphs [78,119]. As discussed earlier in this chapter, the final ion exchanged structure is dependent on a number of parameters, such as the melt composition, the temperature, the exchange duration, and the sample conductivity. By alteration of these parameters, the ion-exchanged structure can be tailored for a large variety of applications. In this work, the aim was to periodically alter the chemical composition of the RKTP crystals to create a coercive field grating to be used for subsequent periodic poling, using planar electrodes. For this purpose, a sufficiently large increase of the coercive field is needed to result in selective domain reversal during poling. Additionally, the resulting ionic conductivity should be equal to or smaller than the conductivity of the virgin crystal, to ensure that the poling current is supplied to the low coercive field regions, where domain reversal is wanted.

Ultimately, the composition of the nitrate melt used in the ion exchange process determines the resulting material properties. The Rb^+/K^+ ratio in the nitrate melt determines the concentration of Rb^+ ions which will be incorporated in the crystal, while the Ba^{2+} adds vacancies to the crystal structure [119]. The Rb^+ ion is, as previously mentioned, larger than the K^+ ion, and has larger activation energy in the KTP crystal structure. This results in a decrease of the ionic conductivity when the Rb^+ ions is incorporated in the crystal lattice, since the Rb^+ ions creates a blockage of the conduction channels. Moreover, the incorporation of Rb^+ ions in the crystal increases the coercive field compared to undoped KTP crystals [15,78]. Meanwhile, the additional potassium vacancies, attributed to the Ba^{2+} ions, results in an increase of the ionic conductivity.

The impact of the melt was investigated by performing planar ion exchange in RKTP crystals on the z^- surface. In KTP isomorphs, the z^- surface is advantageous for patterning due to the enhanced the domain nucleation to that of the z^+ face [65]. To prevent ion exchange on the z^+

surface, a stop layer was fabricated. The conduction channels in the KTP crystal structure can be blocked, and hence ion exchanged prevented, either by a metal mask or by plasma etching of the surface [113,124]. In this work mainly oxygen plasma etching has been used [PAPER I], which has previously not been reported. During the plasma etching, the crystal surface is bombarded by oxygen ions. It can be suggested that the plasma etching destroys the surface and subsurface crystal structure, and therefore blocks out- and in-diffusion of ions. This effect has also been reported using argon plasma etching [124]. However, the reason why ion plasma etching blocks the conduction channels remains unclear and further investigation is needed.

The ion exchange process in RKTP was studied using 3 different nitrate melts with constant Ba^{2+} concentration and varying Rb^+/K^+ ratio: the "Rb-rich" composition (73 mol% $RbNO_3$/ 7 mol% $Ba(NO_3)_2$/ 20 mol% KNO_3), the "half-Rb-K" composition (47 mol% $RbNO_3$/7 mol% $Ba(NO_3)_2$/46 mol% KNO_3) and the "Rb-poor" composition (20 mol% $RbNO_3$/7 mol% $Ba(NO_3)_2$/73 mol% KNO_3) listed in Table 5.2. The RKTP crystals were ion exchanged for 4 h at 375 ˚C in one of three different melts. With the Ba^{2+} ion concentration being constant it can be assumed the amount of additional vacancies is the same for all three melts. The Rb^+ ion surface concentration was estimated to 47 %, 13 % and 0.3 %, respectively, for the different compositions.

Recipe	Ion-exchange melt composition (molar %)	Ionic conductivity @ 8 kV/mm (S/m)	Coercive field (kV/mm)	Estimated Rb surface concentration (%)
Virgin	-	$1.15 \cdot 10^{-5}$	5.02	-
Rb-poor	20 % $RbNO_3$ / 73 % KNO_3/ 7 % $Ba(NO_3)_2$	$2.83 \cdot 10^{-5}$	-	3.5
Half-Rb-K	47 % $RbNO_3$ / 46 % KNO_3/ 7 % $Ba(NO_3)_2$	$2.13 \cdot 10^{-5}$	6.08	13
Rb-rich	73 % $RbNO_3$ / 20 % KNO_3/ 7 % $Ba(NO_3)_2$	$5.88 \cdot 10^{-6}$	6.72	47

Table 5.2: Melt compositions used for ion-exchange, σ_{ion}, E_c and estimated surface concentration for each melt composition when ion-exchange was performed at 375 ˚C for 4 h [paper I].

The resulting coercive field and ionic conductivity was measured for each melt composition by monitoring the current as an electric field with 550 V/ms linear ramp-rate was applied to the crystal to obtain polarization reversal. Fig. 5.3 shows the current response of three RKTP ion exchanged crystals, as well as that of a virgin crystal, and the linearly ramped electric field. The ionic current in all RKTP crystals responds quadratically to the applied electric field, in agreement with the Mott-Gurney law [111]. The coercive field was measured at the peak of the switching field (see Section 4.6). The ionic conductivity was measured at 8 kV/mm applied electric field.
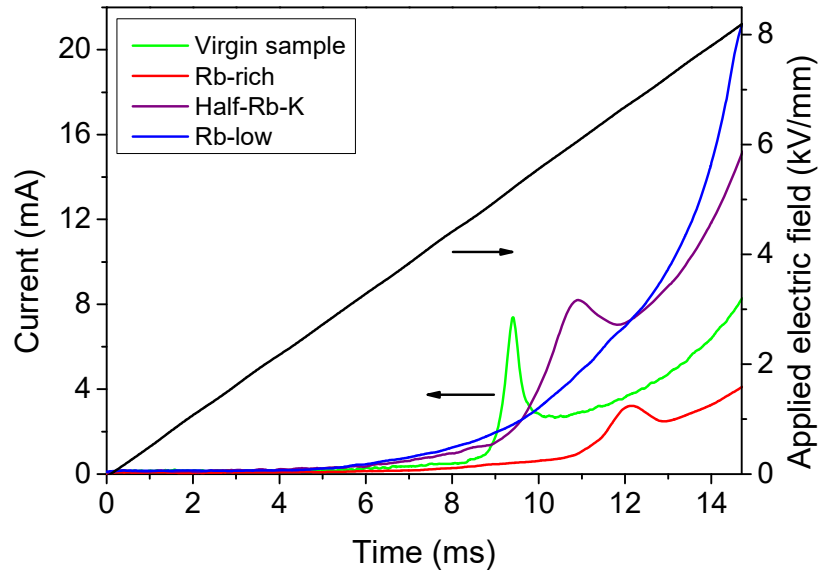
Fig. 5.3: Applied electric field (black, right axis) and corresponding current curves for a virgin (green) crystal, and for samples exchanged with the Rb-rich (red), half-Rb-K (purple) and the Rb-poor (blue) melts, respectively [paper I].

The largest increase of the coercive field is obtained for the Rb-rich composition, with $\Delta E_c = 1.7$ kV/mm compared to the virgin sample. The ionic conductivity of this sample was decreased by 50 %. The half-Rb-K melt composition resulted in an increase of the coercive field by $\Delta E_c = 1.06$ kV/mm and an increase of the ionic conductivity by 85 %. The Rb-poor melt composition had so large increase of the ionic conductivity, that it was not possible to reverse the polarization in this sample. Several different pulse shapes, ramp rates and magnitudes of the electric field was applied to the crystal, but no polarization reversal could be observed for the crystal before reaching material breakdown. All data is summarized in Table 5.2. It can be observed that the Ba incorporation increases the ionic conductivity while the Rb decreases it, as expected. Similar results have been observed in KTP by Karlsson *et al.*, Risk *et al.* and Roelofs *et al.* [75,78,119].

With the largest difference in the coercive field, and simultaneous decrease of the ionic conductivity, obtained for the Rb-rich melt, the impact of the ion exchange duration was studied for this melt. RKTP crystals were exchanged for varying durations between 4 h and 24 h, and the ionic conductivity and the coercive field were subsequently measured, as shown in Fig. 5.4. The coercive field increases 60 % ($\Delta E_c \sim 3$ kV/mm) for ion exchange durations longer than 8 h. The ionic conductivity simultaneously decreases by ~80 %. The magnitude of both the coercive field and the ionic conductivity saturates after ca 8 h, which is in agreement with results reported for KTP by Roelofs *et al.* [119].
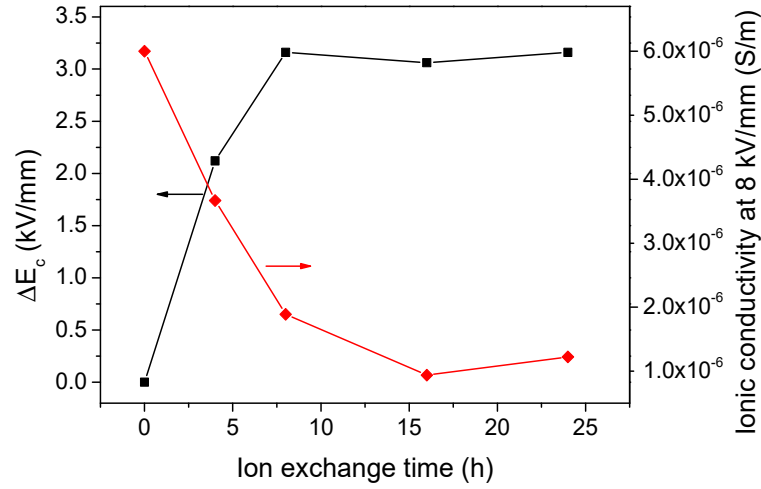
Fig. 5.4: Changes in E_c and σ_{ion} with exchange time relative to virgin samples for the "Rb-rich" recipe [paper I].

The observed saturation indicates that the full area of the sample is saturated with the maximum dopant concentration. Once there is a critical amount of Rb^+ ions in each of the conduction channels, the coercive field will reach its maximum magnitude and the ionic conductivity its minimum magnitude. Longer ion exchange durations will, indeed, result in thicker structures, but the magnitude of the electric response does not increase further.

The concentration gradient of Rb^+ and K^+ along the polar axis was measured on the *y*-surface of the sample ion exchanged for 4 h using SEM-EDX. In Fig. 5.5 it can be observed that the Rb^+ concentration is maximal at the z^- surface of the RKTP crystal and decreases further in to the bulk. The maximum Rb^+ concentration at the surface was measured to 43 %, in good agreement with the estimate of 47 %. The Rb^+ distribution could be fitted to a complementary error function, *erfc*(z/d), with a diffusion depth, d = 22 μm. Although the depth of the ion exchange region is significantly deeper than what has been previously reported for KTP, the concentration of the Rb^+ ions follow a complementary error function, in agreement previous reports of thinner ion exchanged structures in KTP. Moreover, it should be noted that in general the Ba^{2+} ions do not appear during SEM-EDX measurements as the Ba^{2+} ion typically are too light to be detected with this technique.
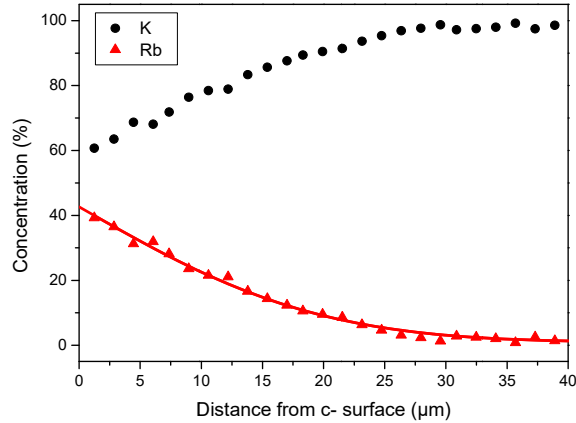
Fig. 5.5: Rb- and K-concentration measured from the ion-exchanged surface for a RKTP sample exchanged in a Rb-rich melt for 4 h at 375 ˚C. The Rb profile (solid curve) is fitted to an *erfc(z/d)* with *d* = 22 μm. The accuracy in concentration of the measurement is better than 2 % for both species [paper I].

To fabricate the coercive field grating, it is essential to enable selection of the regions of the polar surface where ion exchange is wanted. The significant difference in ion exchange rate along the crystalline axes in RKTP makes it possible to accurately control the regions where ion exchange is desired, without any broadening in the *x*- and *y*-direction [113]. Therefore, the regions where ion exchange is wanted can be selected by fabrication of a stop layer on the polar surfaces with high accuracy.

Moreover, the ion-exchanged structures can be visualized under illumination in a standard optical microscope, as shown in Fig. 5.6. The light from the microscope illumination is guided toward the higher refractive index of the ion exchange region, resulting in a contrast difference. As seen in Fig. 5.6 (a), the ion exchanged structure visible both viewed from the z^--surface (top view) as well as from the *y*-surface (side view). It is worth observing that the ion exchanged structure appears significantly deeper in the microscope compared to the measured cation distribution. This is most probably due to stresses induced in the crystal during the ion exchange process.
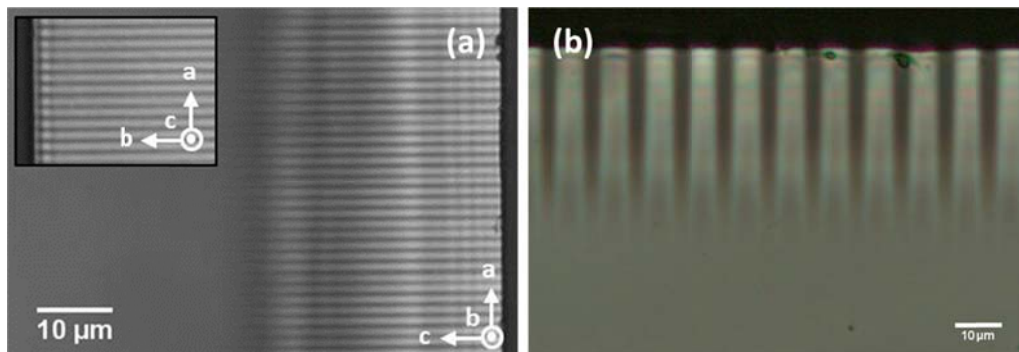

Fig. 5.6: (a) Optical micrograph of a periodic ion-exchange grating, Λ = 3.16 μm, as seen through the *y*-face and z^--face (inset) of the crystal. Both photos have the same scale. [Paper I] (b) Optical micrograph seen through the *y*-surface of a periodic ion exchange structure, Λ = 9.22 μm, in RKTP. The edges of the ion exchanged structures appear deeper than the middle regions. Both gratings were fabricated by ion exchange in a Rb-rich melt for 4 h at 375 ˚C.

49

Additionally, patterning of the surface to be ion exchanged creates a discontinuity between the ion-exchanged regions and the masked regions. This discontinuity gives rise to enhanced electric field at the ion exchanged/masked region. This enhanced electric field might increase the rate of exchange in this region, and thereby further increase the exchange depth. Moreover, this discontinuity also forces the crystal structure in the interface to be somewhat distorted, as the ion exchanged region adjusts to accommodate the larger cation while masked regions remain unchanged. Under illumination in an optical microscope this effect can be observed, as seen in Fig. 5.6 (b). However, it remains an open question whether it is correlated to larger dopant ion concentrations or increased stress in the interface between ions exchanged regions and unchanged regions.

6 Periodic Poling of RKTP

As mentioned earlier, a wide range of techniques have been developed for implementation of QPM structures for KTP family crystals, Today, the most commonly used technology is room temperature electric field poling [75–78].

To ensure efficient operation of the QPM device, the fabricated QPM grating needs to be uniform over the crystal aperture, and be of considerable length with minimal variations in the grating duty-cycle. Fabrication of such gratings is, however, not straight forward, since the final domain structure is dependent on a variety of interrelated parameters, such as crystal homogeneity and ionic conductivity, the properties of the applied electric field, ambient temperature etc.

In this chapter, periodic electric field poling of RKTP is presented. A novel periodic poling technique based on coercive field engineering is introduced to facilitate fabrication of fine-pitch QPM gratings. This technique is exploited for fabrication of high-quality bulk sub-μm QPM gratings.

6.1 Electric field poling with metal electrodes

6.1.1 Sample preparation

The RKTP crystals used in this work are commercial flux grown z-cut wafers. The as-purchased wafers are approximately $35 \times 35 \times 1$ mm^3 in size along the x-, y- and z-directions. First, the ionic conductivity is mapped for each individual wafer. Typically, the ionic conductivity in the wafers varies along the y-direction of the wafer, while remaining essentially constant along the x-direction (see section 4.4). Therefore, to increase the poling yield, each wafer is cut into pieces which are typically $11 \times 6 \times 1$ mm^3 in size in the x-, y- and z-directions, to obtain crystals with as homogenous ionic conductivity as possible, and each crystal is then treated separately. Moreover, the anisotropy of the domain wall velocity in KTP isomorphs is exploited by aligning the grating vector in the x-direction and the electrode stripes along the y-direction. After cutting, the x-surfaces of each crystal are polished to an optical finish to allow for laser excitation.

Electrodes for the poling are fabricated on the z^--surface using lithographic techniques. For KTP isomorphs, it is preferred to fabricate the poling electrodes on the z^--surface, to exploit the higher domain nucleation rate compared to the z^+-surface. Standard contact lithography is used to create a periodic photoresist pattern of desired periodicity above 2 μm. For periodicities below 2 μm a different lithographic system is used, which will be discussed later on in this chapter. Electrodes are then fabricated on the crystal surface through evaporation of an Al film over the patterned surface to ensure electric contact in the openings of the photo resist. The photo resist layer is kept to act as an insulator where domain reversal is not desired during the poling process. The sample preparation is illustrated in Fig. 6.1.
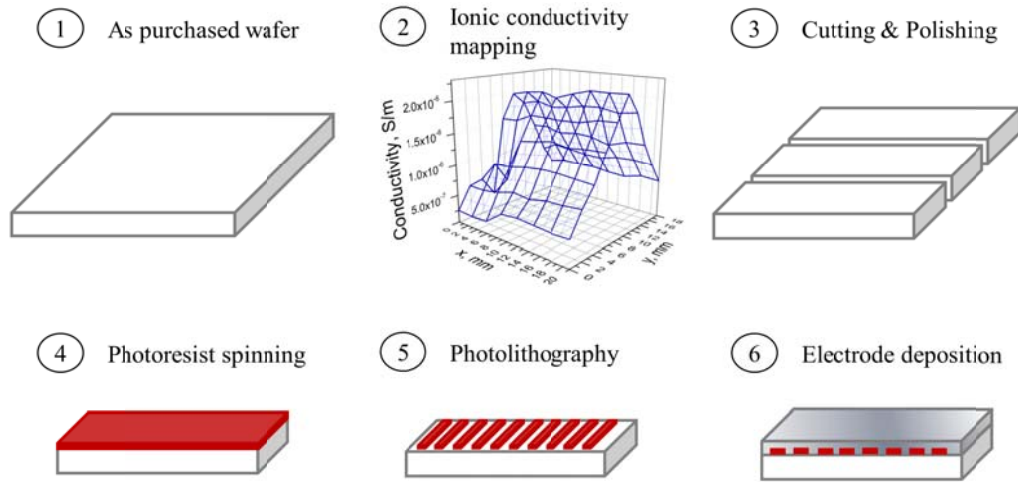
Fig. 6.1: Schematic of the sample preparation steps before the periodic poling.

6.1.2 Monitoring techniques

During poling, it is of utmost importance to monitor the evolution of the domain reversal in the sample, in order to know when the poling process is complete. Proper monitoring of the domain reversal evolution also provides information of key parameters for the domain reversal. In this work, the poling process was monitored using two optical techniques. In ferroelectric materials with low conductivity, the switching current is monitored as the external electric field is applied. The applied electric field is stopped when sufficient charge is supplied to pole the desired area A, such that $Q = 2P_sA$. Unfortunately, this is not a feasible method for RKTP due to the fact that it is very difficult to discern the ionic contribution from the switching current. Nevertheless, it is still useful to monitor the current through the sample to gain information about the ionic conductivity of each crystal. The circuit used for electrical measurements and poling is illustrated Fig. 6.2. The applied electric pulse is generated using a waveform generator, and it is amplified with a high voltage amplifier (HV) to the desired field strength. The current flowing through the sample during poling is monitored using a serial resistance $R_1 = 10$ kΩ. The voltage over the sample is measured over the resistance $R_3 = 100$ kΩ, which acts as a voltage divider together with $R_2 = 100$ MΩ.
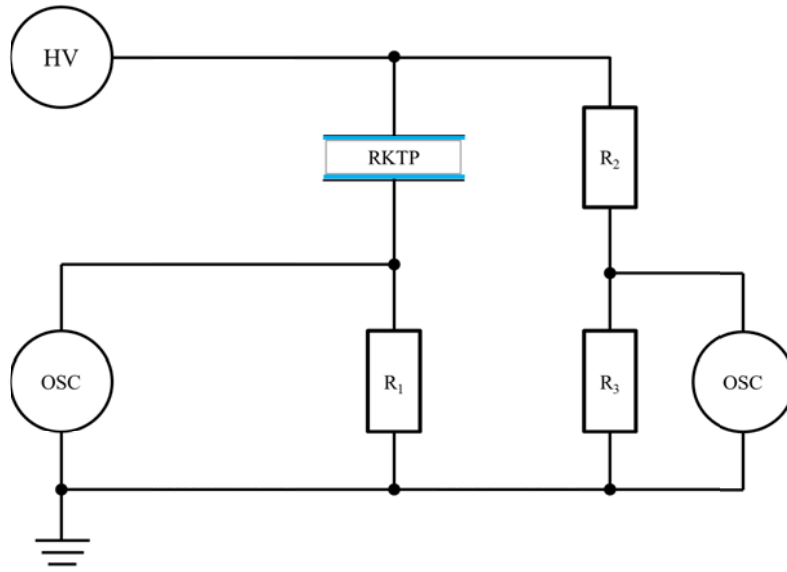
Fig. 6.2: Schematic of the poling circuit used in this work.

In order to monitor the progress of the periodic poling, two optical methods were used. The first method exploits the electro-optic effect [125]. Here, the light from a HeNe laser is launched along the x-axis in the RKTP crystal. The laser light is polarized 45˚ to the z-axis. A second polarizer is positioned after the RKTP crystal, with its orientation orthogonal to the laser light. The light transmitted through the second polarizer is recorded by a photodetector connected to an oscilloscope. When an electric field is applied over the crystal the refractive index changes due to the electro-optic effect. The change of the refractive index induces a phase shift of the laser light, thereby changing the polarization of the light. This phase shift is time dependent when the applied electric field is non constant, or when the field is constant and reversal of the spontaneous polarization occurs. As the polarization of the light is altered, the amount of light transmitted through the second polarizer is altered, resulting in an intensity modulation of the light measured by the photodetector. Fig. 6.3 shows a schematic of the setup. Using this method, it is possible to determine whether poling occurs in the crystal when the electric field pulse is applied. However, the electro-optic effect gives no indication of the quality of the final ferroelectric domain structure.
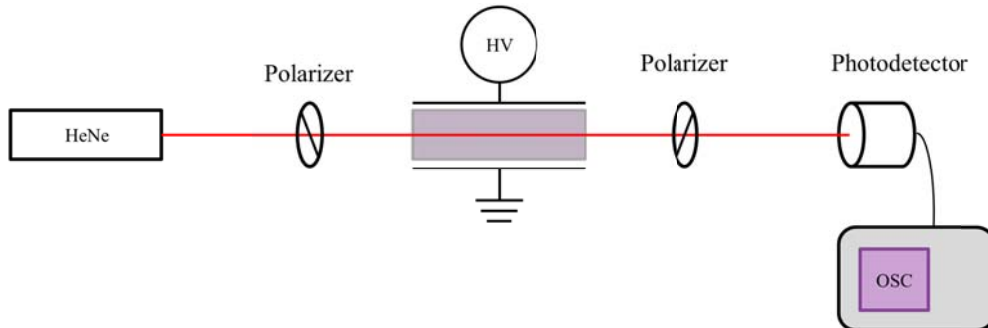

Fig. 6.3: Setup of the electro-optic poling monitoring.

The second method used to monitor the quality of the domain grating is in-situ SHG [92]. Measuring the power of the generated second harmonic gives an accurate indication of the quality of the domain grating. Here, a tunable, continuous wave Ti:Sapphire laser is loosely focused into the RKTP crystal along the *x*-axis. The SHG output power is separated from the fundamental power using a color filter and then measured using a power meter. Fig. 6.4 shows an illustration of the setup. The range of the available Ti:Sapphire laser is 750-950 nm. This corresponds to 1st order QPM for periods ranging from 3 µm to 6 µm. For longer periods, 3rd or higher-order QPM can be used. This method allows for assessment of the grating quality and the full aperture of the poled crystal can be scanned and evaluated. However, this technique only allows for monitoring of the domain grating quality after the grating has already formed.
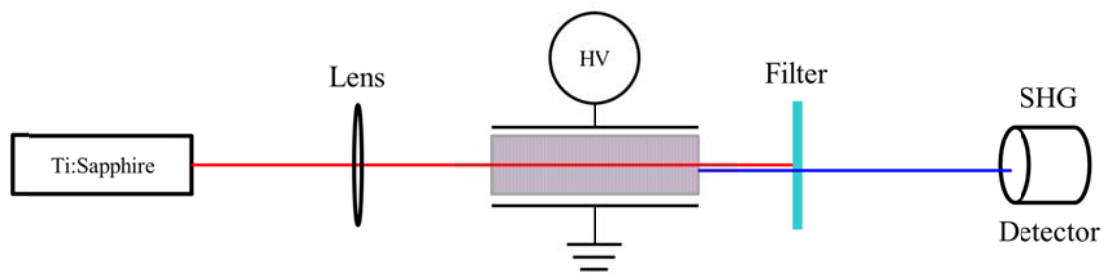
Fig. 6.4: Poling monitoring by SHG.

6.1.3 The poling process

Once patterned the crystal is connected to the poling circuit using liquid KCl electrodes at both polar surfaces. An electric field pulse is applied to invert the spontaneous polarization in the area where the Al electrodes are in contact with the crystal. The formation of the ferroelectric domain grating is illustrated in Fig. 6.5. Typically, nucleation of new domains starts at the edges of the metal electrodes where the magnitude of the electric field is the largest, the so-called *fringing fields*. The nucleated domains propagate to the other polar surface while new domains continue to nucleate under the metal electrodes, in a competing process. Finally the domains merge, and, ideally, a ferroelectric domain grating with a 50 % duty-cycle is formed.
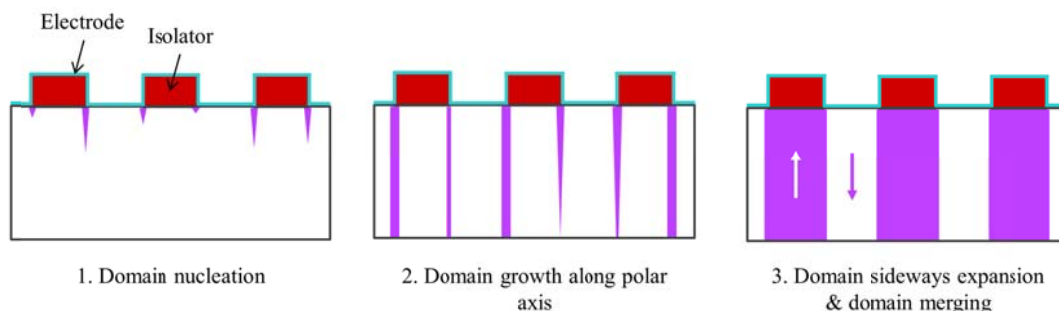

Fig. 6.5: Schematic of the periodic poling process.

The shape and the magnitude of the applied electric field pulse are crucial for the formation of the ferroelectric domain grating. The pulse shape is normally designed to obtain the largest possible domain-velocity anisotropy. For RKTP, Lindgren *et al.* recently reported that a triangular pulse shape is the most favorable for fabrication of homogenous domain

structures [126]. A symmetric triangular electric field pulse provides a well-controlled poling process, as the majority of the domains nucleate close to the peak of the electric field pulse. The nucleated domain tips then propagates to the z^+ surface, resulting in a homogenous grating.

The formation of domain gratings in KTP isomorphs occurs in the millisecond time scale. Therefore, it is reasonable that the applied electric field has a pulse length in the same order of magnitude, typically 2.5-5 ms. Similar results were observed by Canalias *et al.* in KTP [127].

If the domains growth and merging of domains occur under the isolating photoresist grating, so that a too large area is being poled, the sample is considered *overpoled*. This typically occurs when the magnitude of the applied electric field is too large or the pulse length is too long. In contrast, if the domains do not fully merge under the electrodes and the domain grating is not fully formed, the sample is deemed as *underpoled*. In this case, the magnitude of the applied electric field is too low or the pulse length too short.

Formation of inverted domains outside of the metal electrodes, under the isolating photoresist, is the most common problem during the poling process. The electric field is enhanced at the edges of each electrode, as shown in Fig. 6.6. The fringing fields at the edge of the electrode also has a tangential component, E_x, in contrast to straight under the electrode where only the normal component, E_z, of the electric field is present [19]. The normal component of the electric field, E_z, is responsible for the switching and nucleation of new domains. In the polarization switching process, the depolarization energy is minimized by compensation charges supplied by an external voltage source. Due to the transverse field component, E_x, at the electrode edges some of the supplied charges can move under the insulated area, and cause nucleation of new domains in this region, thereby broadening the domains. The width of the domain broadening, Δa, under the isolated area is correlated to the switching time τ_{sw} and the crystal conductivity, σ, as [19].

$$\Delta a \propto \tau_{sw}\sigma.$$

(6.1)

In KTP isomorphs, the domain broadening can be mitigated by a decreased ionic conductivity [75] and/or by using short pulses during the poling process [18].

Moreover, the domain broadening can to some extent be compensated for by decreasing the width of the electrodes, i.e., by patterning with a duty-cycle D < 50 %. For considerably large periods, e.g. $\Lambda \approx 30$ µm, it is not necessary to decrease the duty-cycle of the electrodes, as the impact of the fringing fields is considerably small. However, as the period decreases, the impact of the fringing fields on the final domain structure is increased. Therefore, the duty-cycle of the electrode needs to be decreased to prevent an erroneous duty-cycle of the final ferroelectric domain grating; e.g. for a grating period $\Lambda = 2$ µm the duty-cycle of the electrode was D = 15 % to enable formation of a domain grating with a final duty-cycle of approximately 50 %.
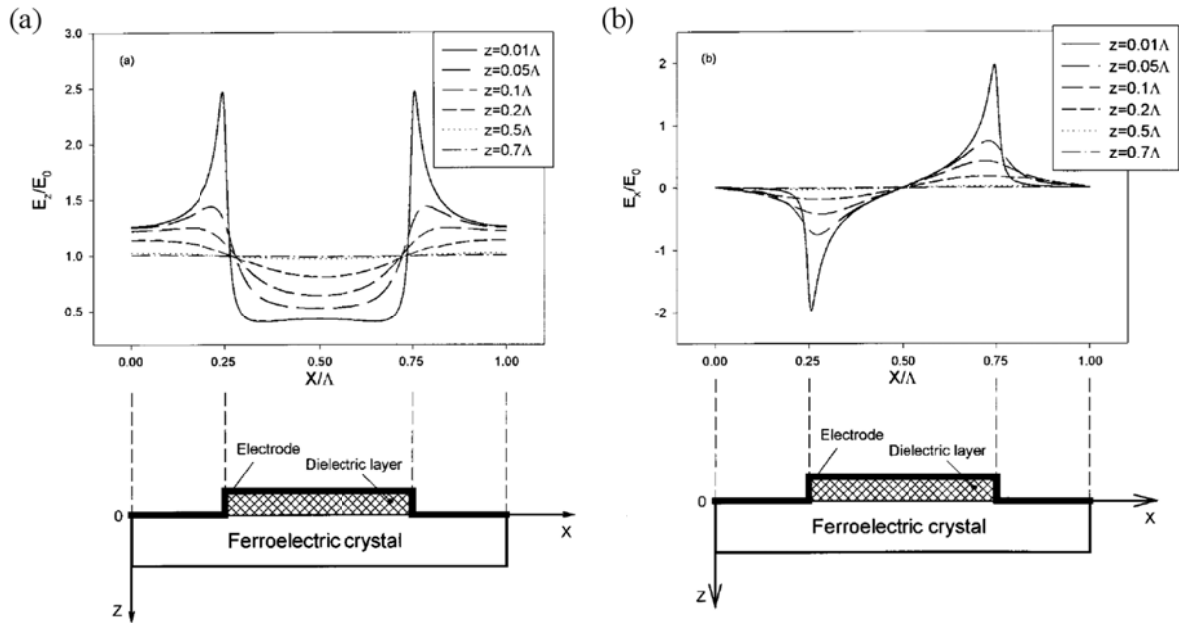
Fig. 6.6: The distribution of the (a) normal and (b) tangential components of the electric field due to the edge of the electrode (from [19]).

6.1.4 Sample evaluation

In this work, three methods were used to evaluate the final domain structures, selective etching, SHG and atomic force microscopy.

After poling, the resulting domain structure can be visualized by etching the sample in a KOH:KNO$_3$ solution [128]. This makes it possible to visually inspect the quality of the grating on the polar faces and study any irregularities or defects. Typically, the etching is done by submerging the crystal in a KOH:KNO$_3$ solution at 100 °C for approximately 30 s. The OH$^-$ groups attacks the z^- surfaces of the crystal, while the etch rate of the z^+ surfaces is significantly lower [15]. This creates a relief on the crystal surface, visible under microscope illumination, which provides instant information on the quality of the final domain structure. Fig. 6.7 shows an etched domain-grating structure of a periodically poled RKTP crystal. The period of the crystal is $\Lambda = 6.01$ μm, designed for SHG of light with a wavelength of $\lambda = 943$ nm. The duty-cycle on the patterned surface is similar to that of the metal electrodes. The domains on the unpatterned surface are slightly broadened compared to the electrode width.
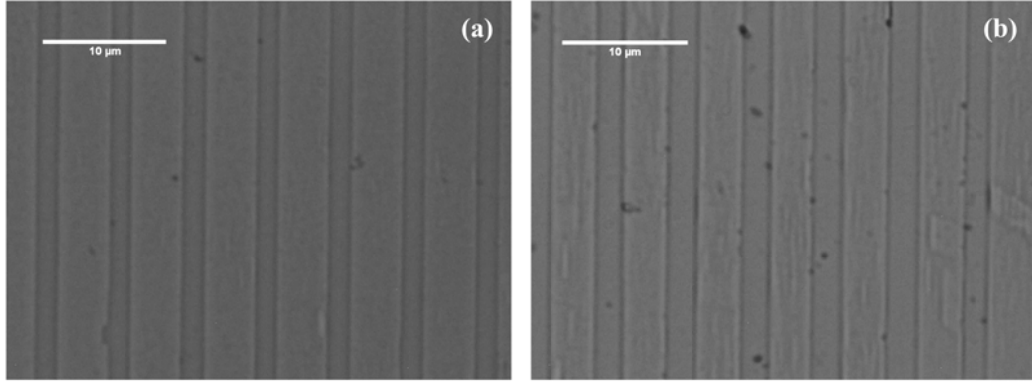
**Fig. 6.7: Optical micrograph of the periodic domain structure with period Λ = 6.01 µm on the (a)
former z^- surface and (b) former z^+ surface.**

For domain periods not resolvable in an optical microscope, an atomic force microscope (AFM) can be used to visualize the topography of the etched domain structure, as shown in Fig. 6.8 (a). The AFM can also be used to visualize ferroelectric domains without etching the sample through the so-called piezo-force microscopy (PFM). In PFM, a small-magnitude sinusoidal voltage is applied to the cantilever while the tip is scanned in contact with the crystal surface. Due to the piezoelectric effect, the sample surface will oscillate. These oscillations can be filtered out from the topographic signal with a lock-in amplifier, and can be used to visualize the ferroelectric domain structure on the polar as well as on the non-polar surfaces, as shown in Fig. 6.8 (b).
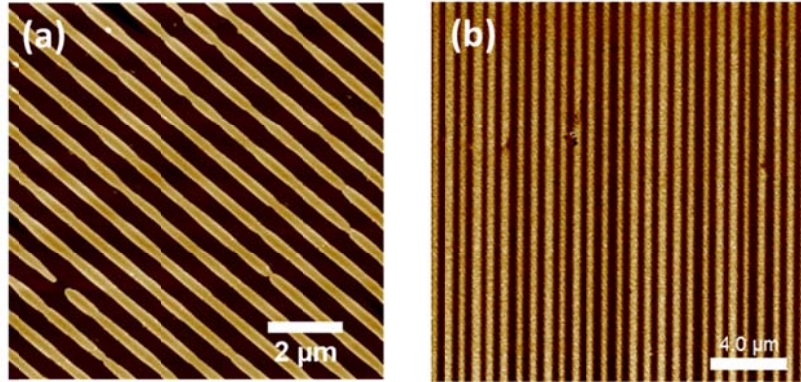

**Fig. 6.8: (a) The topography imaged by AFM of a selectively etched sub-µm periodically poled
crystal on the patterned surface [paper II] and (c) PFM of the domain structure in the crystal bulk
imaged on the nonpolar y-surface [paper III], with inverted domains in yellow.**

The performance of fabricated QPM devices with Λ > 2 µm can be evaluated optically for single pass, continuous wave SHG using a Ti:Sapphire, pump laser, as shown in Fig. 6.4. The measured SHG efficiency the QPM device is normalized with respect to the pump power and grating length to

$$\eta = \frac{P_{SHG}m^2}{P_F^2 L}.$$

(6.2)

57

Here, η is the normalized conversion efficiency, P_{SHG} the generated SHG power, P_F the pump power of the fundamental beam, L the grating length and m the QPM order. High quality domain gratings in KTP isomorphs typically have a normalized conversion efficiency of $\eta = 1 - 1.8 \ \%\text{W}^{-1}\text{cm}^{-1}$. The normalized conversion efficiency provides a quantitative measure of the quality of fabricated device while being a completely non-destructive method to evaluate the QPM device.

6.2 Electric field poling with a coercive field grating

Electric field poling with metal electrodes is the standard technique to fabricate ferroelectric domain gratings in KTP isomorphs. However, domain broadening associated with the fringing fields from the metal electrodes severely limits the lateral control of the domain growth as the grating period is decreased. An alternative route to gain accurate control of the domain formation is to periodically engineer the coercive field of the crystal, to select the regions where domain reversal is wanted. This allows for poling using planar electrodes, thereby mitigating the domain broadening associated with the fringing fields.

A coercive field grating can be fabricated in the RKTP crystal bulk using an ion exchange process to periodically alter the chemical composition of the crystal, and thereby alter its coercive field. In this work, additional Rb-doping was used to engineer the coercive field of the RKTP crystals for subsequent periodic poling. A similar technique was suggested by Risk *et al.* for fabrication of QPM structures in KTP waveguides [78], but the technology has never been used in RKTP nor been studied for implementation of bulk gratings.

6.2.1 Fabrication of the coercive field grating

The first steps of sample preparation are equal to those described in Section 6.1.1, as illustrated in Fig. 6.9. After depositing a photoresist grating, the photoresist pattern, as well as the z^+ surface, is exposed to oxygen plasma etching. The oxygen plasma creates a stop layer that prevents in- and out-diffusion of ions in the selected regions, thereby making it possible to select the areas for ion exchange. The photoresist is subsequently cleaned off the z^- surface. Thereafter ion exchange is performed in a Rb-rich melt for the desired period of time to create the coercive field grating. Care should be taken when choosing the melt composition and the duration of the process. The concentration of Rb^+ ions exchanging the K^+ ions in the crystal structure increases as the ion exchange process proceeds, thereby inducing stress in the crystal. The increased stress causes the crystal to be more fragile or even break during the ion exchange process. Moreover, as showed in 5.3, the effect of the ion exchange process on the coercive field and the ion conductivity saturates after approximately 8 h. Therefore, ion exchange processes with durations longer than 8 h are not necessary. The melt composition should be chosen so that the ion exchanged regions experience a simultaneous increase of the coercive field and decrease of the ionic conductivity. The domain reversal during the periodic poling will start in the regions with lower coercive field, i.e. in the areas which are not ion exchanged. As discussed in Section 5.3, a simultaneous increase of the coercive field and decrease of the ionic conductivity can be achieved by ion exchange in a Rb-rich melt.
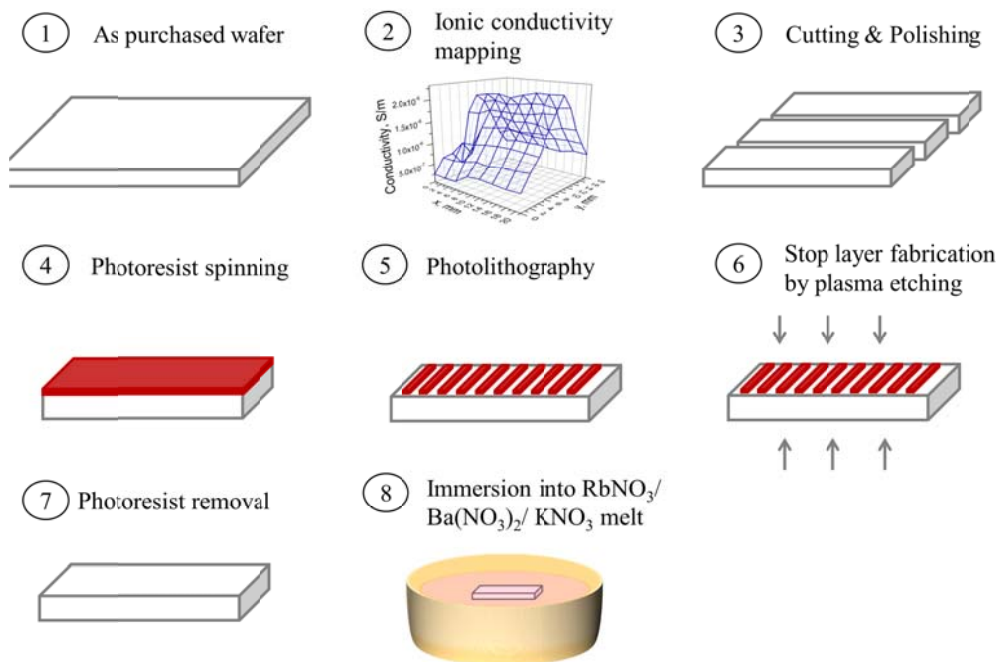
Fig. 6.9: A schematic view of the steps of the coercive field grating fabrication.

6.2.2 Periodic poling

To study the impact of the coercive field grating on the periodic poling process, crystals were patterned with a period of 3.16 µm with a 33 % duty-cycle. The coercive field grating was fabricated performing ion exchange in a Rb-rich melt for 4h at 375 °C. The coercive field in the ion-exchanged regions was increased by 35 % and the ionic conductivity by was decreased by 50 %. The depth of the grating was approximately 70 µm.

Each crystal was poled with planar electrodes and using single 5 ms long triangular pulse with magnitude varying between 7-8 kV/mm. Thereafter, the domain structure was revealed by selective etching. It is worth noting that the etching results in a contrast difference, not only between different domain polarities, but also between ion exchanged and non-exchanged regions. The stress caused by the ion exchange and the altered chemical composition leads to an increase of the etching rate in the ion exchanged regions.

As expected, domain reversal occurs in the non-exchanged regions of the crystals (see Fig. 6.10 (a)). This can be clearly observed on the border between the poled and the unpoled regions. No lateral broadening into the ion exchanged regions can be observed. Thereby, the duty-cycle of the patterned photoresist is transferred to the periodic domain grating, which is a major difference compared to conventional poling using metal electrodes [15]. Moreover, the duty-cycle is maintained throughout the entire thickness of the sample, as evident in Fig. 6.10 (b).
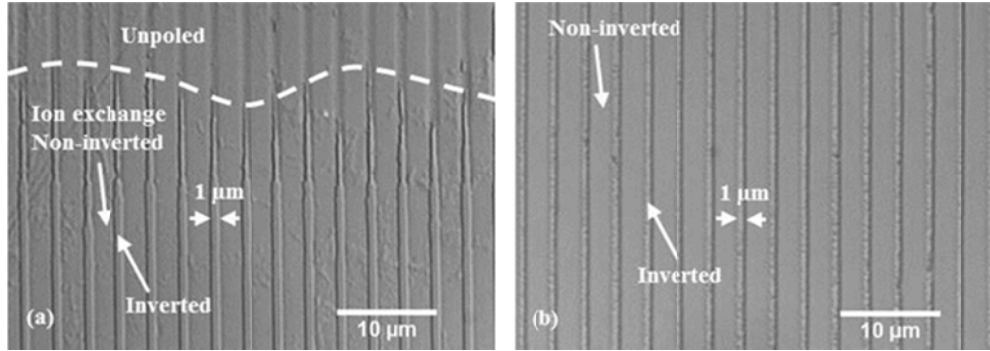
Fig. 6.10: The ferroelectric domain structure revealed by selective etching on the former (a) z^- and (b) z^+ surface of the periodically poled RKTP crystal.

Both underpoling and overpoling are possible outcomes of the poling if the magnitude of the applied electric field is chosen incorrectly. Although domains do not broaden into the ion-exchanged areas, they can broaden and merge in the bulk, below the ion-exchanged region if the magnitude of the applied electric field is too high. Interestingly, for underpoled crystals it can be inferred that the domains start nucleating at the border between the ion-exchanged and the non-exchanged regions, (see Fig. 6.11), where there is a discontinuity in the electric field which probably enhances domain nucleation. In contrast to conventional poling using metal electrodes, the domains do not broaden into the ion exchanged regions. The nucleated domains in the border regions propagate along the crystal thickness to the former z^--surface, maintaining the width and duty-cycle from the z^--surface.
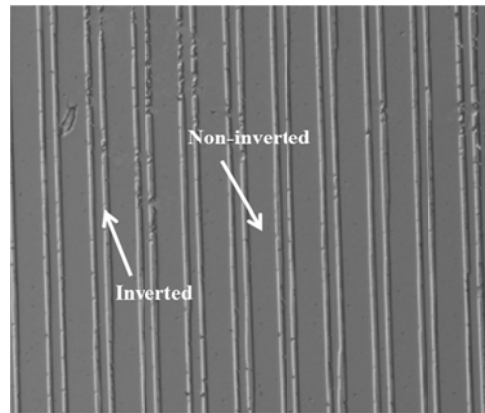

Fig. 6.11: The domain structure of an intentionally under poled sample with $\Lambda = 9.22$ µm on the former z^+ surface.

6.3 Fabrication of sub-µm ferroelectric gratings

Fabrication of sub-µm ferroelectric grating of high quality is essential for realization of QPM interactions with counterpropagating photons, such as MOPO. Attempts have been made to fabricate such gratings in RKTP [18], but homogenous lithographic patterning as well as accurate control of the domain broadening remains significant challenges.

In this work, the domain growth during the poling process was controlled using the developed technique for periodic poling by fabricating an coercive field grating in the crystal

bulk. Moreover, a lithographic system based on laser interference was developed to fabricate sub-µm periodic photoresist patterns with high accuracy.

6.3.1 Lithography

The lithographic interference-based system developed for fabrication of sub-µm photo resist patterns is illustrated in Fig. 6.12.
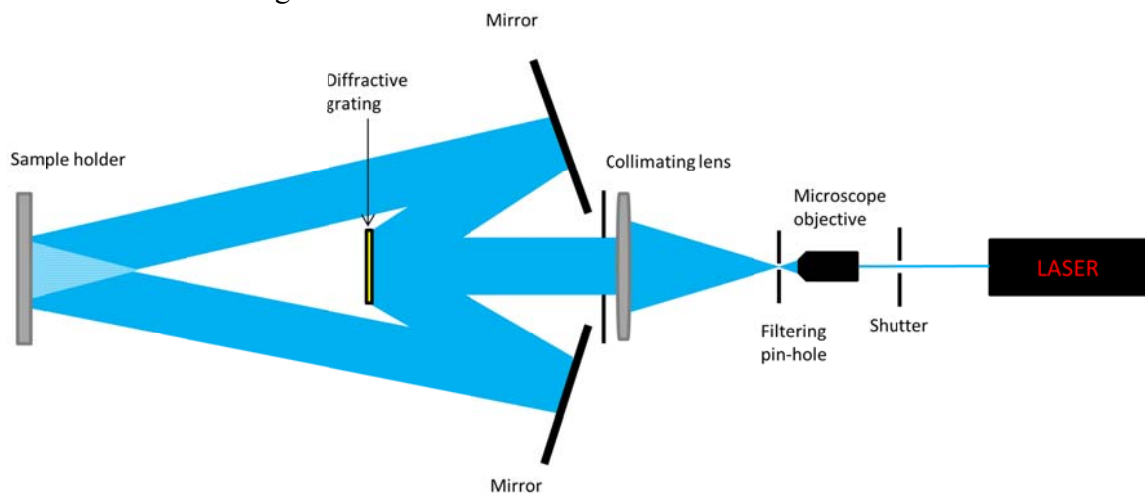

Fig. 6.12: Illustration of the in-house built laser interference lithography setup using a frequency-quadrupled, cw, single mode Nd:YVO$_4$ laser operating at 266 nm as source.

The light source used for this system was a frequency-quadrupled, continuous wave, single mode Nd:YVO$_4$ laser operating at 266 nm. The beam from the laser is focused using a microscope lens, and the spatial mode is cleaned up using a pin-hole. The beam is then collimated and split into the ±1 diffraction orders using a reflective diffraction grating. The two diffraction orders are recombined using highly reflective mirrors, creating an interference pattern at the sample holder. The period of the interference pattern can be controlled by adjusting the angle at which the beams are incident on the sample holder, i.e. by adjusting the angle of the highly reflective mirrors and the position of the reflective grating.

The photoresist that is typically used for contact lithography is not suitable for patterning at 266 nm and, therefore another photoresist needs to be used for this purpose. Most thick positive photoresists used in the deep UV region are so-called chemically amplified resists, in which exposure releases acids in the resist which are diffused and amplified in a subsequent post-exposure baking step. This kind of photoresist is highly sensitive to contamination by base molecules, which neutralizes the acids in the resist, resulting in poor control of the patterning procedure in ambient conditions. However, with the coercive field poling technology, the photoresist layer is not used as an insulator, making the thickness of the photoresist less crucial. Therefore, a thin DUV-sensitive photoresist, which is not chemically amplified, was used for patterning. Fig. 6.13 shows the resulting photoresist pattern profile on the z^--surface of a RKTP crystal. The periodicity of the pattern is 755 nm. The duty-cycle of the pattern is uniform throughout the crystal surface.
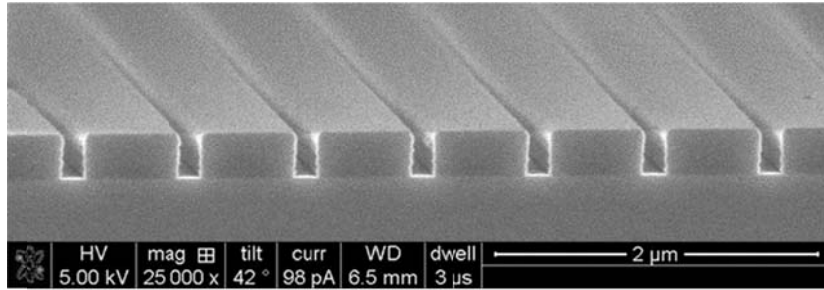
Fig. 6.13: Scanning electron microscope image of the pattern of the exposed in 300 nm thick photoresist using the in-house built laser interference lithography system.

6.3.2 Periodic poling of sub-µm domain gratings

The sub-µm coercive field gratings were created similarly to what is described in section 6.2.2. After the deep UV-laser lithographic patterning, an Al film is evaporated over the photoresist and lift-off is performed leaving a metal grating on the z^- surface which is used as stop layer for the ion exchange process. The duty-cycle of the metal stripes was typically 20 %. A stop layer is fabricated on the z^+ surface using oxygen plasma etching to prevent ion diffusion in or out of this surface.

A coercive field grating was fabricated by ion exchange in a Rb-melt at 330 °C for 4 h resulting in a coercive field increase of 1.5 kV/mm and decrease of the ionic conductivity by 2×10^{-6} S/mm. The temperature was somewhat decreased from 375 °C to 330 °C to minimize the stress induced in the crystal by the ion exchange process. The metal stop layer was removed after the ion exchange process.

Afterwards, the crystal was connected to the external poling circuit using liquid planar electrodes. Poling was performed by application of 5 ms long, symmetric triangular electric field pulses to the sample with a peak magnitude of ~6 kV/mm.

The sample was selectively etched and imaged by AFM, as shown in Fig. 6.14 (a) and (b). One of the crystals was was cut along the *x*-direction and the nonpolar *y*-surfaces were polished to an optical finish. The domain structure on the *y*-surface was imaged by PFM along the polar axis over the full sample thickness. Fig. 6.14 show the domain structure imaged (c) 100 µm and (d) 900 µm below the patterned surface, representative for the entire periodically poled area. The duty-cycle of the inverted domains is approximately 44 % and remains constant over the whole crystal thickness. Note that the duty-cycle on the patterned face appear to be smaller than at 100 µm depth. This can be explained by the fact that the domains slightly broaden when they propagate through the ion-exchange region, and then keep a constant width for the rest of the crystal thickness.
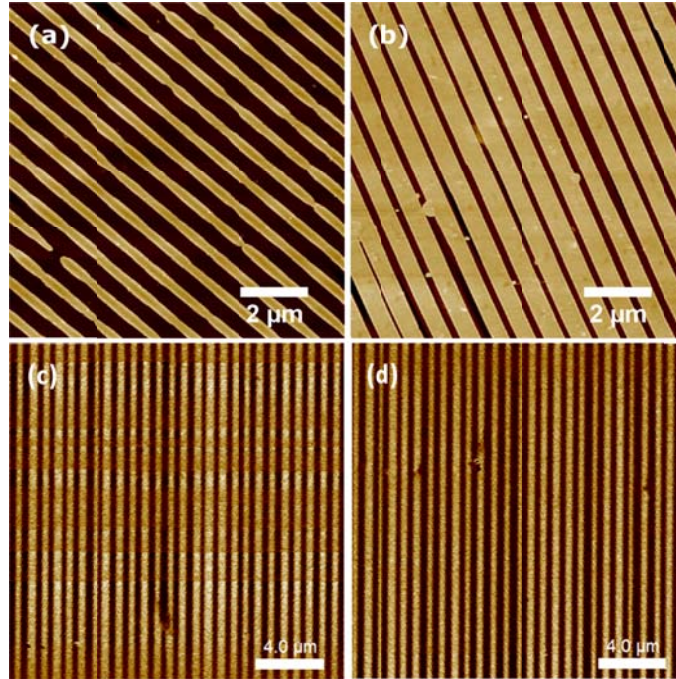
Fig. 6.14: The sub-μm domain grating imaged by AFM on the previous (a) *z*- and (b) *z*+ surface. The domain structure on the nonpolar *y*-surface imaged by PFM (a) 100 μm and (b) 900 μm below the patterned surface [paper III].

6.4 Domain wall stability

An alternative technique to fabricate QPM devices is by direct growth of the periodic domain structures [3]. Peña *et al*. recently demonstrated a technique using a periodically poled KTP crystal template for epitaxial growth below the Curie temperature of KTP, thereby preserving the periodic domain structure of the seed [38]. Using this technique, it would be possible to grow large aperture crystals with short QPM periods, especially if PPRKTP can be used as a template. Although the growth process is performed below the Curie temperature, it is essential to study the thermal stability of the domain gratings at the temperatures at which growth is performed, to ensure formation of high quality domain gratings. There are no reported studies of the thermal stability of domains in KTP isomorphs at epitaxial growth temperatures (700-750 ˚C), although a few studies were performed close to the Curie temperature of KTP [129,130]. Moreover, studying the thermal stability of the RKTP domain gratings also provides fundamental information on the domain wall movement in this material.

Thus, the thermal domain wall stability in RKTP was studied by annealing PPRKTP crystals with periods ranging from 2 μm to 36.4 μm. Several crystals with quasi-periodic domain structures (average periodicity 650 ± 200 nm) fabricated using a self-assembling technique (SARKTP) were also studied [17]. All crystals were heated up with a rate of 25 ˚C/min to 730 ˚C and cooled down at a rate of 2.4 ˚C/min. Altering the ramp rate of the heating did not affect the results, thereby ruling out any influence of the pyroelectric field.

All crystals were etched after the poling, and then again after the annealing process to visualize the movement of the domains. The changes in the domain structure were characterized using optical microscopy and PFM.

Fig. 6.15 shows PPRKTP crystal with $\Lambda = 9$ μm annealed for 4.5 h, which provides a representative picture for the domain wall motion. Fig. 6.15 (a) and (b) are optical micrographs of the domain structures on the previous z^- and z^+ surfaces. In the images the pre-annealing domain walls appear slightly dimmer compared to the post-annealing domain walls, which are sharper. Fig. 6.15 (c) shows Fig. 6.15 (a) imaged by AFM, along with a magnified inset. The corresponding PFM image is shown in Fig. 6.15 (d), with the presence of some topography cross-talk.
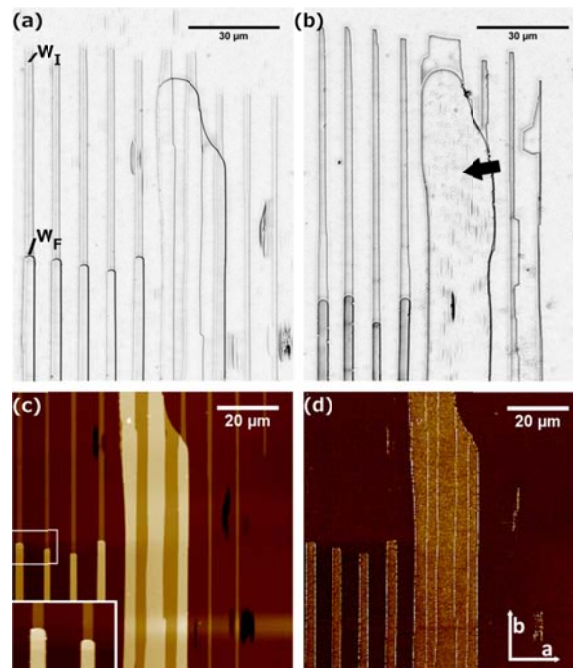

Fig. 6.15: Optical micrographs of the etched domain structures on the former (a) z^- and (b) z^+ surface, along with (c) AFM topography and (d) PFM response of the etched structure showed in (a). The inset in (c) shows a higher magnification scan of the area marker in the white box in (c) [Paper VI].

In agreement to the domain growth in KTP, the domain wall motion is highly anisotropic along the different crystallographic axes. Additionally, the motion of a wall is dependent on whether the domain extends throughout the entire thickness of the crystal or if merging occurs in the bulk. When the domain extends throughout the full thickness of the crystal, back-switching occurs along the y-axis. The average domain wall motion along the y-axis was, in this case, 68 μm on the former z^- surface and 90 μm on the former z^+ surface, measured from the initial position, W_I, to the final position, W_F, shown in Fig. 6.15 (a). Meanwhile, domains with an original head-to-head configuration merge into larger domains and show much less movement along the y-axis, as seen in Fig. 6.15 (b), where the merged domains are marked with an arrow. Along the x-axis the domain wall motion was radically different. On the former z^- surface a

domain expansion by 0.4 µm was measured while a contraction by 0.6 µm was seen on the former z^+ surface.

Domain walls deviating from 180° will be charged and hence have a larger domain wall energy. Moreover, domain walls parallel to the (100) plane are energetically favorable since they do not cut the helical chains [131]. Therefore, the domain walls along the x-axis will move to minimize their angle with the (100) plane. Domains with a head-to-head orientation will merge during the annealing process to obtain straighter domain walls.

In contrast, there is no evidence that minimizing the angle with the (010) plane decreases the domain wall energy. Nevertheless, contraction of tens of µm is observed along the y-direction, which is explained by the domain wall velocity being approximately 30 times higher along the y-axis relative to the x-axis [132]. This indicates that the energy barrier for domain wall movement along this direction is significantly lower. This is in agreement with studies in near-stoichiometric lithium tantalate (SLT) [133,134] and near-stoichiometric lithium niobate (SLN) [135] where the difference in domain wall stability is attributed to the lower energy of the walls in the y-direction of the material.

Domains with sharp and rough edges have high domain wall energy, as the two rightmost domains in Fig. 6.15 (b). These walls have high energy and are therefore very mobile. These walls have larger than normal contraction or smoothening (the merged domain of Fig. 6.15 (b)). The higher propagating speed of these very rough domain walls can be explained by the competition between the formation of new domain steps by the wall and the growth of the steps, as previously explained for lithium tantalate [136].

Fig. 6.16 (a) shows the domain displacement along the y-axis on the z^+ surface as a function of domain period. As evident, the displacement of the domain walls increases in a non-linear fashion as the periodicity of the domain grating decreases. For the crystal with $\Lambda = 36.4$ µm period only smoothening of the sharp domain wall edges was observed, in agreement with the observations by Masiello [129]. In the crystal with $\Lambda = 2$ µm, 250 µm domain wall displacement was observed, and the SARKTP crystals were completely switched back. Moreover, crystals with shorter periods also displayed more severe movement along the x-axis. In many cases individual domains merged into larger domains during the annealing process. Fig. 6.16 (b) shows merging in a domain grating with 2 µm periodicity.
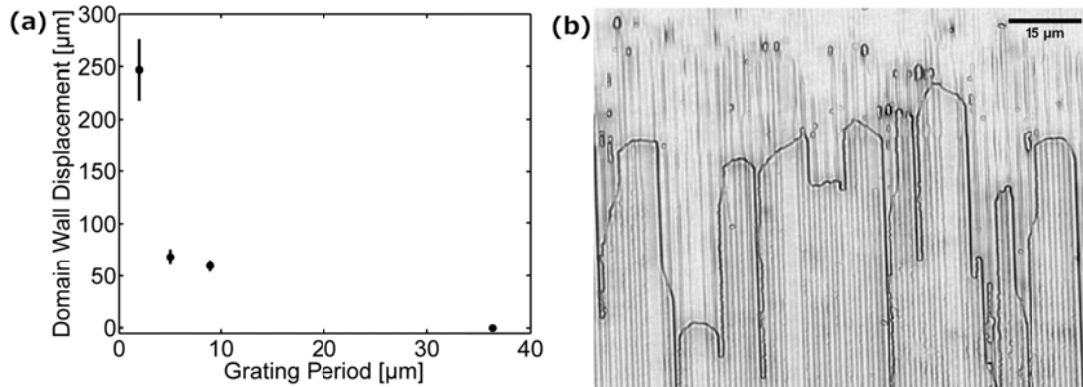
65

Fig. 6.16: (a) the domain wall displacement along the b-axis depending on the domain grating period; and (b) merging of domains of the former z⁻ surface in a Λ = 2 µm grating [paper VI].

The increased domain wall mobility with decreasing period can be understood by considering the ratio of the domain wall area and the domain volume. More narrow domains have a larger ratio and thereby higher domain wall energy and are more unstable. Similar findings have been reported in SLT by Liu *et al.* [134]. Furthermore, Kan *et al.* observed that domains with short inter-domain distance are less stable, and reported evidence of the existence of a repulsive force between neighboring domains [137]. A plausible explanation would be that with short inter-domain distance the domain walls interact with each other, merge or backswitch, depending on the type of bound charges. Regardless, further investigations of this matter are needed.

Thus, in order to use fine-pitch PPRKTP as templates for epitaxial growth, the domain walls should be uncharged and as straight as possible to maintain the domain structure throughout the growth process. This could be addressed by poling thin (300 µm) RKTP crystals, thereby facilitating the formation of uncharged walls, as well as decreasing the domain wall area to volume ratio.

7 Optical Applications of PPRKTP

In this chapter, the optical performance of the devices fabricated throughout this work is discussed. It the first part, PPRPKTP crystals fabricated using conventional electric field poling with metal electrodes have been used to generate high power blue light through SHG, as well as to fabricate laser-written waveguides for QPM SHG operation. In the second part, PPRKTP crystals fabricated using coercive field engineering through ion exchange have been used to explore the possibility to integrate QPM devices with refractive index gratings. Finally, the high-quality sub-μm PPRKTP crystals were evaluated as QPM MOPO devices in both the picosecond and nanosecond regime, thereby demonstrating MOPO processes never before realized.

7.1 High-power blue generation in PPRKTP

With the constant increase of available laser power, it is necessary to explore the material limitations of the nonlinear crystals. This is particularly relevant for new periodically poled materials, such as RKTP, where no data was available prior to this work. PPKTP and PPRKTP are considered to be the material of choice for low and medium power visible applications. To quantify the performance of the crystals a number of studies have been performed in the green spectral range [14,90,138,139], while only a few studies have been reported in the blue spectrum due to the lack of high power laser sources around 900 nm. Blue lasers have numerous applications in spectroscopy, underwater communication and material processing, which is why it is relevant to study the performance in this spectral range. Moreover, most studies are performed in KTP which has lower resistance to optical damage than the isomorph RKTP.

The performance of a PPRTP with a QPM grating period of $\Lambda = 6.03$ μm is studied, for phase matching 946 nm, thereby generating 473 nm by SHG. The dimension of the PPRKTP crystal was $10 \times 5 \times 1$ mm^3 ($x \times y \times z$), with a QPM grating length of 8 mm. The PPRKTP was poled using conventional electric field poling and the resulting domain structure can be seen in Fig. 6.7. Neither of the crystal end faces was anti-reflection coated.

Prior to the high power tests, the sample was evaluated using a continuous wave, tunable Ti:Sapphire laser. The effective nonlinearity was measured to be $d_{eff} = 9.5$ pm/V and the temperature acceptance bandwidth was 3 ˚C. Moreover, the linear absorption was measured to 8.2 %/cm at the second harmonic wavelength 473 nm, which is in agreement with earlier reported data [140].

The RKTP crystal was pumped using an in-house built Nd:YAG single-crystal fiber oscillator operating at 946 nm, which was used as the fundamental source in the experiments. The laser could be operated both in continuous wave and Q-switched mode [141]. In continuous wave, it delivered up to 11.5 W of laser output power with a near-Gaussian intensity profile (M² < 1.3) and a spectral width < 0.04 nm. In the Q-switched mode, it delivered 10 W at 18 kHz with pulse widths of 45 ns and a similar beam profile to the cw operation.

The experimental setup is illustrated in Fig. 7.1. The fundamental power incident on the PPRKTP crystal was controlled using a polarizer-waveplate arrangement. Furthermore, the

temperature of the PPRKTP was controlled using a thermoelectric element. The fundamental beam was focused in the PPRKTP to obtain optimal conversion efficiency. After the PPRTKP crystal, the second harmonic power was filtered from the fundamental power using a dichroic mirror and then collected in a power meter.
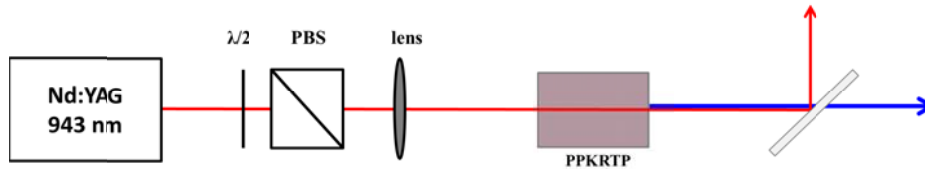

Fig. 7.1: Experimental set-up for high power blue light generation through SHG.

First, the performance of the PPRKTP was evaluated for continuous wave operation. The fundamental beam was focused to a beam waist of $w_0 = 25$ μm, close to the optimal spot size for this crystal length, defined by the Boyd-Kleinmann, $w_0 = 26$ μm. The measured SHG power and conversion efficiency are displayed Fig. 7.2. The SHG power reached 795 mW for an input power of 11.5 W at 946 nm, corresponding to a conversion efficiency of 7 %. The temperature for optimal phasematching of the PPRKTP was 85.2 °C.
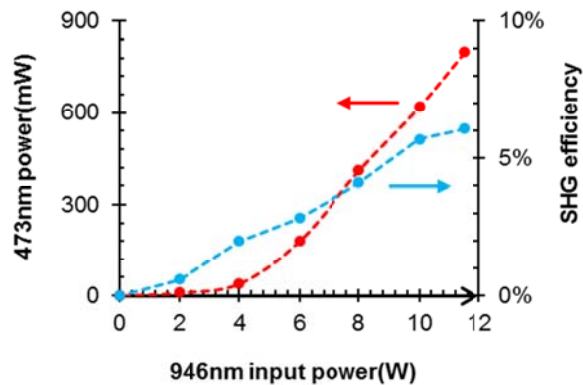

Fig. 7.2: cw SH power and conversion efficiency vs. fundamental power.

The generated SHG power decreased relatively rapidly over time. Therefore, the SH power was recorded over 30 min, with two different focusing conditions, $w_0 = 25$ μm and $w_0 = 35$ μm. The measured SHG output power over time is shown in Fig. 7.3. For a beam waist of $w_0 = 25$ μm, the initial SHG output power was 795 mW, but remained above 750 mW for no more than a few minutes. After approximately 30 min of operation the SHG output power stabilized at 250 mW. As the PPRKTP was translated to another point, the SHG output power returned to the previous maximum power of 795 mW. For the larger beam waist of $w_0 = 35$ μm, the maximum SHG output power was initially measured to 400 mW. As can be seen in Fig. 7.3, the rate of decay is significantly decreased. However, a decay of the SHG output power is still present.
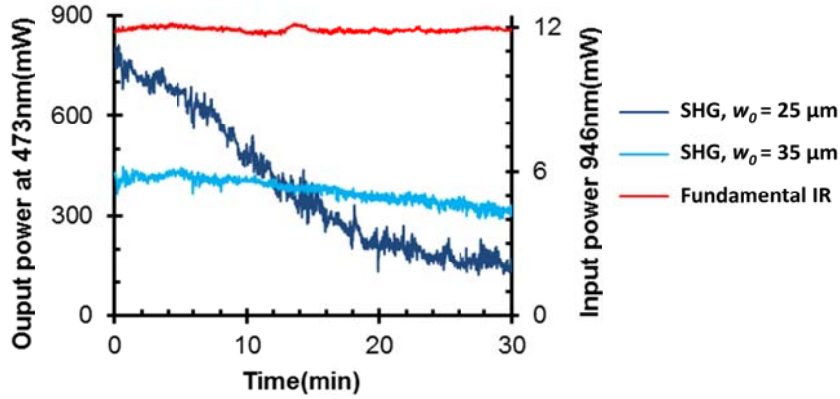
Fig. 7.3: Stability of cw infrared and blue average power.

The above observed results are in agreement with what has been previously reported for generation of green light in KTP [90,142]. The decaying SHG output power can be attributed to absorption of visible light in the KTP isomorphs [14,90,138,143]. At sufficient intensity of the blue SHG, the absorption of the SHG becomes non-negligible, resulting in heating of the crystal. With the absorption being proportional to the intensity of the generated SHG, a thermal gradient is formed over the crystal length. The thermal gradient results in a corresponding change of the refractive indices, thereby altering the QPM condition by so-called thermal dephasing [90,138]. From Fig. 7.3 it can be seen that a decrease of the fundamental beam intensity (either by looser focus or lower pump power) significantly changes the rate of decay. This can be attributed to corresponding decrease in intensity of the generated blue second harmonic as well as of the fundamental beam. Liao *et al.* reported a threshold for the thermal dephasing at 78 kW/cm^2 for green light at $\lambda = 532$ nm in PPKTP [138]. However, the threshold is dependent of a number of parameters such as crystal composition, optical quality, wavelength of the absorbed wave to mention a few.

The thermally induced dephasing was further investigated by measuring the SHG output power as a function of temperature, as shown in Fig. 7.4. The pump beam was focused to a beam waist of $w_0 = 25$ μm and the measurement was performed at 100 mW and at 11.5 W of pump power. At 11.5 W of fundamental power, the temperature of the PPKRTP crystal was scanned from 92 ˚C to 76.5 ˚C in steps of 0.5 ˚C, while at 100 mW of fundamental power the temperature was scanned from 92 ˚C to 78.7 ˚C in steps of 0.3 ˚C. At each measurement point, the generated SHG output power was measured after approximately 3 minutes, once the temperature of the PPRKTP crystal had stabilized. At low fundamental power, 100 mW, incident of the PPRKTP crystal, the phase matching curve follows the expected *sinc*^{2}-curve with a temperature acceptance bandwidth of 3 ˚C. Meanwhile, at maximum fundamental power, 11.5 W, the measured phasematching curve is severely distorted from the expected *sinc*^{2}-curve. As the temperature is decreased from the start temperature of the measurement, the optimal QPM temperature is approached, and the intensity of the generated second harmonic increases rapidly. With the onset of the high intensity second harmonic, the absorption of the blue light is non-negligible. The absorption of the blue second harmonic results in a thermal gradient over the

69

crystal, resulting in a distortion of the phase-matching curve. Moreover, with the correlated waiting time at each measurement point, dephasing has already set in, thereby severely distorting the curve. Nevertheless, the measured high power phase matching curve resembles previously reported phase matching curves affected by dephasing [144].
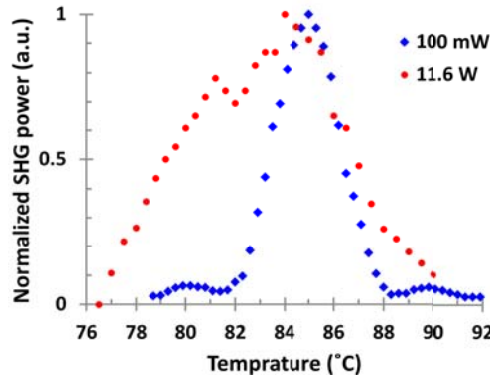

Fig. 7.4: Phase matching curves in cw for 100 mW (blue) and 11.6 W (red) of fundamental power.

It could be argued that the thermal dephasing could be attributed to formation of so-called grey tracks, by blue light induced infrared absorption (BLIIRA), two-photon absorption (TPA) of the fundamental and second harmonic, and/or the linear absorption of the fundamental and the second harmonic. Recent studies have shown that the BLIIRA threshold in the PPRKTP used is tens of MW/cm^2 [89]. However, the maximum peak intensity reached in this experiment was only 1.17 MW/cm^2 for the fundamental beam. Furthermore, no grey-tracks could be observed in the crystal during inspection in an optical microscope. The threshold of TPA is on the same order of magnitude as that of BLIIRA [90,143,145]. Therefore, the main contribution to the thermal dephasing at the intensities used is the linear absorption of the generated blue second harmonic. In principle, the thermal gradient created by the absorption of the SHG could be compensated by accurate cooling of the PPKRTP to keep the magnitude of the gradient lower than the thermal acceptance bandwidth of the QPM device. However, at high intensities, and hence, large magnitude of the thermal gradient, a highly accurate thermoelectric element with a counteracting gradient is needed to compensate for the absorption-induced thermal gradient of the crystal, which is not easy to achieve.

The PPRKTP crystal was then evaluated in the pulsed regime. Since the second harmonic grows much faster with average power in the pulsed than in the cw regime, a much looser focusing is required to limit the detrimental thermal effects. For the pulsed experiment, the performance of the crystal was evaluated with fundamental beam radius of w_0 = 125 μm, 175 μm and 225 μm. For each beam radius, the incident fundamental power was increased gradually, Watt by Watt. For each power level, the PPRKTP temperature was tuned to obtain maximum conversion efficiency. The measured SHG output power and conversion efficiency for each beam size are displayed in Fig. 7.5.
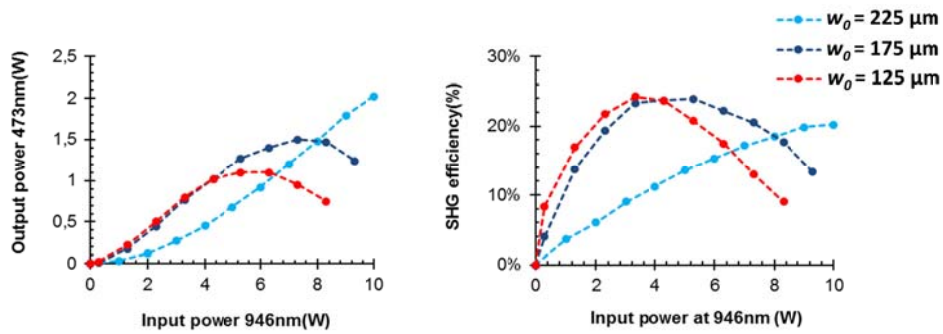
70

Fig. 7.5: Output SH power at 473 nm as a function of average fundamental power (left) and SHG conversion efficiency as a function of 946 nm average power for the three different beam sizes (125 µm, 175 µm, and 225 µm).

The maximum average SHG output power, 2 W, was obtained using the largest beam size, w_0 = 225 µm, at full fundamental power, 10 W. This corresponds to a conversion efficiency of 20 % and pulse energy of 0.56 mJ of light at 473 nm. As the beam size of the fundamental was decreased, the SHG power reached a maximum value and then rolled off as the average fundamental power was further increased. This can be attributed to both depletion of the pump energy and absorption of the generated second harmonic in the end of the crystal where the intensity of the blue light is the highest. However, in contrast to the cw measurement, the SHG output power was stable at the maximum power over time, as displayed in Fig. 7.6.
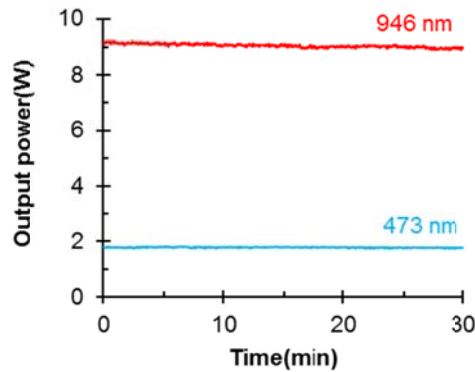

Fig. 7.6: Fundamental and second harmonic power stability.

The phase matching curves, measured at average pump powers of 0.5W and 10W with a beam waist of w_0 = 225 µm are shown in Fig. 7.7. The performance at both high and low pump power is quite different from what was observed in the cw regime. At low fundamental pump power, 0.5 W, the phase matching curve follows the expected $sinc^2$-curve (dashed line). Meanwhile, the phase matching curve at high pump power, 10 W, tilts towards lower temperature which is typical when thermal dephasing is present.
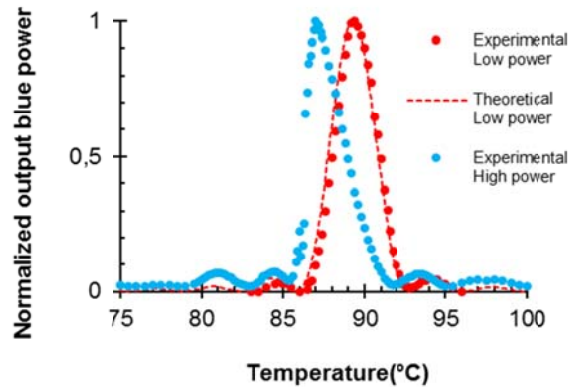
71

Fig. 7.7: Phase matching curve in Q-switched mode for low (0.5 W) and high (10 W) power. The theoretical fit is a classical *sinc²*-function.

The influence of the thermal effects on the SHG process was further investigated by measuring the SHG power at constant fundamental average power while the temperature of the PPRKTP crystal was decreased from the low power optimal phase matching temperature of 89.5 ˚C. The change in conversion efficiency as a function of temperature correction, ΔT, is displayed in Fig. 7.8 for each beam radius. Interestingly, the maximum conversion efficiency is obtained at the same temperature correction for each beam radius of the fundamental beam. The temperature correction of 2-3 ˚C is in good agreement with the measured temperature acceptance bandwidth of the used PPRKTP crystal. This can be understood by considering the dynamics of the SHG process. The generated SHG power increases as the fundamental wave propagates along the *x*-axis of the QPM device, and the maximum power is obtained in the rear part of the crystal. At high fundamental average power, the absorption of the blue second harmonic is non-negligible, which results in heating of the crystal, and creation of a temperature gradient along the *x*-axis of the crystal. This temperature gradient results in a tilt of the phase matching curve, as can be seen in Fig. 7.8, and the sample has to be cooled to compensate for the heat. As long as the temperature difference between the front and end face of the crystal is within the temperature acceptance bandwidth of the QPM device, the effect can be compensated by adjusting the temperature of the PPRKTP crystal. However, if the temperature difference between the two end faces is larger than the temperature acceptance bandwidth the QPM device, it can no longer be compensated by cooling of the device. Therefore, this results in a decreased effective length of the QPM device, thereby decreasing the efficiency of the SHG process.
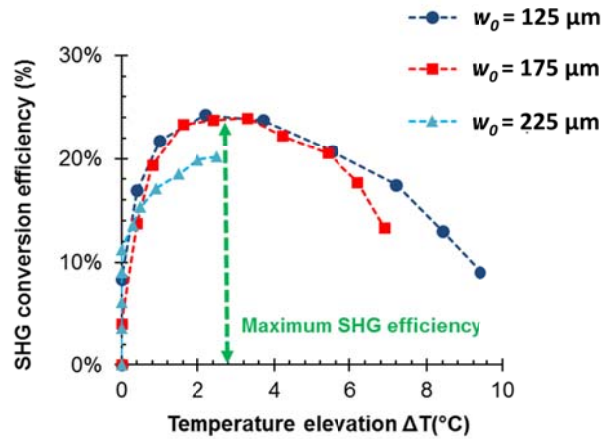
72

Fig. 7.8: Temperature correction ΔT (°C) versus the SHG conversion efficiency for different fundamental beam sizes (125 μm (dark blue), 175 μm (red) and 225 μm (light blue)).

The absorption induced heating of the PPRKTP crystal is not only affecting the conversion efficiency of the QPM device, but might also affect the beam quality of the generated second harmonic. A CCD array camera was used to measure the intensity distribution of the generated second harmonic beam at 0.5 W and 10 W of average fundamental power, shown in Fig. 7.9. The measurement was performed at the same position in the crystal at both 0.5 and 10 W of pump power. As evident in Fig. 7.9, the heating will also cause a significant thermal lensing inside the crystal, which will modify the intensity distribution. As the pump power is increased, the SHG beam becomes more elliptical and the beam profile becomes degraded.
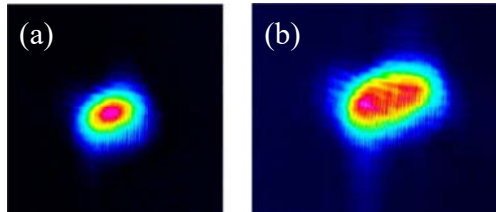

Fig. 7.9: 473 nm beam profile at (a) 0.5 W and (b) 11 W of average fundamental power.

Over all, the performance of the PPRKTP in this investigation is mainly limited by thermal loading caused by linear absorption of the generated blue second harmonic. Although detrimental at increasing intensities, the thermal dephasing could possibly be counter-engineered by pre-chirping of the QPM grating, or by accurate design of a gradient thermoelectric element to compensate for the absorption induced thermal gradient.

7.2 SHG in laser-written PPRKTP waveguides

In a waveguide, the interacting waves can be confined to a small area over comparatively long distances without diffraction, thereby enabling a highly efficient nonlinear process also when using pump sources providing low or moderate powers. QPM waveguides are therefore attractive for development of, e.g., compact light sources and integrated optical circuits.

Although well developed, waveguides fabricated using ion exchange processes in KTP suffer some major drawbacks. Due to dispersion and the refractive index distribution in such

waveguides (see Fig. 5.1), the depth of the guided mode is highly dependent on the wavelength. Typically, the visible light is guided closer to the surface than near-IR wavelengths, resulting in poor overlap between the interacting waves in the nonlinear process, in turn leading to a reduction of the conversion efficiency. Moreover, the fabrication method suffers from poor reproducibility as the diffusion coefficients in KTP depends on sample conductivity [121].

An alternative method to fabricate waveguides is by exploiting the nonlinear absorption of focused femtosecond long pulses to create microstructures in the material [146]. The formation of the microstructures results in creation of stresses in the material surrounding the microstructure, and thereby a locally increased refractive index in the neighboring region, which can be exploited for waveguiding. In KTP, Laurell *et al.* demonstrated a double track writing method can be used to fabricate high quality, low loss channel waveguides [43].

In this work, in collaboration with the Huber-group at Hamburg University, channel waveguides were written into an 8 mm PPRKTP crystals with a QPM period of $\Lambda = 6.03$ μm, for SHG of 943.40 nm, with a $d_{eff} = 11$ pm/V. A Ti:Sapphire femtosecond laser system with center wavelength of 755 nm, providing 160 fs long pulses at 1 kHz was used to write the double track channel waveguides. The laser was focused 250 μm below the crystal surface and the double tracks were written along the *x*-axis of the crystal. The two tracks were separated by 18 μm, as shown in Fig. 7.10.
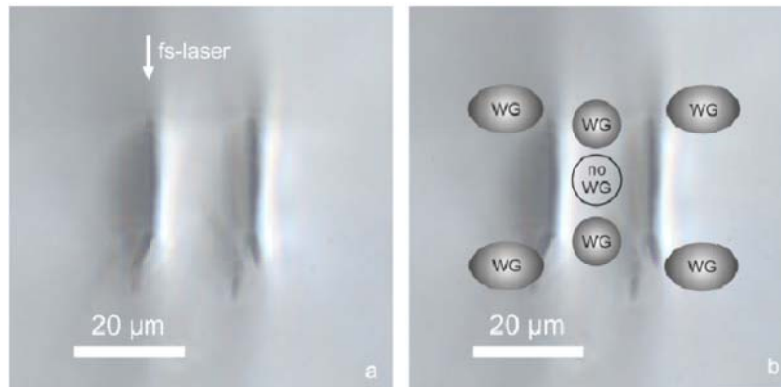

Fig. 7.10: Bright field microscope image of the *x*-surface showing the (a) laser-written tracks and (b) the areas where waveguiding can be obtained (from [43]).

The total passive losses for the near-IR radiation were 2.2 dB, while the losses in the visible region were 1.6 dB. These losses include incoupling and propagation losses, which agrees well with previously reported results [43]. The higher losses in the near-IR can be explained either by larger coupling losses or stronger leakage in the waveguide.

The SHG performance was evaluated using a tunable, continuous wave Ti:Sapphire laser coupled into the waveguide using an f = 40 mm lens. The crystal temperature was kept at 22.9 ˚C and phase matching was obtained at 943.18 nm. The slight shift in the phase matched wavelength compared to the bulk can be explained by the slightly higher refractive index of the waveguide. The waveguide generated a maximum of 76 mW of SHG when pumped with 1610 mW of fundamental power. The generated SHG power and conversion efficiency are presented in Fig. 7.11. This corresponds to a conversion efficiency of $\eta = 4.7$ %, i.e normalized

conversion efficiency of $\eta = 4.6$ %W^{-1}cm^{-2}. Assuming typical coupling losses of 10 %, the conversion efficiency can be corrected to $\eta = 5.3$ % and the normalized conversion efficiency $\eta = 5.8$ %W^{-1}cm^{-2}. However, the passive losses for the fundamental beam are significantly larger than 10 %, and higher conversion efficiencies could be expected if these losses can be reduces.

Accounting for typical coupling losses of 10 % (0.5 dB) and the measured passive losses for the fundamental beam, the nonlinear coefficient can be estimated to $d_{eff} \sim 9$ pm/V. This is in good agreement with the measured d_{eff} of the bulk crystal, indicating no degradation of the QPM structure occurs during the fabrication process.

In Fig. 7.11, the generated SHG power has been fitted to the expected quadratic dependency of the fundamental power. This measurement was performed by optimizing the wavelength at the highest input power and thereafter adjusting the temperature of the crystal as the power was reduced to maintain maximum conversion efficiency at each point. As can be seen, the generated SHG deviates from the expected quadratic behavior at 1.1 W, corresponding to a peak intensity of 0.96 MW/cm^2. This deviation can be attributed to thermal dephasing of the QPM device from absorption of the generated blue light, effectively heating the crystal and changing the QPM wavelength [90,142].
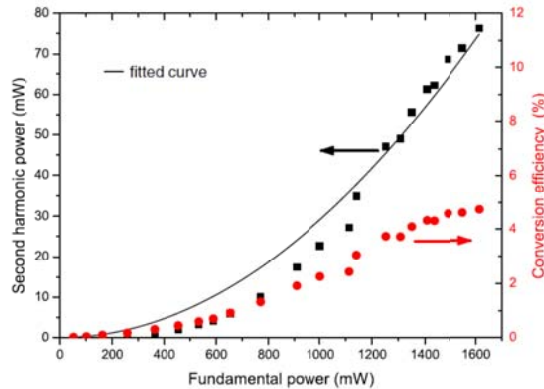

Fig. 7.11: Measured SHG power (black dots) with the fitted quadratic behavior (black line) and the conversion efficiency (red dots) [paper V].

The absorption induced dephasing of the waveguide was investigated by measuring the generated SHG power as a function of temperature while the pump power was kept to 1 W and 1.6 W, shown in Fig. 7.12. At 1 W of pump power the SHG process is phase matched at 943.18 nm when stabilized at 22.2 ˚C. The measured curve follows the expected $sinc^2$-function, which is shown as a solid line in Fig. 7.12. The temperature acceptance bandwidth at 1 W pump power was measured to 3.3 ˚C. As the pump power was increased to 1.6 W, the temperature for optimal phasematching increased to 22.9 ˚C. Moreover, the first side lobe to the right, at 29 ˚C, has become enhanced, which is typical for thermally induced dephasing [147]. The shift of 0.7 ˚C for the phasematching corresponds to a wavelength shift of 0.2 nm of the Ti:Sapphire laser during the measurement. Finally, the QPM wavelength temperature dependence was measured from 8.5 ˚C to 65 ˚C, resulting in a tuning rate of 0.053 nm/˚C.
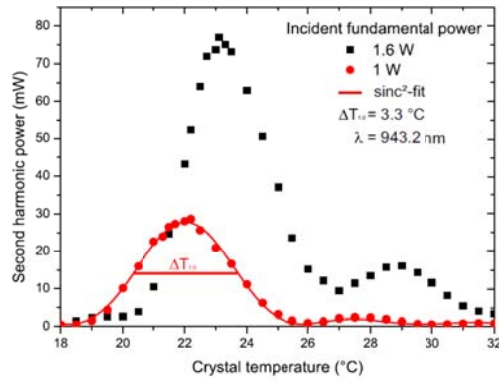
Fig. 7.12: SHG power as a function of crystal temperature at 1 W (red) and 1.6 W (black) of pump power. At 1 W pump power the measurement is fitted to the expected *sinc*²-function [paper V].

The near field intensity distribution in the waveguide of the fundamental and second harmonic wave were measured using a CCD camera, and are shown in Fig. 7.13. The white ellipses show the laser written tracks forming the waveguide. Both the fundamental and the second harmonic waves are centered between the tracks and slightly shifted to the bottom. The size of each mode is determined by the refractive index profile for respective wavelength. The guided mode of the fundamental wave is elliptical with a size of 12.8 µm × 22.3 µm ($1/e^2$). The guided second harmonic mode is smaller than the fundamental, with a size of 9.4 µm × 11.8 µm ($1/e^2$). The center of gravity of the two modes is at a similar position, thereby resulting in a large mode overlap, which is important for obtaining high conversion efficiency. This is typically not the case for ion exchanged waveguides where the fundamental mode penetrates deeper into the material than the second harmonic, thereby limiting the mode overlap and conversion efficiency. The overlap area, A_0, can be calculated using Eq. (2.37) to be 465 µm² from the measured beam profiles.
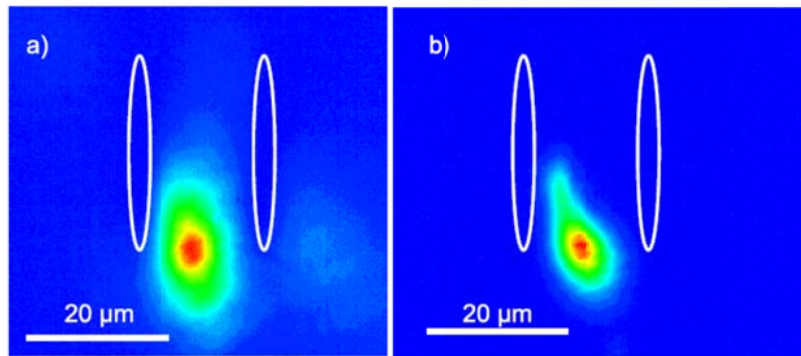
Fig. 7.13: The intensity distribution of the guided (a) fundamental and (b) second harmonic modes [paper V].

The demonstrated laser written waveguide show excellent performance with no apparent degradation of the waveguide or of the QPM structure. The modal overlap of the interacting waves is superior to that of ion exchanged waveguides, and could possibly be further improved by altering the distance between the laser-written tracks. This fabrication method could therefore be an excellent alternative for fabrication of waveguides in PPRKTP crystals for a wide range of applications.

76

7.3 Optical properties of ion exchanged PPRKTP

In the previous chapter, the advantages of using a coercive field grating formed by ion exchange for fabrication of QPM devices with short periods in RKTP were discussed. For devices with sub-µm periods, the formation of the coercive field grating by ion exchange in the crystal bulk was proven to be a crucial step in the fabrication process.

It is well established that the ion exchange process increases the refractive index in the exchanged region and, if the ion exchanged region is deep enough, the refractive in the crystal bulk can possibly be engineered, and thus devices with a simultaneous linear and nonlinear grating can be obtained. For this purpose, it is essential to study the impact of the ion exchange process on the optical performance of the fabricated QPM devices.

To do this, a representative PPRKTP crystal with period $\Lambda = 3.16$ µm exchanged for 4 h in a Rb-rich melt at 375 °C was evaluated in a single pass SHG experiment with a tunable, continuous wave, z-polarized Ti:Sapphire laser.

Close to the patterned surface, in the ion exchanged region, the fundamental power was distributed in a wide range of waveguide modes, resulting in low power SHG over a broad wavelength range. In this case, each fundamental mode experiences its own refractive index and corresponding phase matching wavelength, all together leading to low conversion efficiency in this region.

Below the ion exchanged region (i.e. ~70 µm) the conversion was uniform and efficient over the full aperture of the PPRKTP crystal. 3.4 mW of blue light was generated with 520 mW of fundamental power at $\lambda = 795$ nm, corresponding to a normalized conversion efficiency of 1.7 %W^{-1}cm^{-1} and an estimate of $d_{eff} = 10$ pm/V. This is close to optimal d_{eff} for KTP, and similar performance to what has been obtained for conventional poling using metal electrodes in RKTP [88].

The impact of the ion exchange process manifests itself as a refractive index gradient along the polar axis throughout the full thickness of the crystal, and not only in the ion exchanged region. This effect was evaluated by translating the crystal in steps of 50 µm along the polar direction, well below the ion exchanged region, while keeping the temperature of the PPRKTP constant and measuring the QPM wavelength of the fundamental beam, shown in Fig. 7.14 (a). The phase matched wavelength changes approximately linearly with distance from the patterned surface along the polar direction. The step-like appearance of the curve is an artifact from the limited resolution (0.05 nm) of the optical spectrum analyzer. The total change of the fundamental QPM wavelength is $\Delta\lambda = 0.21$ nm. It corresponds to a total refractive index change $\Delta n_f - \Delta n_{SHG} = 4 \cdot 10^{-4}$ over the crystal thickness.

The change in QPM wavelength was further verified by measuring the temperature tuning curves of at two positions in the crystal bulk, at 100 µm and 600 µm below the patterned surface, while the pump wavelength was fixed at $\lambda = 784.98$ nm. The tuning curves are shown in Fig. 7.14 (b). Both curves have a full width half maximum of $\Delta T_{FWHM} = 1.9$ °C, confirming a high quality and homogeneity of the QPM grating over the full crystal depth. The QPM condition shifts towards higher temperatures as the distance to the patterned surface increases.

The total shift if temperature over 500 μm thickness is $\Delta T = 2.3$ nm, corresponding to $\Delta\lambda = 0.13$ nm, which is in good agreement with the results in Fig. 7.14 (a). This shift in the QPM condition is attributed to remnant stresses in the crystal from the ion exchange process.
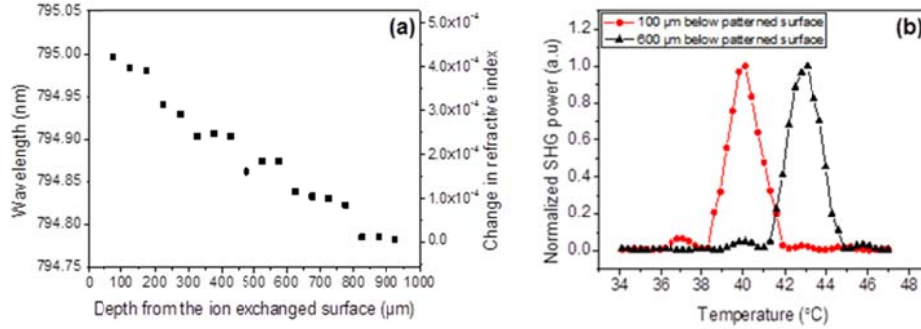

Fig. 7.14: (a) Measurement of the QPM wavelength over the sample thickness at constant temperature. (b) SHG phasematching temperature curves at two positions along the polar axis with constant fundamental wavelength [Paper I].

7.4 MOPO in sub-μm PPRKTP devices

The possibility to engineer ferroelectric domain gratings with sub-μm periodicities enables realization of nonlinear optics involving naturally counterpropagaing photons, e.g. MOPO [13,20] and backwards propagating SHG [17,21]. These counterpropagaing nonlinear optical interactions possess unique spectral, tuning and coherence features, in contrast to the co-propagating counterpart. The counter propagating geometry of the MOPO provides excellent control of the generated parametric waves. Moreover, the low sensitivity to temperature fluctuations and pump beam orientation makes the device inherently robust.

In this section, the fabricated sub-μm PPKRTP are evaluated as QPM MOPO devices. As it will be shown, the high quality of the fabricated QPM gratings in this work enables MOPO processes which have not been previously experimentally realized.

7.4.1 Ps-pumped MOPO: Cascaded processes

For a highly efficient process, which is enabled by the use of high quality QPM devices, the down converted signal and idler waves can reach significant intensities. At sufficiently high intensity, the generated signal can act as pump source for a second, cascaded MOPO process. The phase matching condition for the primary and the secondary, cascaded MOPO is given by:

$$\begin{aligned}
k_p &= K_G + k_{s1} - k_{i1} \\
k_{s1} &= K_G + k_{s2} - k_{i2}
\end{aligned}$$

(7.1)

Here, K_G is the grating vector, and k_m, $m = p,s,i$, is the grating vector for the pump, signal and idler waves. 1 and 2 refers to the primary and secondary process, respectively. A sketch of the phase matched wave vectors involved in the MOPO process is shown in Fig. 7.15.
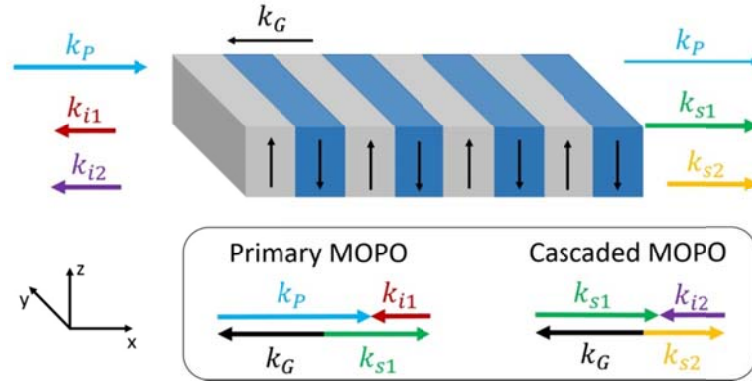
Fig. 7.15: Illustration of the phase matching condition for the primary and secondary cascaded MOPO [paper II].

The cascaded MOPO process is significantly different from cascaded conventional co-propagating OPOs. Efficient cascaded processes in a conventional co-propagating OPO often requires multiple QPM gratings and/or advanced cavity designs [148,149], while in the MOPO, the process is controlled by the peak intensity of the forward propagating waves and the length and quality of the QPM device. Moreover, with the phase information from the pump being transferred to both the signal and idler in the co-propagating OPO, further components are needed in the cavities to generate a narrowband output, thereby adding complexity to the cavity designs. In contrast, no cavity is needed to provide feedback for the MOPO process, making the MOPO inherently stable and robust.

In this work, a regenerative Ti:Sapphire amplifier providing 240 ps long pulses at 1 kHz repetition rate was used to pump the sub-µm PPRKTP crystals, with period of $\Lambda = 755$ nm. The pulses have 10 nm bandwidth (FWHM) centered around 802 nm with a positive linear frequency chirp of 123 mrad/ps^2. The pump light was polarized the crystal z-axis and launched along the crystal x-axis and focused to a beam waist of 105 µm. The pump pulse energy was controlled using a polarizer/half-waveplate arrangement.

The measured conversion efficiency and the pump depletion of a typical PPRKTP crystal are shown in Fig. 7.16. The primary MOPO generated a forward travelling signal wave, $s1$, centered at 1125 nm and a backward propagating idler, $i1$, at 2763 nm. The primary MOPO has a threshold at 39.4 µJ, corresponding to an intensity of 0.64 GW/cm^2. A cascaded MOPO pumped by $s1$ generates a forward propagating signal wave, $s2$, centered at 1898 nm and a counterpropagating idler wave, $i2$, at 2739 nm. The threshold for the cascaded MOPO was 22 µJ of energy of the primary signal, corresponding to 108 µJ of pump energy. At 202 µJ pump energy the pump depletion reached 61 % while the $s1+i1$ power conversion efficiency reached 43 %, with signal energy of 62 µJ. At this pump energy, the cascaded secondary MOPO reached a $s2+i2$ conversion efficiency of 8 %, with $s2$ energy of 9 µJ. The maximum conversion efficiency for the primary MOPO was reached at 130 µJ pump energy. Above this energy, the depletion of $s1$ because of the secondary MOPO process becomes significant, and the efficiency of the primary MOPO process rolls off. As the pump energy increases above 150 µJ, there is a discrepancy between the pump depletion and the total conversion efficiency of the primary and

79

the secondary, cascaded MOPO process. This discrepancy can be attributed to a third MOPO process pumped by the secondary signal. The third MOPO generates a counterpropagating signal at 2762 nm and a forward-propagating idler at 5.9 μm, which is mainly absorbed by the material.
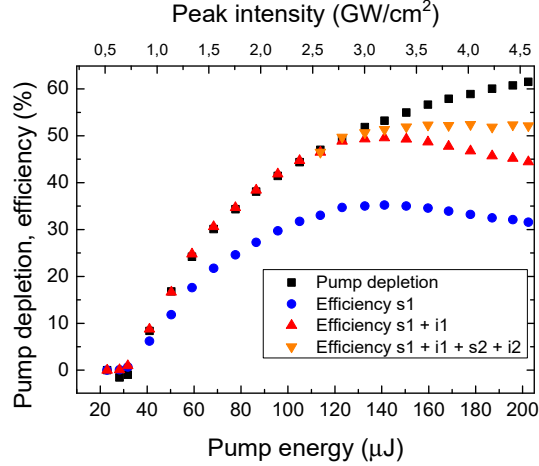

Fig. 7.16: The measured conversion efficiency of the primary signal (blue), primary signal and idler(red) and primary and secondary signal and idler (orange) along with the pump depletion(black) of the MOPO process [paper II].

The effective nonlinear coefficient, d_{eff}, can be estimated from the threshold of the primary MOPO using Eq. (2.45) as discussed in Section 2.7 . With the effective QPM grating length of 6.4 mm the estimated nonlinear coefficient becomes d_{eff} = 9.77 pm/V, close to the value for a perfect QPM grating is KTP [150].

One of the unique features of the MOPO, resulting from the counter-propagating geometry of the interaction, is that the phase modulation of the pump is coherently transferred to the forward-propagating parametric wave, while the counter-propagating wave retains a narrow bandwidth [23,151]. This implies that the positive frequency chirp of the pump will be transferred to *s1*, and, in turn, to *s2*. Fig. 7.17 compares the spectra of (a) the pump, (b) *s1*, and (c) *s2* at different pump energies. Note that due to the linear chirp of the pump spectrum, the pump spectrum is not depleted uniformly. Depletion occurs first on the short wavelength side of the pump spectrum, here corresponding to the trailing edge of the pulse, reflecting the time delay required to establish the distributed feedback. As the pump energy is increased, the time delay is reduced, and longer wavelengths in the pulse spectrum also get converted efficiently. For instance, at the pump energy of 203 μJ, the remaining undepleted part of the pump has FWHM length of 93 ps, which is comparable to the cumulative time of 80 ps, which is required for the pump to travel through the QPM structure and the idler to travel back to the beginning of the structure. At the pump energy of 76 μJ, when only the primary MOPO process is active, the generated *s1* pulse length can be estimated from the depleted part of the pump which has FWHM length of 141 ps. The measured FWHM frequency bandwidth of *s1* at this pump energy is 2.8 THz, which results in the *s1* chirp rate of 125 mrad/ps^2, close to the chirp rate of 124.5 mrad/ps^2 expected from the calculations based on the formula (Eq. (2.48)) by Strömqvist *et al.* [151].

80

At the pump energy of 131 µJ, the *s1* spectrum broadens on the low frequency side, reflecting increased pump depletion at the lower frequency side of the spectrum. At the same time, at this pump energy, the secondary MOPO process is already active and starts depleting *s1* on the high-frequency side of the spectrum. This interplay of the two processes is even more clearly visible at the pump energy of 203 µJ, where the *s1* FWHM spectral width is 2.55 THz, i.e. actually narrower that the one obtained at the pump energy of 76 µJ. Here, the energy from the *s1* high-frequency part of the spectrum with the corresponding phase modulation was transferred to the *s2* centered at 1897 nm. This depletion on the high-frequency side of the *s1* spectrum is clearly visible in the inset of the Fig. 5(c). The measured FWHM spectral bandwidth of the *s2* was 0.863 THz, which for the chirp transfer rate from *s1* to *s2*, $\partial \omega_{s2} / \partial \omega_{s1}$ of 1.005 [151], would give the *s2* FWHM pulse length of about 43 ps.
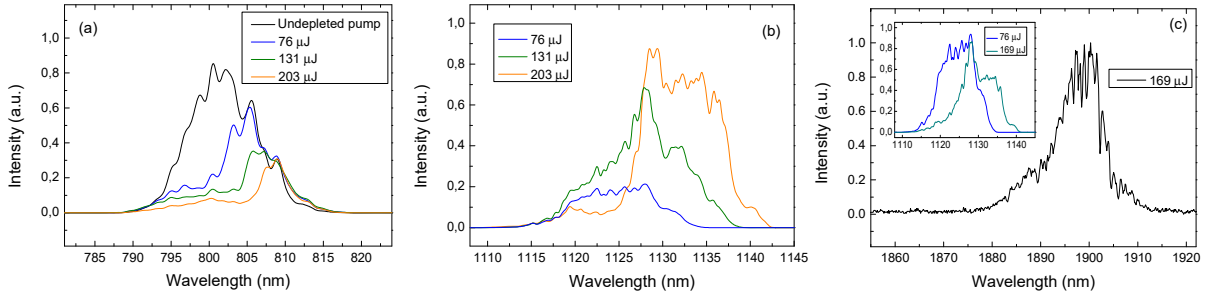

Fig. 7.17: Spectra of (a) the pump, (b) s1 and (c) s2 at different pump energies, shown in the figures legends [paper II]. Inset in (c) – Normalized s1 spectra at different pump energies, showing s1 depletion.

The spectra of the backward-propagating waves generated in the cascaded MOPO processes measured at the pump energy of 203 µJ are shown in Fig. 7.18. The spectral resolution of the measurement was 0.1 nm, which corresponds to the frequency resolution of about 4 GHz in the spectral range of the idlers. As expected, the wavelengths of the idlers generated in the two cascaded MOPO processes, *i1* and *i2*, change rather little as compared to the large steps in the central wavelengths of *s1* and *s2*. This can be attributed the counter-propagating wavelength being mainly dependent on the QPM period. The idler wave *i1* is centered at 2763.3 nm, and *i2* is centered at 2739.7 nm. The measured FWHM spectral-width of *i1* and *i2* were 17 GHz and 10 GHz, respectively. From the MOPO signal- and idler-chirp ratios the expected bandwidth can be estimated. In the first MOPO process (*s1*, *i1*) of the cascade the theoretical ratio is 84, while for the second process (*s2*, *i2*), the ratio is substantially larger and equal to 201. This indicates that the bandwidth of the *i2* is expected to be narrower than that of *i1*, as indeed is the case. From the spectral bandwidth of the corresponding signals, the expected *i1* and *i2* bandwidths were estimated to be 33 GHz and 4.3 GHz, respectively. It should be noted however, that the pulse-length of the *s2-i2* pair of the second cascade is of the order of 40 ps, which would give the transform-limited bandwidth of about 10 GHz, in accordance with the measured value. The spectrum around *i1* at the same time consists of two clearly resolved peaks. The higher amplitude peak is indeed idler *i1* from the primary MOPO process, while the other one with the FWHM of

28 GHz can be attributed to the third, cascaded MOPO pumped by the *s2*, i.e. the signal from the secondary, cascaded MOPO. The third cascade is indeed expected in a PPRKTP with a 755 nm period, with a wavelength of 5.9 µm for the forward-propagating idler, *i3*, and a wavelength of 2.762 µm for the backward-propagating signal, *s3*. We could not observe the forward-propagating wave owing to large absorption of the material at this wavelength. The wavelength of the *s3* is on the other hand within the bandwidth of *i1* so it can be expected that the third MOPO cascade is helped by cross-seeding from the idler of the first MOPO cascade. Another strong indication of the presence of the third cascade is the discrepancy of the measured pump depletion and the efficiency of the two first MOPO cascades at the pump energies above 140 µJ (see Fig. 7.17). It was verified that this discrepancy is not caused by the polariton scattering [28], once again attesting to the high quality of the QPM structure. Moreover, the idler spectrum below this pump energy does not contain the peak attributable to the third MOPO process.
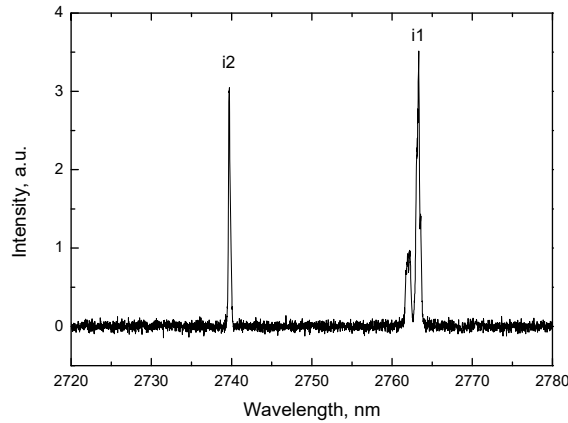

Fig. 7.18: Measured spectrum of the primary and secondary idlers. The smaller peak close to the primary idler (i1) corresponds to the signal of a cascaded, third MOPO process [paper II].

7.4.2 Highly efficient MOPO pumped by narrowband nanosecond pulses

The measured performance of the PPRKTP crystal in the ps-regime proves the very high quality and homogeneity of the fabricated QPM devices in this work. These sub-µm PPRKTP crystals can therefore be used in combination with well-established single-frequency nanosecond pump laser be used to generate millijoule-level narrowband pulses in the 1.5 µm - 3.4 µm spectral region. Such light source is of large interest for applications where spectral purity, energy and stability are of importance, e.g. remote sensing, spectroscopy, airborne and space-based LIDAR and quantum communications.

Therefore, the performance of a representative sub-µm PPRKTP crystal was evaluated as MOPO device in the nanosecond regime. The uncoated crystal was pumped by an injection-seeded, diode-pumped, single-longitudinal mode Q-switched Nd:YAG laser that provides 80 mJ, 10 ns-long linearly polarized pulses at 1064.4 nm at a repetition rate of 100 Hz. The pump energy was controlled by a half-waveplate and polarizer arrangement. The pump beam was polarized along the crystal *z*-axis and propagated parallel to the crystal *x*-axis. The crystal

temperature was kept at 22 °C by a thermoelectric element. In this configuration, the PPRKTP crystal generated a signal at 1740.1 nm that co-propagated with the pump, and a backward-propagating idler at 2741.4 nm. In order to characterize the performance of the MOPO, the signal and residual pump were separated by a dichroic mirror, (99 % transmission and reflection for the signal and pump, respectively), whereas the idler was separated from the pump path by a partially reflecting mirror that was placed before the focusing lens.

The MOPO threshold was reached at a pump energy of 0.76 mJ, corresponding to the threshold intensity of 660 MW/cm^2. The conversion efficiency and the pump depletion versus the pump energy are shown in Fig. 7.19 (a).
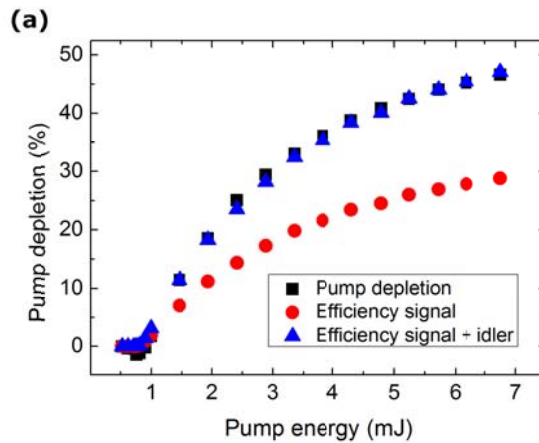

Fig. 7.19: MOPO conversion efficiency and pump depletion as a function of pump energy [paper III].

At a pump energy of 6.75 mJ, the signal energy reached 1.95 mJ, corresponding to the signal conversion efficiency of 29 %, while the combined signal-and-idler conversion efficiency was 47 %. The maximum pump energy was limited by the expected laser-induced damage threshold of RKTP crystals [101]. It should be noted that in MOPO the efficiency does not exhibit saturation or roll-off, which typically happens in OPOs with co-propagating interactions and is caused by back-conversion of the signal and idler to the pump. Owing to spatial separation of the signal and idler peak intensities in MOPO the back-conversion process is not efficient [53].

One of the striking features in MOPO is the narrow spectral width or high spectral brightness. Fig. 7.20 shows the spectra of (a) the pump, (b) the co-propagating signal, and (c) counter-propagating idler waves. The measured bandwidths of the signal and idler waves are 14.4 GHz and 16 GHz, respectively. Note that both parametric waves present narrow bandwidth. Indeed it is the counter-propagating nature of the interaction that gives MOPO its unique spectral features. In MOPO, the phase modulation of the pump is mainly transferred to the forward wave, meaning that the forward-wave is a spectral-shifted replica of the pump, while the phase of the backward wave remains essentially constant [151]. Thus, it is expected that the spectral width of the signal wave should be transformed limited for a single-longitudinal mode pump. On the other hand, the bandwidth of the idler would be automatically transform-limited, thanks to the counter-propagating geometry. The signal and idler pulse length of 6.7 ns at the pump power two-times

above the threshold were measured with fast photoelectromagnetic detector. The signal and idler spectra are in fact broader than the transform limit of the pulses. This broadening can be attributed to the slightly noncollinear pumping as a result of the non-ideal pump beam intensity profile [22].
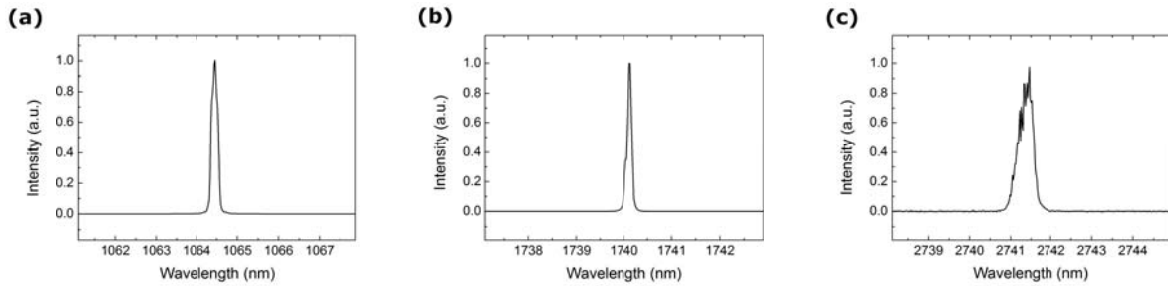

Fig. 7.20: Measured spectra of the pump (a), forward-propagating signal (b), and backward-propagating idler (c) waves [paper III].

The transverse intensity profiles of undepleted pump, signal and idler beams were characterized with a pyroelectric array camera. The beam profiles of the parametric waves were recorded at a pump energy two-times above the MOPO threshold, while the residual pump light was removed using a long pass filter with the cut-off wavelength at 1.5 µm. As shown in Fig. 7.21, the pump beam is astigmatic and contains two high-intensity regions as a result of thermal lensing properties in the Nd:YAG amplifier. At the focusing lens, with f = 200 mm, the separation between the areas is about 2.6 mm. In the PPRKTP crystal placed in the focus of the lens, the maximum noncollinear angle would be about 0.4 degrees, sufficiently large to increase the signal and idler spectral bandwidth to the values observed in the experiment [22]. This observation shows that in order to obtain the transform limited spectra in nanosecond MOPO the device must be pumped with a well-collimated TEM_{00} pump beam. Regardless of the intensity structure in the pump beam the signal and idler beams were homogeneous with some asymmetry which reflects that of the pump beam. It is indeed expected due to the MOPO property that the signal and idler self-establish strictly counter-propagating oscillation even for noncollinear pumping [22]. Moreover, the as discussed before, the suppression of the back-converting cascading process in MOPO should also prevent deterioration of the signal and idler beam quality.
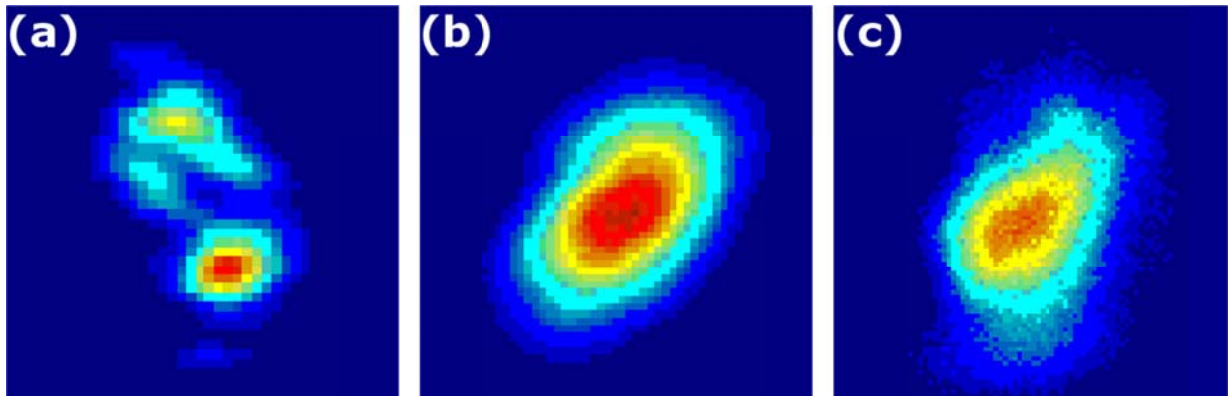
Fig. 7.21: Far-field intensity profiles of (a) undepleted pump, (b) signal, and (c) idler beams at a pump energy two times above the MOPO threshold [paper III].

It should be stressed that the MOPO operation with 10 ns pumping was possible only due to quality of the QPM structure throughout the full length of 7 mm. This gives sufficiently large margin for reaching the counter-propagating parametric oscillation threshold and safe operation below optical damage threshold. Increasing further the length of the QPM structure to 10 mm would decrease the MOPO threshold by two times. Moreover, the spectral width of the generated parametric waves is indeed orders of magnitude narrower than one would obtain from co-propagating interaction. In order to generate transform-limited nanosecond pulses, however, the MOPO should be pumped with well collimated fundamental transversal mode beams.

8 Summary

In this work, ferroelectric domain gratings with periods ranging from 755 nm to 9.22 μm were fabricated in RKTP crystals and, their performance has been assessed in a wide range of QPM applications. Samples fabricated with conventional electric-field poling have been used to investigate high-power blue SHG. Moreover, these PPRKTP crystals have also been used for demonstration of laser-written waveguides with excellent performance and with very little changes of the d_{eff} of the material.

The performance of the PPRKTP crystals at high powers was investigated in the blue spectral region. We obtained a record-high output power of 795 mW of continuous-wave blue light at 473 nm, and up to 2 W average power of pulsed light. However, the generated output powers were not stable over time. In agreement with what has been reported at in the green spectral region, the linear absorption of the visible light in RKTP results in thermal dephasing of the QPM device, significantly affecting the long-term operation. The thermal dephasing was the limiting factor for continuous wave operation as well as for the pulsed operation of the QPM device.

For the first time, laser-written waveguides were demonstrated in PPRKTP, using a double-track writing method. The waveguides had low losses of 1.6 dB for visible light and 2.2 dB for near-IR light. A normalized SHG conversion efficiency of $\eta = 4.6$ %W^{-1}cm^{-2} was demonstrated, by generating a record-high output of 76 mW of blue light. Although slight thermal dephasing was observed at 1.6 W of pump power, no catastrophic damage or deterioration of the fundamental and second harmonic modes could be observed. Moreover, the double-track, laser-written waveguides showed a superior mode overlap compared to conventional ion-exchanged waveguides.

The stability of the domain structures was investigated at elevated temperatures. This investigation was important from a fundamental point of view, but it also important from a device point of view since it could lead to an alternative way for fabricating QPM gratings by the direct-growth method. The observed movement of charged domain walls at high temperatures was anisotropic along the x- and y-directions. Along the y-axis domain wall motion is in the order of tens of micrometers. In the x-direction, it results in either three orders of magnitude smaller domain wall displacement or in domain merging, depending on the initial domain configuration. Moreover, gratings are increasingly unstable with a decreasing period, due to the increased domain-wall area to domain volume ratio.

Fabrication of dense ferroelectric domain gratings is challenging because of the required accurate control of the lateral domain-growth. Therefore, a novel patterning technique was developed in this work, based on coercive-field engineering inside the crystal bulk through an ion-exchange process. This novel patterning method allows for electric-field poling using planar electrodes, thereby alleviating the domain broadening associated with the ionic conductivity of RKTP and the metal electrodes normally used for periodic poling. The ion exchange process was

optimized to engineer coercive-field gratings to enhance the control of the lateral domain growth during the poling process.

The impact of the ion exchange on the optical properties of the PPRKTP was investigated by employing SHG in crystals with a period of $\Lambda = 3.16$ μm and with deep exchanged regions. While it is well known that the refractive index is increased in the ion exchanged regions, it was found that the ion exchange process itself induces a stress in the bulk of the crystal, resulting in a refractive index gradient along the polar axis in the bulk of the crystal, over the full crystal thickness. This gradient effectively alters the QPM condition along the *z*-axis of the PPRKTP, resulting in a possibility for tuning of the QPM wavelength.

This novel poling technique was further developed for fabrication of sub-μm domain gratings in RKTP. The domain gratings were of high quality and homogenous over the complete electrode area, and extended over the full crystal thickness. PFM studies of the non-polar y-surface confirmed that the domain broadening was limited to the depth of the coercive field grating and that the domains then propagated over the full 1 mm crystal thickness without further broadening. This proves the importance of the ion exchange process for fabrication of dense domain gratings in RKTP. In fact, this is the first time high-quality, sub-μm domain gratings have been demonstrated in RKTP.

The sub-μm PPRKTP crystals were used for the first MOPO demonstrations in RKTP. The MOPO was pumped using both picosecond and nanosecond long pump pulses. In the picosecond regime, the high-quality of the PPRKTP crystals enabled the demonstration of a record-low threshold and the first realization of a cascaded MOPO process, where the generated forward-propagating signal acted as a pump source for the cascaded MOPO. The cascaded process had a total conversion efficiency of 51 %.

Also, the first MOPO pumped using nanosecond-long pulses provided by a Q-switched laser operating in a single longitudinal mode was demonstrated. The MOPO generated 1.95 mJ of signal energy in the mid-IR spectral region, with a combined signal-and-idler conversion efficiency of 47 % homogenously over the crystal aperture. Both the forward propagating signal and the backward propagating idler were narrowband, with bandwidths of tens of GHz. The high conversion efficiency and favorable spectral properties make this device an attractive, single-pass source for generating near- and mid-infrared transform limited mJ-level pulses in a simple, compact and robust arrangement.

8.1 Outlook

The possibility of fabricating sub-μm QPM devices of high quality makes it possible to explore the full potential of nonlinear optics involving counter-propagating waves, which previously remained a largely unexplored field due to the lack of high-quality QPM devices. The novel poling technology developed in this work provides a method to fabricate QPM devices with increasingly shorter periods, with high reproducibility. As the period of the QPM device is further reduced, novel nonlinear processes could be experimentally demonstrated, such as a MOPO with counterpropagating signal ($\Lambda \sim 500$ nm), or counterpropagating optical amplifiers in which both the signal and the idler are counterpropagating with respect to the pump wave

($\Lambda \sim 250$ nm). Furthermore, there are a wide range of other applications where the MOPO processes can be exploited, for instance as ultrabright biphoton sources, frequency translators of photon quantum states and to provide narrowband seeding for subsequent parametric processes.

Moreover, the developed patterning technology based on ion exchange could potentially be used for fabrication of Volume Bragg Gratings (VBG) in KTP isomorphs. Fabrication of deep refractive index gratings, with sub-µm periods, could enable fabrication of VBGs reflective in the near- and mid-IR spectral regions. Such VBGs could for example be used for demonstration of monolithic OPOs were the cavity and the QPM grating are fabricated in the same crystal.

9 References

1. P. A. Franken, A. E. Hill, C. W. Peters, and G. Weinreich, "Generation of optical harmonics," Phys. Rev. Lett. **7**(4), 118–119 (1961).

2. C. J. Van Der Poel, J. D. Bierlein, J. B. Brown, and S. Colak, "Efficient type I blue second-harmonic generation in periodically segmented $KTiOPO_4$ waveguides," Appl. Phys. Lett. **57**(20), 2074–2076 (1990).

3. G. A. Magel, M. M. Fejer, and R. L. Byer, "Quasi-phase-matched second-harmonic generation of blue light in periodically poled $LiNbO_3$," Appl. Phys. Lett. **56**(2), 108–110 (1990).

4. A. Szilagyi, A. Hordvik, and H. Schlossberg, "A quasi-phase-matching technique for efficient optical mixing and frequency doubling," J. Appl. Phys. **47**(5), 2025–2032 (1976).

5. M. Yamada, N. Nada, M. Saitoh, and K. Watanabe, "First-order quasi-phase matched $LiNbO_3$ waveguide periodically poled by applying an external field for efficient blue second-harmonic generation," Appl. Phys. Lett. **62**(5), 435–436 (1993).

6. K. Kitamura, Y. Furukawa, K. Niwa, V. Gopalan, and T. E. Mitchell, "Crystal growth and low coercive field 180° domain switching characteristics of stoichiometric $LiTaO_3$," Appl. Phys. Lett. **73**(21), 3073–3075 (1998).

7. V. Gopalan, T. E. Mitchell, Y. Furukawa, and K. Kitamura, "The role of nonstoichiometry in 180° domain switching of $LiNbO_3$ crystals," Appl. Phys. Lett. **72**(16), 1981–1983 (1998).

8. Y. Furukawa, K. Kitamura, S. Takekawa, K. Niwa, and H. Hatano, "Stoichiometric $Mg:LiNbO_3$ as an effective material for nonlinear optics.," Opt. Lett. **23**(24), 1892–1894 (1998).

9. N. Yu Ei, S. Kurimura, Y. Nomura, and K. Kitamura, "Stable high-power green light generation with thermally conductive periodically poled stoichiometric lithium tantalate," Japanese J. Appl. Physics, Part 2 Lett. **43**(10 A), (2004).

10. D. A. Bryan, R. Gerson, and H. E. Tomaschke, "Increased optical damage resistance in lithium niobate," Appl. Phys. Lett. **44**(9), 847–849 (1984).

11. C. Canalias, *Domain Engineering in $KTiOPO_4$* (Doctoral thesis, Department of Applied Physics KTH, Stockholm Sweden, 2005).

12. G. Strömqvist, *Nonlinear Response in Engineered Optical Materials* (Doctoral thesis, Department of Applied Physics KTH, Stockholm Sweden, 2012).

13. C. Canalias and V. Pasiskevicius, "Mirrorless optical parametric oscillator," Nat. Photonics **1**, 459 (2007).

14. B. Boulanger, M. M. Fejer, R. Blachman, and P. F. Bordui, "Study of $KTiOPO_4$ gray-tracking at 1064, 532, and 355 nm," Appl. Phys. Lett. **65**(19), 2401–2403 (1994).

15. A. Zukauskas, *QPM Devices in KTA and RKTP* (Doctoral thesis, Department of Applied Physics KTH, Stockholm Sweden, 2014).

16. A. Zukauskas, N. Thilmann, V. Pasiskevicius, F. Laurell, and C. Canalias, "5 mm thick periodically poled Rb-doped KTP for high energy optical parametric frequency conversion," Opt. Mater. Express **1**(2), 201–206 (2011).

17. A. Zukauskas, V. Pasiskevicius, and C. Canalias, "Quasi-periodic self-assembled sub-micrometer ferroelectric bulk domain gratings in Rb-doped $KTiOPO_4$," Appl. Phys. Lett. **103**(25), (2013).

18. A. Zukauskas, G. Strömqvist, V. Pasiskevicius, F. Laurell, M. Fokine, and C. Canalias, "Fabrication of submicrometer quasi-phase- matched devices in KTP and RKTP [Invited]," Opt. Mater. Express **1**(7), 1319–1325 (2011).

19. G. Rosenman, K. Garb, A. Skliar, M. Oron, D. Eger, and M. Katz, "Domain broadening in quasi-phase-matched nonlinear optical devices," Appl. Phys. Lett. **73**(7), 865–867 (1998).

20. S. E. Harris, "Proposed backward wave oscillation in the infrared," Appl. Phys. Lett. **9**(3), 114–116 (1966).

21. C. Canalias, V. Pasiskevicius, M. Fokine, and F. Laurell, "Backward quasi-phase-matched second-harmonic generation in submicrometer periodically poled flux-grown KTiOPO$_4$," Appl. Phys. Lett. **86**(18), 181105 (2005).

22. G. Strömqvist, V. Pasiskevicius, and C. Canalias, "Self-established noncollinear oscillation and angular tuning in a quasi-phase-matched mirrorless optical parametric oscillator," Appl. Phys. Lett. **98**(5), (2011).

23. G. Strömqvist, V. Pasiskevicius, C. Canalias, P. Aschieri, A. Picozzi, and C. Montes, "Temporal coherence in mirrorless optical parametric oscillators," J. Opt. Soc. Am. B **29**(6), 1194 (2012).

24. V. Pasiskevicius, C. Canalias, G. Strömqvist, and F. Laurell, "Mirrorless OPO: first steps towards unlocking the potential of counter-propagating three-wave interactions," Proc. SPIE **6875**, (2008).

25. J. B. Khurgin, "Slowing and stopping photons using backward frequency conversion in quasi-phase-matched waveguides," Phys. Rev. A **72**(2), 1–5 (2005).

26. C. S. Chuu and S. E. Harris, "Ultrabright backward-wave biphoton source," Phys. Rev. A - At. Mol. Opt. Phys. **83**(6), 1–4 (2011).

27. H. J. McGuinness, M. G. Raymer, and C. J. McKinstrie, "Theory of quantum frequency translation of light in optical fiber: application to interference of two photons of different color.," Opt. Express **19**(19), 17876–907 (2011).

28. H. Jang, A.-L. Viotti, G. Strömqvist, A. Zukauskas, C. Canalias, C. A. C. Analias, and V. Pasiskevicius, "Counter-propagating parametric interaction with phonon-polaritons in periodically poled KTiOPO$_4$," Opt. Express **25**(3), 17092–17098 (2017).

29. D. A. Kleinmann, "Nonlinear dielectric polarization in optical media," Phys. Rev. **126**(1977), (1962).

30. E. Hecht, *Optics*, 4th ed (Addison Wesley Publishing, 2001).

31. R. Boyd, *Nonlinear Optics*, 3rd ed (Academic Press, 2008).

32. J. A. Armstrong, N. Bloembergen, J. Ducuing, and P. S. Pershan, "Interactions between light waves in a nonlinear dielectric," Phys. Rev. **127**(1918), (1962).

33. G. D. Boyd and C. K. N. Patel, "Enhancement of optical second-harmomic generation (SHG) by reflection phase matching in ZnS and GaAs," Appl. Phys. Lett. **8**(313), (1966).

34. P. D. Maker, R. W. Terhune, M. Nisenhoff, and C. M. Savage, "Effects of Dispersion and Focusing on the Production of Optical Harmonics," Phys. Rev. Lett. **8**(21), (1962).

35. J. A. Giordmaine, "Mixing of Light Beams in Crystals," Phys. Rev. Lett. **8**(19), (1962).

36. L. A. Eyres, P. J. Tourreau, T. J. Pinguet, C. B. Ebert, J. S. Harris, M. M. Fejer, L. Becouarn, B. Gerard, and E. Lallier, "All-epitaxial fabrication of thick, orientation-patterned GaAs films for nonlinear optical frequency conversion," Appl. Phys. Lett. **79**(7), 904–906 (2001).

37. A. Chowdhury, H. M. Ng, M. Bhardwaj, and N. G. Weimann, "Second-harmonic generation in periodically poled GaN Second-harmonic generation in periodically poled GaN," **1077**(2003), 1–4 (2006).

38. A. Peña, B. Ménaert, B. Boulanger, F. Laurell, C. Canalias, V. Pasiskevicius, L. Ortega, P. Segonds, J. Debray, C. Félix, and A. Pen, "Bulk PPKTP by crystal growth from high temperature solution," J. Cryst. Growth **360**(1), 52–55 (2012).

39. M. Fejer, G. A. Magel, D. H. Jundt, and R. L. Byer, "Quasi-Phase-Matched Second Harmonic Generation: Tuning and Tolerances," IEEE J. Quantum Electron. **28**(11), 2631–2654 (1992).

40. G. D. Boyd, "Parametric Interaction of Focused Gaussian Light Beams," J. Appl. Phys. **39**(8), 3597 (1968).

41. Y. N. Korkishko and V. a. Fedorov, *Ion Exchange in Single Crystals for Integrated Optics and Optoelectronics* (Cambridge International Science Pub., 1999).

42. R. V. Ramaswamy and R. Srivastava, "Ion-Exchanged Glass Waveguides: A Review," J. Light. Technol. **6**(6), 984–1000 (1988).

43. F. Laurell, T. Calmano, S. Müller, P. Zeil, C. Canalias, and G. Huber, "Laser-written waveguides in KTP for broadband Type II second harmonic generation," Opt. Express **20**(20), 22308 (2012).

44. G. Agrawal, *Applications of Nonlinear Fiber Optics*, Optics and Photonics (Elsevier Science, 2001).

45. W. P. Risk, T. R. Gosnell, and A. V. Nurmikko, *Compact Blue–Green Lasers* (Cambridge University Press, 2003).

46. J. M. Manley and H. E. Rowe, "Some General Properties of Nonlinear Elements Part I. General Energy Relations," in *Proceedings of the IRE 44* (1956).

47. S. J. Brosnan and R. L. Byer, "Optical Parametric Oscillator Threshold and Linewidth Studies," IEEE J. Quantum Electron. **15**(415), (1979).

48. A. E. Siegman, "Nonlinear Optical Effects: An Optical Power Limiter," Appl. Opt. **1**(6), 739 (1962).

49. P. P. Bey and C. L. Tang, "Plane-Wave Theory of Parametric Oscillator and Coupled Oscillator-Upconverter," IEEE J. Quantum Electron. **8**(3), 361–369 (1972).

50. E. Granot, S. Pearl, and M. M. Tilleman, "Analytical solution for a lossy singly resonant optical parametric oscillator," J. Opt. Soc. Am. B **17**(3), 381–386 (2000).

51. H. Kogelnik and C. V. Shank, "Stimulated emission in a periodic structure," Appl. Phys. Lett. **18**(4), 152–154 (1971).

52. H. Kogelnik and C. V. Shank, "Coupled-wave theory of distributed feedback lasers," J. Appl. Phys. **43**(5), 2327–2335 (1972).

53. Y. J. Ding and J. B. Khurgin, "Backward Optical Parametric Oscillators and Amplifiers," IEEE J. Quantum Electron. **32**(9), 1574–1582 (1996).

54. C. Hammond, *The Basics of Crystallography and Diffraction*, 3rd ed. (Oxford University Press, 2009).

55. Engineers Electronics, "IEEE Standard Definitions of Primary Ferroelectric Terms," East **986**, (1986).

56. M. E. Lines and A. M. Glass, *Principles and Applications of Ferroelectrics and Related Materials* (Oxford University Press, 1977).

57. V. K. Yanovskii and V. I. Voronkova, "Ferroelectric Phase Transitions and Properties of Crystals of the KTiOPO4 Family," Phys Status Solidi A **93**(2), 665–668 (1986).

58. T.Volk and M.Wöhlecke, *Lithium Niobate* (Springer Series in Materials Science, 2008).

59. W. J. Merz, "Domain formation and domain wall motions in ferroelectric BaTiO$_3$ single crystals," Phys. Rev. **95**(3), 690–698 (1954).

60. R. Landauer, "Electrostatic considerations in BaTiO$_3$ domain formation during polarization reversal," J. Appl. Phys. **28**(2), 227–234 (1957).

61. V. Janovec, "Anti-parallel ferroelectric domains in surface space-charge layers of BaTiO$_3$," Czechoslov. J. Phys. **9**(4), 468–480 (1959).

62. M. Molotskii, R. Kris, and G. Rosenman, "Fluctuon effects in ferroelectric polarization switching," J. Appl. Phys. **88**(2000), 5318–5327 (2000).

63. G. Gerra, A. K. Tagantsev, and N. Setter, "Surface-stimulated nucleation of reverse domains in ferroelectrics," Phys. Rev. Lett. **94**(10), 1–4 (2005).

64. A. K. Tagantsev, L. E. Cross, and J. Fousek, *Domains in Ferroic Crystals and Thin Films* (Springer, 2010).

65. C. Canalias, J. Hirohashi, V. Pasiskevicius, and F. Laurell, "Polarization-switching characteristics of flux-grown KTiOPO$_4$ and RbTiOPO$_4$ at room temperature," J. Appl. Phys. **97**(12), 124105 (2005).

66. R. C. Miller and G. Weinreich, "Mechanism for the sidewise motion of 180° domain walls in barium titanate," Phys. Rev. **117**(6), 1460–1466 (1960).

67. R. C. Miller and A. Savage, "Velocity of Sidewise 180˚ domain-wall motion in BaTiO$_3$ as a function of the applied electric field," Phys. Rev. **112**(3), 755–762 (1958).

68. H. L. Stadler, "Ferroelectric switching time of BaTiO$_3$ crystals at high voltages," J. Appl. Phys. **29**(10), 1485–1487 (1958).

69. G. Rosenman, A. Skliar, M. Oron, and M. Katz, "Polarization reversal in KTiOPO4 crystals," J. Phys. D. Appl. Phys. **30**, 277–282 (1997).

70. P. Urenski, M. Lesnykh, Y. Rosenwaks, G. Rosenman, and M. Molotskii, "Anisotropic domain structure of KTiOPO$_4$ crystals," J. Appl. Phys. **90**(4), 1950–1954 (2001).

71. L. Ouvrard and M. Troost, "Rechearches sur les phosphates doubles de titane, d'etain et de cuivre," Compt Rend. **111**, 177–179 (1890).

72. F. C. Zumsteg, J. D. Bierlein, and T. E. Gier, "K$_x$Rb$_{1-x}$TiOPO$_4$: A new nonlinear optical material," J. Appl. Phys. **47**(11), 4980–4985 (1976).

73. H. Vanherzeele and J. D. Bierlein, "Potassium titanyl phosphate: properties and new applications," J. Opt. Soc. Am. B **6**(4), 622–633 (1989).

74. P. Tordjman, R. Masse, and J. Guitel, "Structure Cristalline du Monophosphate KTiPO$_5$," Zeitschrift für Krist. **139**, 103–115 (1974).

75. H. Karlsson and F. Laurell, "Electric field poling of flux grown KTiOPO$_4$," Appl. Phys. Lett. **71**(24), 3474–3476 (1997).

76. M. C. Gupta, W. P. Risk, A. C. G. Nutt, and S. D. Lau, "Domain inversion in KTiOPO$_4$ using electron beam scanning," Appl. Phys. Lett. **63**(9), 1167–1169 (1993).

77. G. Rosenman, A. Skliar, D. Eger, M. Oron, and M. Katz, "Low temperature periodic electrical poling of flux-grown KTiOPO$_4$ and isomorphic crystals," Appl. Phys. Lett. **73**(25), 3650–3652 (1998).

78. W. P. Risk and S. D. Lau, "Periodic electric field poling of KTiOPO$_4$ using chemical patterning," Appl. Phys. Lett. **69**(26), 3999–4001 (1996).

79. D. R. Allan, J. S. Loveday, R. J. Nelmes, and P. A. Thomas, "A high-pressure structural study of potassium titanyl phosphate (KTP) up to 5 GPa," J. Phys. Condens. Matter **4**(11), 2747–2760 (1992).

80. P. A. Thomas, A. M. Glazer, and B. E. Watts, "Crystal structure and nonlinear optical properties of KSnOPO$_4$ and their comparison with KTiOPO$_4$," Acta Crystallogr. Sect. B **46**(5), 692–692 (1990).

81. D. D. Xue and S. S. Zhang, "The origin of nonlinearity in KTiOPO4," Appl. Phys. Lett. **70**(8), 943–945 (1997).

82. P. A. Thomas, P. Cloetens, T. Lyford, and J. Baruchel, "Structural matching of ferroelectric domains and associated distortion in potassium titanyl phosphate crystals," **15**, 1613–1624 (2003).

83. R. A. Stolzenberger and M. P. Scripsick, "Recent advancements in the periodic poling and characterization of RTA and its isomorphs," Optoelectron. '99 - Integr. Optoelectron. Devices **3610**(January), 23–35 (1999).

84. R. A. Laudise, R. J. Cava, and A. J. Caporaso, "Phase relations, solubility and growth of potassium titanyl phosphate, KTP," J. Cryst. Growth **74**(2), 275–280 (1986).

85. R. J. Bolt, M. H. van der Mooren, and H. de Haas, "Growth of KTiOPO$_4$ (KTP) single crystals by means of phosphate and phosphate/sulfate fluxes out of a three-zone furnace," J. Cryst. Growth **114**(1-2), 141–152 (1991).

86. K. Hutton, R. Ward, and K. Godfrey, in *Materials Research Society Symposium Proceedings 329* (1994), p. 23.

87. P. A. Thomas, R. Duhlev, and S. J. Teat, "A comparative structural study of a flux-grown crystal of K$_{0.86}$Rb$_{0.14}$TiOPO$_4$ and an ion-exchanged crystal of K$_{0.84}$Rb$_{0.16}$TiOPO$_4$," Acta Crystallogr. Sect. B Struct. Sci. **50**(5), 538–543 (1994).

88. A. Zukauskas, V. Pasiskevicius, and C. Canalias, "Second-harmonic generation in periodically poled bulk Rb-doped KTiOPO$_4$ below 400 nm at high peak-intensities.," Opt. Express **21**(2), 1395–1403 (2013).

89. S. Tjörnhammar, V. Maestroni, A. Zukauskas, T. K. Uždavinys, C. Canalias, F. Laurell, and V. Pasiskevicius, "Infrared absorption in KTP isomorphs induced with blue picosecond pulses," Opt. Mater. Express **5**(12), 2951 (2015).

90. G. K. Samanta, S. C. Kumar, M. Mathew, C. Canalias, V. Pasiskevicius, F. Laurell, and M. Ebrahim-Zadeh, "High-power, continuous-wave, second-harmonic generation at 532 nm in periodically poled KTiOPO$_4$," Opt. Lett. **33**(24), 2955–2957 (2008).

91. Q. Jiang, P. A. Thomas, K. B. Hutton, and R. C. C. Ward, "Rb-doped potassium titanyl phosphate for periodic ferroelectric domain inversion," J. Appl. Phys. **92**(5), 2717–2723 (2002).

92. S. Wang, V. Pasiskevicius, and F. Laurell, "High-efficiency frequency converters with periodically-poled Rb-doped KTiOPO$_4$," Opt. Mater. (Amst). **30**(4), 594–599 (2007).

93. P. A. Morris, A. Ferretti, J. D. Bierlein, and G. M. Loiacono, "Reduction of the ionic conductivity of flux grown KTiOPO$_4$ crystals," J. Cryst. Growth **109**(1-4), 361–366 (1991).

94. D. K. T. Chu, J. D. Bierlein, and R. G. Hunsperger, "Piezoelectric and Acoustic Properties of Potassium Titanyl Phosphate (KTP) and its Isomorphs," IEEE Trans. Ultrason. Ferroelectr. Freq. Control **39**(6), 683–687 (1992).

95. G. Hansson, H. Karlsson, S. Wang, and F. Laurell, "Transmission Measurements in KTP and Isomorphic Compounds.," Appl. Opt. **39**(27), 5058–5069 (2000).

96. M. V Pack, D. J. Armstrong, and A. V Smith, "Measurement of the χ $^{(2)}$ tensors of KTiOPO$_4$, KTiOAsO$_4$, RbTiOPO$_4$, and RbTiOAsO$_4$ crystals," **43**(16), 3319–3323 (2004).

97. T. Y. Fan, C. E. Huang, B. Q. Hu, R. C. Eckardt, Y. X. Fan, R. L. Byer, and R. S. Feigelson, "Second harmonic generation and accurate index of refraction measurements in flux-grown $KTiOPO_4$," Appl. Opt. **26**(12), 2390–2394 (1987).

98. K. Fradkin, A. Arie, A. Skliar, and G. Rosenman, "Tunable midinfrared source by difference frequency generation in bulk periodically poled $KTiOPO_4$," Appl. Phys. Lett. **74**(7), 914–916 (1999).

99. W. Wiechmann, S. Kubota, T. Fukui, and H. Masuda, "Refractive-index temperature derivatives of potassium titanyl phosphate.," Opt. Lett. **18**(15), 1208–1210 (1993).

100. S. Emanueli and A. Arie, "Temperature-dependent dispersion equations for $KTiOPO_4$ and $KTiOAsO_4$," Appl. Opt. **42**(33), 6661–6665 (2003).

101. R. S. Coetzee, N. Thilmann, A. Zukauskas, C. Canalias, and V. Pasiskevicius, "Investigations of laser induced damage in $KTiOPO_4$ and $Rb:KTiOPO_4$ at 1 μm and 2 μm," Opt. Mater. Express **5**(9), 2090–2095 (2015).

102. C. L. Zhang, Z. G. Hu, L. X. Huang, W. N. Zhou, Z. Lue, G. Zhang, Y. C. Liu, Y. B. Zou, F. H. Lu, H. D. Hou, S. J. Qin, H. X. Zhang, and L. Bai, "Growth and optical properties of bulk KTP crystals by hydrothermal method," J. Cryst. Growth **310**(7-9), 2010–2014 (2008).

103. F. Ahmed, "Laser damage threshold of $KTiOPO_4$," Appl. Opt. **28**(1), 119–122 (1989).

104. A. Hildenbrand, F. R. Wagner, H. Akhouayri, J.-Y. Natoli, M. Commandré, F. Théodore, and H. Albrecht, "Laser-induced damage investigation at 1064 nm in $KTiOPO_4$ crystals and its analogy with $RbTiOPO_4$," Appl. Opt. **48**(21), 4263–4269 (2009).

105. D. S. Hum, R. K. Route, G. D. Miller, V. Kondilenko, A. Alexandrovski, J. Huang, K. Urbanek, R. L. Byer, and M. M. Fejer, "Optical properties and ferroelectric engineering of vapor-transport-equilibrated, near-stoichiometric lithium tantalate for frequency conversion," J. Appl. Phys. **101**(9), 093108 (2007).

106. P. Zeil, A. Zukauskas, S. Tjörnhammar, C. Canalias, V. Pasiskevicius, and F. Laurell, "High-power continuous-wave frequency-doubling in $KTiOAsO_4$," Opt. Express **21**(25), 30453 (2013).

107. G. J. Edwards, M. P. Scripsick, L. E. Halliburton, and R. F. Belt, "Identification of a radiation-induced hole center in $KTiOPO_4$," Phys. Rev. B **48**(10), 6884–6891 (1993).

108. R. Eachus, V. Laguta, M. Glinchuk, A. Watterich, and A. Hofstaetter, "Electron paramagnetic resonance and electron – nuclear double-resonance study of Ti^{3+} centres in $KTiOPO_4$," J. Phys. Condens. Matter **15**, 3969–3984 (2003).

109. S. Wang, V. Pasiskevicius, and F. Laurell, "Dynamics of green light-induced infrared absorption in $KTiOPO_4$ and periodically poled $KTiOPO_4$," J. Appl. Phys. **96**(4), 2023–2028 (2004).

110. J. Hirohashi, V. Pasiskevicius, S. Wang, and F. Laurell, "Picosecond blue-light-induced infrared absorption in single-domain and periodically poled ferroelectrics," J. Appl. Phys. **101**(3), (2007).

111. N. F. Mott and R. W. Gurney, *Electronic Processes in Ionic Crystals* (Oxford University Press, 1940).

112. H. H. Wieder, "Activation Field and Coercivity of Ferroelectric Barium Titanate," J. Appl. Phys. **28**(3), 367–369 (1957).

113. J. D. Bierlein, A. Ferretti, L. H. Brixner, and W. Y. Hsu, "Fabrication and characterization of optical waveguides in $KTiOPO_4$," Appl. Phys. Lett. **50**(18), 1216–1218 (1987).

114. C. Kittel and H. Kroemer, *Thermal Physics* (W. H. Freeman, 1980).

115. H. M. Garfinkel, "Ion-exchange equilibriums between glass and molten salts," J. Phys. Chem. **72**(12), 4175–4181 (1968).

116. W. P. Risk, "Fabrication and characterization of planar ion-exchanged $KTiOPO_4$ waveguides for frequency doubling," Appl. Phys. Lett. **58**(1), 19 (1991).

117. D. K. T. Chu, "Acoustic and optical properties of thallium ion-exchanged KTiOPO4," Appl. Phys. Lett. **65**, 1989–1991 (1994).

118. J. Cugat, R. Solé, J. J. Carvajal, X. Mateos, J. Massons, G. Lifante, F. Díaz, and M. Aguiló, "Channel waveguides on $RbTiOPO_4$ by Cs+ ion exchange.," Opt. Lett. **38**(3), 323–5 (2013).

119. M. G. Roelofs, P. A. Morris, and J. D. Bierlein, "Ion exchange of Rb, Ba, and Sr in $KTiOPO_4$," J. Appl. Phys. **70**(2), 720–728 (1991).

120. P. A. Thomas, S. C. Mayo, and B. E. Watts, "Crystal structures of $RbTiOAsO_4$, $KTiO(P_{0.58},As_{0.42})O_4$, $RbTiOPO_4$ and $(Rb_{0.465},K_{0.535})TiOPO_4$, and analysis of pseudosymmetry in crystals of the $KTiOPO_4$ family," Acta Crystallogr. Sect. B Struct. Sci. **48**(4), 401–407 (1992).

121. F. Laurell, "Periodically poled materials for miniature light sources," Opt. Mater. (Amst). **11**(January), 235–244 (1999).

122. J. M. White and P. F. Heidrich, "Optical waveguide refractive index profiles determined from measurement of mode indices: a simple analysis," **15**(1), 151–155 (1976).

123. P. A. Thomas and M. A. Glazer, "Potassium Titanyl Phostphate, $KTiOPO_4$. II. Structural interpretation," J. Appl. Cryst. **24**, 968–971 (1991).

124. J. Gehler, W. Karthe, C. Wächter, A. Bräuer, A. Rasch, and M. Rottschalk, "ARROW's in $KTiOPO_4$," IEEE Photonics Technol. Lett. **9**(4), 470–472 (1997).

125. H. Karlsson, F. Laurell, and L. K. Cheng, "Periodic poling of $RbTiOPO_4$ for quasi-phase matched blue light generation," Appl. Phys. Lett. **74**(11), 1519–1521 (1999).

126. G. Lindgren, A. Zukauskas, V. Pasiskevicius, F. Laurell, and C. Canalias, "Studies of sub-millisecond domain dynamics in periodically poled Rb-doped $KTiOPO_4$, using online in situ second harmonic generation," Opt. Express **23**(16), 20332 (2015).

127. C. Canalias, V. Pasiskevicius, F. Laurell, S. Grilli, P. Ferraro, and P. De Natale, "In situ visualization of domain kinetics in flux grown $KTiOPO_4$ by digital holography," J. Appl. Phys. **102**(6), (2007).

128. F. Laurell, M. G. Roelofs, W. Bindloss, H. Hsiung, A. Suna, and J. D. Bierlein, "Detection of ferroelectric domain reversal in $KTiOPO_4$ waveguides," J. Appl. Phys. **71**(10), 4664–4670 (1992).

129. F. Masiello, T. A. Lafford, P. Pernot, J. Baruchel, D. S. Keeble, P. A. Thomas, A. Zukauskas, G. Strömqvist, F. Laurell, and C. Canalias, "Investigation by coherent X-ray section topography of ferroelectric domain behaviour as a function of temperature in periodically poled Rb:KTP," J. Appl. Crystallogr. **44**(3), 462–466 (2011).

130. V. D. Kugel, G. Rosenman, N. Angert, E. Yaschin, and M. Roth, "Domain inversion in $KTiOPO_4$ crystal near the Curie point," J. Appl. Phys. **76**(8), 4823–4826 (1994).

131. J. D. Bierlein and F. Ahmed, "Observation and poling of ferroelectric domains in $KTiOPO_4$," Appl. Phys. Lett. **51**(17), 1322–1324 (1987).

132. C. Canalias, S. Wang, V. Pasiskevicius, and F. Laurell, "Nucleation and growth of periodic domains during electric field poling in flux-grown $KTiOPO_4$ observed by atomic force microscopy," Appl. Phys. Lett. **88**(3), 032905 (2006).

133. X. Liu, K. Kitamura, K. Terabe, and S. Takekawa, "Stabilization of periodically poled domain structures in a quasiphase-matching device using near-stoichiometric LiTaO$_3$," J. Appl. Phys. **102**(1), (2007).

134. X. Liu, K. Kitamura, and K. Terabe, "Thermal stability of LiTaO$_3$ domains engineered by scanning force microscopy," Appl. Phys. Lett. **89**(14), 1–4 (2006).

135. X. Liu, K. Kitamura, Y. M. Liu, F. S. Ohuchi, and J. Y. Li, "Thermal-induced domain wall motion of tip-inverted micro/nanodomains in near-stoichiometric LiNbO3 crystals," J. Appl. Phys. **110**(5), (2011).

136. V. Y. Shur, "Kinetics of ferroelectric domains: Application of general approach to LiNbO$_3$ and LiTaO$_3$," Front. Ferroelectr. A Spec. Issue J. Mater. Sci. **1**, 199–210 (2007).

137. Y. Kan, H. Bo, X. Lu, T. Xu, Y. Jin, X. Wu, F. Huang, and J. Zhu, "Decay properties of artificial two-domain structures in LiNbO$_3$ crystals studied by scanning probe microscope," Appl. Phys. Lett. **97**(20), 202903 (2010).

138. Z. M. Liao, S. A. Payne, J. Dawson, A. Drobshoff, C. Ebbers, D. Pennington, and L. Taylor, "Thermally induced dephasing in periodically poled KTP frequency-doubling crystals," J. Opt. Soc. Am. B **21**(12), 2191–2196 (2004).

139. B. Boulanger, I. Rousseau, J. P. Fève, M. Maglione, B. Ménaert, and G. Marnier, "Optical Studies of Laser-Induced Gray-Tracking in KTP," IEEE J. Quantum Electron. **35**(3), 281–286 (1999).

140. P. Zeil, *Tailored Fiber Lasers and Their Use in Nonlinear Optics* (Doctoral thesis, Department of Applied Physics KTH, Stockholm Sweden, 2015).

141. L. Deyra, I. Martial, J. Didierjean, F. Balembois, and P. Georges, "3 W, 300 µJ, 25 ns pulsed 473 nm blue laser based on actively Q-switched Nd:YAG single-crystal fiber oscillator at 946 nm.," Opt. Lett. **38**(16), 3013–6 (2013).

142. S. A. Payne, J. Dawson, A. Drobshoff, D. Pennington, Z. M. Liao, L. Taylor, and C. Ebbers, "Thermally induced dephasing in periodically poled KTP frequency-doubling crystals," J. Opt. Soc. Am. B **21**(12), 2191 (2004).

143. S. Greenstein and M. Rosenbluh, "Dynamics of cw intra-cavity second harmonic generation by PPKTP," Opt. Commun. **238**(4-6), 319–327 (2004).

144. F. Laurell and G. Arvidsson, "Frequency doubling in Ti:MgO:LiNbO$_3$ channel waveguides," J. Opt. Soc. Am. B **5**(2), 292–299 (1988).

145. V. A. Maslov, V. A. Mikhailov, O. P. Shaunin, and I. A. Shcherbakov, "Nonlinear absorption in KTP crystals," Quantum Electron. **27**(4), 356–359 (1997).

146. B. C. Stuart, M. D. Feit, S. Herman, A. M. Rubenchik, B. W. Shore, and M. D. Perry, "Nanosecond-to-femtosecond laser-induced breakdown in dielectrics," Phys. Rev. B **53**(4), 1749–1761 (1996).

147. N. Yu, C. Jung, D. Ko, and J. Lee, "Thermal dephasing of quasi-phase-matched second-harmonic generation in periodically poled stoichiometric LiTaO3 at high input power," J. Korean Phys. Soc. **49**(2), 528–532 (2006).

148. P. B. Phua, K. S. Lai, R. F. Wu, and T. C. Chong, "Coupled tandem optical parametric oscillator (OPO): an OPO within an OPO," Opt. Lett. **23**(16), 1262 (1998).

149. P. V Gorelik, F. N. C. Wong, D. Kolker, and J.-J. Zondy, "Cascaded optical parametric oscillation with a dual-grating periodically poled lithium niobate crystal.," Opt. Lett. **31**(13), 2039–41 (2006).

150. H. Vanherzeele and J. D. Bierlein, "Magnitude of the nonlinear-optical coefficients of KTiOPO$_4$," Opt. Lett. **17**(14), 982–984 (1992).

151. G. Strömqvist, V. Pasiskevicius, C. Canalias, and C. Montes, "Coherent phase-modulation transfer in counterpropagating parametric down-conversion," Phys. Rev. A - At. Mol. Opt. Phys. **84**(2), 1–4 (2011).